technische universität
dortmund

MR:comp

Dissertation zur Erlangung des akademischen Grades
Doctor rerum naturalium

MR Safety of Implantable Medical Devices

Optimization and uncertainty reduction of the measurement procedure for the safety assessment of RF-induced heating during an MRI examination for patients with implantable medical devices

Finya Ketelsen
geboren in Flensburg

2025

Experimentelle Physik IV
Fakultät Physik
Technische Universität Dortmund
in Zusammenarbeit mit
MR:comp GmbH
Gelsenkirchen

Erstgutachter:	Prof. Dr. K. Kröninger
Zweitgutachter:	Jun.-Prof. Dr. A. Lühr
Abgabedatum:	26. März 2025
Mündliche Prüfung:	28. Mai 2025

Abstract

RF-induced heating is one of the safety hazards for patients with implants in MRI. Implants are classified as passive or active, with different test procedures measuring the resulting temperature rise. Heating depends on the E-field along the implant and the implant characteristics such as size and material. Implants are tested using a phantom container filled with a tissue simulating medium placed in an RF exposure system. Typically, a body coil from an MR scanner is used. Since these coils are designed to produce a homogeneous B-field, they are not ideal for E-field generation. Their disadvantages in terms of E-field homogeneity and direction are investigated in this thesis. An alternative exposure system (LES) is extensively validated and compared to a body coil system. Different sized passive objects are used, resulting in a higher temperature rise in the LES compared to the body coil for the same average E-field. Therefore, the possible temperature rise per E-field in the body coil is underestimated, while the E-field distribution in the LES leads to a worst-case temperature rise, increasing the reliability of the patient risk.
For active implants, a novel measurement approach with fixed object to E-field probe distance is validated and compared to the standard approach. The overall uncertainty is reduced by half by eliminating the uncertainty of probe position and coupling. In addition, the measurement time is reduced from several days to hours, measuring thousands of data points instead of about 25.

Kurzfassung

HF-induzierte Erwärmung ist eines der Sicherheitsrisiken für Patienten mit Implantaten im MRT. Implantate werden als passiv oder aktiv eingestuft, wobei verschiedene Testverfahren den resultierenden Temperaturanstieg messen. Die Erwärmung hängt vom E-Feld entlang des Implantats und von den Implantateigenschaften wie Größe und Material ab. Die Implantate werden mit einem Phantombehälter getestet, der mit einem gewebesimulierenden Medium gefüllt ist und in einem HF-Expositionssystem platziert wird. In der Regel wird eine Körperspule aus einem MR-Scanner verwendet. Da diese Spulen für die Erzeugung eines homogenen B-Feldes ausgelegt sind, eignen sie sich nicht für die Erzeugung eines E-Feldes. Ihre Nachteile in Bezug auf die Homogenität und Richtung des E-Feldes werden in dieser Arbeit untersucht. Ein alternatives Expositionssystem (LES) wird ausgiebig validiert und mit einem Körperspulensystem verglichen. Es werden unterschiedlich große passive Objekte verwendet, was bei gleichem durchschnittlichen E-Feld zu einem höheren Temperaturanstieg im LES im Vergleich zur Körperspule führt. Daher wird der mögliche Temperaturanstieg pro E-Feld in der Körperspule unterschätzt, während die E-Feldverteilung in der LES zu einem Worst-Case-Temperaturanstieg führt, was die Zuverlässigkeit des Patientenrisikos erhöht.
Für aktive Implantate wird ein neuartiger Messansatz mit festem Abstand zwischen Objekt und E-Feldsonde validiert und mit dem Standardansatz verglichen. Die Gesamtunsicherheit wird um die Hälfte reduziert, indem die Unsicherheit der Sondenposition und der Kopplung eliminiert wird. Darüber hinaus wird die Messzeit von mehreren Tagen auf Stunden reduziert, wobei Tausende von Datenpunkten statt etwa 25 gemessen werden.

Contents

Nomenclature

Abbreviations

AIMD	Active implantable medical device
ASTM F2182	ASTM F2182-19$^{\epsilon 2}$
BC	Body coil
FG	Function generator
ISO/TS	ISO/TS 10974:2018
LES	Linear Exposure System
MRI	Magnetic resonance imaging
RF	radio-frequncy
rms	root mean square
SAR	Specific absorption rate
SNR	Signal-to-noise-ratio
TDS	Time domain sensor
TF	Transfer function
TO	Test object
TSM	Tissue simulating medium

Companies

ING Gao	Ingeneubüro Gao, Mülheim, Germany
MR:comp	MR:comp GmbH, Gelsenkirchen, Germany
SPEAG	Schmid & Parter Engineering AG, Zurich, Switzerland
TOMCO	TOMCO Technologies, Stepney, Australia
WEIDMANN	WEIDMANN Technologies Deutschland GmbH, Dresden, Germany
ZMT	ZMT Zurich MedTech AG, Zurich, Switzerland

List of Figures

List of Tables

1 Introduction

Advances in modern medicine have led to a steady increase in life expectancy in recent years. As people age, the likelihood of disease increases, and imaging techniques such as magnetic resonance imaging become more important. In addition, the number of people with implants is increasing, and so is the number of people with implants who need MRI scans [1, 2].
Currently, many patients with implants are excluded from MRI scans due to safety concerns. Various test methods are available to assess these safety risks that may be associated with certain implants. Depending on the classification of the implants as passive or active, there are standard procedures for these tests, namely ASTM F2182-19$^{\epsilon 2}$ (ASTM F2182) [3] and ISO/TS 10974 (ISO/TS) [4], respectively. For passive implants without any electrical support, four safety hazards can occur, and for active implants with electrical support, there are more diverse and complex safety hazards due to the interaction between the electrical parts of the implant and the MRI.
From a testing perspective, the MRI is divided into its three magnetic field sources, the static magnetic field, the time-varying gradient field, and the time-varying radio-frequency (RF) field. Each source is responsible for specific interactions. The implants to be tested are placed in a phantom filled with a medium representing the electrical properties of an average human body and exposed to the specific fields [3, 4]. In addition to imaging artifacts, motion due to magnetic force or torque for passive implants, and unintended stimulation, vibration or malfunction, RF-induced heating is one of the safety hazards that must be addressed before an implant can be labeled MR safe or MR conditional instead of MR unsafe [5].
RF-induced heating occurs because the electric field generated by the time-varying RF field induces eddy currents in a conductive material that are converted to tissue heating at hot spots. The physical theory of MRI and the physical laws leading to RF-induced heating are described in detail in the chapter 2 including the test procedures according to Ref. [3] and Ref. [4].
To evaluate the magnitude of the temperature rise ΔT due to RF-induced heating, a test system that generates the fields of interest, in this case an RF exposure system, is required. ASTM F2182 and ISO/TS standards define several requirements for these RF exposure systems regarding E-field distribution and homogeneity.
The most commonly used RF exposure systems are the body coil (BC) within the MR scanner or stand-alone body coils. The goal of these coils is to produce a homogeneous magnetic field to ensure the desired imaging quality. From an imaging point of view, the E-field produced is an unavoidable by-product. Therefore, the E-field distribution produced by these coils is not ideal for testing RF-induced heating in terms of homogeneity and direction.
For the passive implants, an homogeneous E-field is necessary to scale the measured ΔT to the mean E-field at the test location of a certain test object. The result is then scaled to the E-field experienced in a patient during an MRI scan.
For active implants, high stability and repeatability of the E-field is required to de-

termine RF-induced heating as accurately as possible [4].
This work was done in cooperation with the MR:comp GmbH (MR:comp), a test laboratory for MR safety and compatibility. As an RF exposure system, a stand-alone BC including different probes is available. In chapter 3 the available equipment is characterized and especially the potential for optimization is investigated. A BC is not the optimal RF exposure system in terms of E-field distribution and homogeneity. From the analysis of the advantages and disadvantages of a BC used for the test method to determine the RF-induced heating, optimizations are developed and an open linear dipole-based RF exposure system (LES) was designed by "Ingenieurbüro Gao" (ING Gao) as an optimized system focusing on the generation of the electric field instead of the magnetic field. This system consists of two dipole antennas, allowing the system to generate different E-field distributions within the phantom. The general behavior and in particular the E-field distribution inside the phantom are measured and compared with the E-field predicted by numerical simulations. The validation in terms of sufficient agreement of the numerical predictions and the measured E-field distribution and the validation of the measured ΔT of a standard object are described in chapter 4.
In chapter 5 two comparative studies for the test procedure of passive implants are carried out. First, elongated test objects are measured in both systems and their ΔT is compared. The influence of the E-field homogeneity on ΔT is determined. In a second study, a similar comparison is made for different 3D extended objects, investigating the extent of E-field homogeneity and distribution along the test object. The general advantages of the LES design over the BC are described and an optimized measurement approach is proposed to increase the stability and repeatability of the measurements.
For the test procedure to determine the power deposition due to RF-induced heating of active implants, a modified measurement approach is possible with the LES. During the test procedure, an electromagnetic model of the test object is determined and needs to be validated. The model is capable of converting the tangential E-field along the test object into a power deposition or ΔT at the hot spot. After validating this model for various tangential E-field distributions, it is capable of predicting the ΔT for a tangential E-field occurring inside a patient during an MRI examination. Inside a BC, the validation measurement procedure is very time consuming and prone to measurement uncertainties. With the LES and the novel approach, it is possible to reduce the measurement time from several days to a few hours, while increasing the number of measurement points from about 25 to several thousand. This approach is validated and compared with a standard object and the extent of optimization is evaluated in chapter 6 including a proposed general approach for different objects.
The overall conclusion and evaluation of the LES compared to the BC and further possibilities for measurement optimization are describes in chapter 7.

During this work the following contributions to conferences and publications were made.

1. F. Ketelsen, J. Kreutner, G. Schaefers, "Validity of radial symmetric hot spot distribution around a lead for comparison of different probe types at various orientations to a lead", ISMRM Workshop on MR Safety 2019 [6]

2. F. Ketelsen, S. Scholz, W. Görtz, J. Kreutner, G. Schaefers, K. Kröninger, "The influence of probes positioning for measuring RF-induced 3D-power de-

position on a lead with E-field and temperature probes", ESMRMB 2019 Annual scientific meeting, 2019 [7]

3. F. Ketelsen, J. Kreutner, G. Schaefers, K. Kröninger, "Approach to reduce the measurement volume to determine spatial distribution of power deposition around a straight lead according to ISO/TS 10974", ISMRM & SMRT Virtual Conference & Exhibition, 2020 [8]

4. F. Ketelsen, G. Schaefers, K. Kröninger, "Validation of a new 64 MHz RF exposure system for testing medical implants for RF-induced heating according to ASTM-F2182 and ISO/TS 10974", ISMRM & SMRT Annual Meeting & Exhibition, 2021 [9]

5. F. Ketelsen, H. Hammersen, G. Schaefers, K. Kröninger, "Influence of E-Field Homogeneity and Temporal E-Field Drift for Testing Medical Implants for RF-induced heating at 64MHz according to ASTM-F2182 and ISO/TS 10974", ISMRM & SMRT Annual Meeting & Exhibition, 2021 [10]

6. H. Hammersen, F. Ketelsen, A. Rennings, G. Schaefers, "Numerical Simulation study on the effects of intentionally inhomogeneous E-field distributions on RF-induced heating of implants", ISMRM & SMRT Annual Meeting & Exhibition, 2021 [11]

7. F. Ketelsen, H. Gao, G. Schaefers, "Validation of a novel 128 MHz dual channel dipole-based RF exposure system to test medical implants for RF-induced heating according to ASTM-F2182 and ISO/TS 10974", ISMRM Workshop on MR Safety, 2022 [12]

8. F. Ketelsen, G. Schaefers, "New System, New Approach: Fasten up transfer function validation measurements, prove of concept", ISMRM & ISMRT Annual Meeting & Exhibition, 2023 [13]

9. F. Ketelsen, Y. Zhang, G. Schaefers, "Evaluation of a Dipole-based RF Exposure System for Testing RF-induced Heating of Passive Implants at 64 MHz", prepared and will be submitted in April 2025[14]

2 The physics of MR safety

2.1 Fundamentals and components of the MRI

Magnetic resonance imaging (MRI) is a medical imaging technique that uses magnetic fields and radio waves to produce images of the internal structures of the human body, particularly soft tissues such as the brain, organs or muscles. Compared to other imaging techniques such as computer tomography, the MR scanner does not use ionizing radiation and is therefore considered to be largely safe [15].
The basic idea of MRI is to use hydrogen nuclei (protons) as the imaging quantity, since the human body is 67 % water and the water molecules contain hydrogen atoms. The MRI consists of a strong static magnetic field, typically produced by superconducting magnets that require liquid helium to maintain their superconducting state. The magnetic field strength ranges from 0.5 to 3 Tesla in clinical use, and up to 7 or 9.4 T in research. The magnetic field, generated by the superconducting magnets is called B_0 and produces a magnetization aligned with the z-axis (head-to-feet) of the MRI. Without a magnetic field, the proton spins are randomly oriented, but when exposed to a magnetic field, there is an energetically favorable orientation aligned and parallel to the magnetic field. The Boltzmann distribution describes the ratio of protons in parallel and antiparallel states, and for the field strength of 1.5 T the ratio is about 6.6 ppm. Only the protons in the parallel state are used for imaging [16].
To produce a signal, a second time-varying magnetic field is applied as radio-frequency (RF) pulses. The proton spins rotate at a Larmor-frequency, which depends on the strength of the B_0-field. The RF pulses have the same frequency and when they are applied, the protons are knocked out of alignment and the magnetization is moved towards the xy-plane (x-axis: left-right, y-axis: anterior-posterior). After the RF pulse is turned off, the protons and magnetization return to their original state, aligned with the static field. This process is known as relaxation. During relaxation, the protons rotate in the xy-plane, inducing a voltage in the receiver coil that can be measured as a signal. The relaxation time depends on the tissue type and therefore visualizes the contrast between structures in the image [17].
Coils are typically used to apply the RF pulse and detect the relaxation proton signal. Depending on the body volume to be examined, different sizes and shapes are available. There are coils that can transmit and receive the pulse and signal, or alternatively, two coils are used, one for applying the pulse and one for receiving the signal. In clinical MR scanners, a built-in BC is available as a transmit and receive coil. The signal is processed by a computer that converts the raw data into an image using Fourier transformation [17].
The third component of an MR scanner are the gradient coils, which produce a second time-varying magnetic field used for spatial encoding. There are three gradient coils in the system, one for each spatial direction. The gradient coils add a magnetic field to the static field that slightly changes the resonance frequency for each position. Therefore, it is possible to select a particular slice with one gradient

coil and encode the signal within that slice with the other two gradient coils. There are many different ways to use and switch the gradient coils, offering almost unlimited possibilities to choose slices and directions to measure exactly the body part of interest [16].
Not only the ability to choose any slice and direction makes MRI a powerful and flexible imaging technique, but also the variety of sequences that can be applied. A sequence describes the order in which the RF pulse and gradient coils are turned on and off, the number of RF pulses applied, the flip angle of each pulse, and the time between pulses. These parameters affect imaging contrast for different tissues. Standard sequences are available for specific body regions and disease screening, as well as advanced techniques. For brain imaging, functional MRI (fMRI) is used to image diffusion or brain activity. Furthermore, contrast agents can be used or even other molecules can be used as imaging source instead of hydrogen [18, 19, 20, 21, 22, 23].
Even though MRI is a powerful and widely used imaging tool, some safety issues need to be considered. All metallic and magnetic objects are prohibited in the MR room, as they could be accelerated into the bore and potentially harm the patient [24]. A second problem could be unintentional nerve stimulation. To avoid these effects, several precautions are taken. The patient must change out of street clothes and remove any jewelry, such as earrings. The patient is placed on the MR table so that the inner legs are not in contact and the arms are placed without forming loops. These precautions can reduce nerve stimulation and contact burns. In addition, depending on the patient's weight and height, a limit is calculated for the maximum energy to be applied [25].
However, if a patient has any type of metallic implant, the number of potential safety hazards increases and can lead to severe tissue or implant damage, depending on the type of implant. In addition to potential imaging artifacts, the implant may move, vibrate, or deform. The implant could be unintentionally stimulated or malfunction during and after the MR examination, or parts of the implant could heat up. These safety risks could lead to the exclusion of patients with certain implants [3, 4, 25].
This thesis focuses on the potential heating of the implant, particularly RF-induced heating, which is described in detail in the following section.

2.2 RF-induced heating

The potential risk of RF-induced heating has been known since the early development of MR imaging [26]. As described above, the RF pulses are a time-varying magnetic field with the goal of applying a homogeneous magnetic B-field across the coil volume. According to Faraday's law, each time-varying magnetic field $B(t)$ is accompanied by an electric field $E(t)$. These electric fields induce eddy currents in the conductive material. The current density J depends on the conductivity σ of the material in which the currents are induced and the so-called incident E-field

$$J = \sigma E. \tag{2.2.1}$$

Eddy currents also occur in biological tissue, but since the conductivity of metallic implants is about 10^6 times higher than in the biological tissue, the current density is much larger. The induced eddy currents cause two effects. Power dissipation inside the implant occurs due to ohmic losses. This leads to a temperature rise ΔT depending on the heat capacity c of the mass Δm. As a second effect, the induced

currents induce a secondary electromagnetic field around the implant, which is superimposed on the incident E-field. Thus, the power deposition around the implant is modified. Both effects can lead to tissue heating [27].
A key parameter is the Specific Absorption Rate (SAR), which describes the absorbed RF power P_{RF} per exposed mass

$$SAR = \frac{P_{RF}}{\Delta m} = \frac{\sigma \mid E \mid^2}{2\rho}, \tag{2.2.2}$$

where ρ is the density of the mass and σ its conductivity. P_{RF} is the sum of the power of the applied RF pulses. Assuming continuous RF exposure and no heat dissipation, the local temperature increases linearly with the SAR. The SAR is different for each MR sequence and is limited to a safe exposure level depending on the size and weight of the patient [27].
The so-called skin effect describes that the currents inside the metallic implant are limited to the thin surface layer by the laws of electromagnetics. Therefore, the mass of the implant is too small to effectively heat the surrounding tissue. However, the induced scattered fields can multiply the incident E-field at critical locations, called hot spots. In particular, for elongated implants with a length of half the RF wavelength, the energy deposition is maximal at their distal ends. In this case, the energy of the incident E-field is most effectively converted into eddy currents and scattering field due to the so-called antenna effect [27].
The RF-induced heating of an implant therefore depends on the incident E-field to which the object is exposed. In particular, the amplitude and phase of the tangential component of the incident E-field are responsible for the magnitude of the resulting ΔT. Depending on the size of the patient, its position within the MR scanner, and the dimensions and orientation of the implant within the patient, the incident E-field at the implant location changes and thus the ΔT at the possible hot spots [28].
Over the past decades, extensive research has been conducted on the MR safety of various types of implants, especially in the area of RF-induced heating [29, 30, 31, 32, 33, 34, 35, 36, 37, 38, 39, 40, 41]. The classification of implants into passive and active implants and the definition of an electrical length and corresponding implant size at which RF-induced heating is negligible have led to the development of international standards. They describe a standardized approach for testing the different implants in an *in vitro* environment to estimate the patient risk during an MR examination [3, 4].
These standards are continually evaluated and updated to reflect the latest research findings. The measurement approaches for passive and active implants are described individually in the following sections, including their requirements for the measurement system and setup.

2.3 Standard test method for passive implantable medical devices

A common procedure for testing passive implantable devices for RF-induced heating is provided by the American Society for Testing and Materials (ASTM). In April 2020, the current version ASTM F2182-19$^{\epsilon 2}$ was published as an international standard, updating the 2011 version [42]. The title is "Standard Test Method for Measurement of Radio Frequency Induced Heating on or Near Passive Implants During

Magnetic Resonance Imaging" and was developed by a committee that includes all interested parties such as implant manufacturers, MR scanner manufacturers and developers, testing laboratories, scientists and physicians. The scope of this method is to test passive implants *in vitro* in a phantom container and does not provide acceptance criteria for heating levels. Implants are classified as passive if they perform all of their functions without any electrical power supply, whereas they are classified as active if their design includes any type of electrical power supply. Typical passive implants are joints, screws, plates, stents, or dental implants [43].
The method is only valid for the safety issue of RF-induced heating for fully implanted devices for the frequency corresponding to 1.5 T and 3 T MR systems. The size of the recommended ASTM phantom container is 420x150x650 mm with a rectangular shape, filled to a height of 90 mm with human equivalent medium [3].
The general approach of the test method is to place the test object (TO) completely inside a tissue simulating medium (TSM) with the average properties of a human body in terms of electrical conductivity, mass density and thermal properties. Temperature probes are placed at the locations where the maximum temperature rise ΔT is expected and at a reference location at least 30 cm away from the TO. The phantom is placed in an RF exposure system that provides sufficient magnitude at the test location to measure ΔT with sufficient signal-to-noise ratio (SNR). The measurement is performed with and without the TO in place, without moving the temperature probes, under the same measurement conditions [3].
There are specific requirements for the TSM, RF exposure system, probes, and measurement room to ensure a reliable and repeatable measurement. The requirements are listed in the table 2.1.

Parameter	Specification
Electrical conductivity	$0.47\,\mathrm{V/m} \pm 10\,\%$
Relative permittivity ϵ_r	80 ± 20
Local background heating	10 times the probe precision
Implant position	≥ 20 mm distance to every surface
Incident E-field homogeneity	± 1 dB
Probe placement precision	1 mm
Probe precision	$\leq 0.1\,^{\circ}\mathrm{C}$
Probe accuracy	$\pm 0.5\,^{\circ}\mathrm{C}$
Temperature recording before and after measurement	± 2 min
Temporal resolution	≤ 2 s
Room temperature	$20\,^{\circ}\mathrm{C}$-$25\,^{\circ}\mathrm{C}$
Stability of the room temperature	$\pm 2.0\,^{\circ}\mathrm{C/h}$

Table 2.1: List of measurement requirements according to ASTM F2182 for the TSM, the exposure system, the measurement probes and the measurement room [3].

If any of the requirements in table 2.1 cannot be met for a particular implant, additional analysis and measurements may be required to estimate the extent of the influence on the ΔT results. As an optional step, the ASTM F2182 recommends that a reference TO be included in the measurement. This reference object is a 100 mm titanium-alloy rod with a 1 mm hole at each end. This object is called SAIMD-2

and the specifications are described in Ref. [4]. For this object, the expected ΔT per incident E-field is known and can be used to monitor the run-to-run repeatability. The final result of the test method is the maximum ΔT scaled to the local incident E-field for the measurement time used. The typical measurement time is six or 15 minutes of continuous RF exposure. It is the responsibility of the implant manufacturer to provide a relationship between the measured ΔT in the phantom and the possible ΔT in a patient population [3].

2.4 Standard test method for active implantable medical devices

The test procedure for active implantable medical devices (AIMDs) is provided by the International Organization for Standardization (ISO). The current version is the ISO/TS 10974:2018 [4], available as a second edition since April 2018. Currently, the document is a Technical Specification (TS), but the first edition of the ISO will be available in the near future. The title of this document is "Assessment of the safety of magnetic resonance imaging for patients with an active implantable medical device" and describes test methods not only for the safety issue of RF-induced heating, but for all safety issues that may arise during an MRI examination involving active implants [4]. Pacemakers, nerve simulators or cochlear implants are typical active implants [43].

MR source	Hazard	Clause number /TS
RF field RF	Electrode heating	8
	Device heating	8
	Unintended stimulation	15
	Malfunction	15
Gradient field G	Device heating	9
	Vibration	10
	Unintended stimulation	13
	Malfunction	16
Static field B_0	Vibration	10
	Force	11
	Torque	12
	Malfunction	14
Combined fields	Malfunction	17

Table 2.2: Safety hazards and the responsible MR fields, the static B_0, the gradient field G and the RF field RF, including the clause number describing the hazards in the ISO/TS, extracted from Ref. [4].

The current ISO/TS only applies to the implanted parts of a device for the frequency corresponding to a 1.5 T MR scanner. The updated version, which may be published in 2026, will also cover 3 T. The final determination of risk or the establishment of a safety criterion is not within the scope of the ISO/TS, but is the responsibility of the manufacturer or the regulatory authorities [4].
The ISO/TS is divided into ten clauses, each of which describes a known or potential

safety issue. The relationship between the magnetic field component of the MR scanner and the safety issues that arise is listed in the table 2.2. Only Clause 8, which describes RF-induced electrode heating for active implants, is used for this work, and therefore only Clause 8 and its appendices are described in this section. The objective of Clause 8 is to determine the power deposition around one or more hot spots of an AIMD. ISO/TS recommends a tiered approach, describing four Tiers of increasing complexity and accuracy. General requirements for all Tiers are listed in the table 2.3.

Parameter	Specification
RF frequency	$64\,\mathrm{MHz} \pm 5\,\%$
Incident E-field variation	$< \pm 1\,\mathrm{dB}$ in magnitude
(entire AIMD pathway)	$< \pm 20\,^\circ$ in phase
Incident E-field drift	$< 0.25\,\mathrm{dB}$
TSM electrical conductivity	$0.47\,\mathrm{V/m} \pm 10\,\%$
TSM relative electrical permittivity ϵ_r	$78 \pm 10\,\%$

Table 2.3: List of requirements according to the ISO/TS for the RF exposure system, extracted from Ref. [4].

There are more suitable medium conductivities provided in the ISO/TS, but only the conductivity of $\sigma = 0.47\,\mathrm{S/m}$ is used in this work. A measurement system to be used for testing implants according to the standard must be validated as described in Annex I of the ISO/TS [4].
Several steps are required before a suitable Tier can be selected. The hot spot or hot spots must be identified. A hot spot is defined as a location that is within 6 dB or 25 % of the highest ΔT over the entire AIMD length. For identified hot spots, the 3D spatial power distribution is either predicted numerically and validated with a series of measurements, or measured by fully mapping the hot spot volume with the temperature or SAR or E-field probe. Once the distribution is determined, the magnitude is measured under the appropriate conditions to scale the distribution to the final value. This method varies for the different Tiers [4].
Depending on the characteristics of the AIMDs, the most appropriate Tier is selected. The four Tiers and their main differences are as follows

1. No modelling, global E_{max}
2. Human modelling, E_{max} in implantation volume
3. Human modelling, E_{tan} along implant length, AIMD modelling
4. Simultaneous human and AIMD modelling

The most conservative approach is Tier 1, which is only suitable for short AIMDs. Tier 4 requires simultaneous modelling, which results in the least overestimation, but also requires extensive computing power. Therefore, neither Tier 1 nor Tier 4 is feasible for most AIMDs. The Tier 2 approach is similar to the test method for passive implants, where the ΔT per local incident E-field is determined. This value is scaled to the maximum E-field expected in the implant volume in a human. In order to minimize the overestimation due to the use of the maximum E-field, this level is also mostly suitable for shorter AIMDs [4].
To date, the most suitable and practical Tier for the wide range of AIMDs is Tier

3, which uses the tangential E-field along the AIMD and separate modelling of the AIMD and the human population. The part of this work related to active implantable devices uses the Tier 3 approach, which will be described in more detail. The Tier 3 approach consists of several steps. First, an electromagnetic model of the AIMD, called a transfer function (TF), is developed. Numerical, analytical or experimental methods can be used to determine the TF. The AIMD is exposed piece-wise to a constant incident E-field along the entire length of the object and the resulting magnitude and phase at the hot spot are measured [44, 45, 46]. Thus, the specific response of the AIMD to a homogeneous tangential E-field is modelled. The power deposition at the hot spot can be calculated from the model and the tangential incident E-field to which the implant is exposed to, according to the following equation

$$P = A\left|\int_l TF_{\text{hot spot}}(z)\, E_{\tan}(z)\, dz\right|^2. \tag{2.4.1}$$

In this equation, P describes the power deposition at the hot spot, A is a constant, l is the length of the AIMD, z is the position along the AIMD, $TF_{\text{hot spot}}$ is the developed transfer function and $E_{\tan}$ is the tangential incident E-field along the AIMD. The tangential E-field can be obtained numerically from human models [4].
To ensure that the developed TF provides valid results not only for a homogeneous E-field, but for any kind of tangential E-field distribution in magnitude and phase along the AIMD, it needs to be validated. To do this, the AIMD is placed in a phantom container filled with the specific medium. The AIMD is exposed to a known set of different and unique tangential incident E-fields and the ΔT for each exposure condition is measured at the hot spot. To change the exposure condition and thus the tangential E-field along the TO, the AIMD path is changed for each measurement. An example set of exposure conditions is given in Annex M of ISO/TS [4], suggesting different phantom containers and trajectories. The exposure conditions should include amplitude ramps, linear phase, and linear phase combined with linear amplitude along the length of the implant, as may occur in a patient during an MRI examination. In addition, the condition should include a distribution where the phase along the implant is reversed to ensure that the TF is valid for all types of tangential E-field distributions. The resulting ΔT per exposure condition is compared to the predicted ΔT using the developed TF with equation 2.4.1. To determine a validation criterion, the uncertainties of the measurement and the TF are analyzed and compared to the total error between the measurement and the TF predictions [4].
When the TF is validated and its prediction uncertainty is known, it can be used to calculate power deposition for clinically relevant exposure conditions obtained from human modelling [4].

3 The measurement equipment and behavior

3.1 Probe types, measurement and movement systems

The equipment used to perform the measurement studies presented in this thesis consists of the RF exposure system and its power supply. To measure RF-induced heating of any test object (TO), the measurement setup within the exposure system consists of a phantom filled with a tissue simulating medium (TSM), the measurement probes, and optionally a movement system, where the measurement probes can be fixed and moved through the exposure system. The following sections introduce and describe all components used for a typical measurement.

3.1.1 RF exposure system and power supply

The RF exposure system available in the MR:comp test laboratory is the BC of the Medical Implant Test System (MITS) developed by ZMT (Zurich MedTech AG). Further information about the complete MITS can be found in Ref. [47]. For the measurement series in this work, only the BC of the MITS is used with a customized power supply. A schematic overview of the system is shown in Fig. 3.1. The BC is horizontally oriented and matched and tuned to 64 MHz, equivalent to 1.5 T. The length of the BC is 650 mm and the length of the surrounding shield is 850 mm. The inside diameter of the BC is 700 mm. It consists of 16 copper rungs, where the end rings have capacitors between the rungs, which can be individually adjusted to the desired resonance frequency. Therefore, it is a high pass coil with two connectors at 90° to each other. More detailed information about a typical high pass BC can be found in Ref. [48].
In contrast to an MRI examination using RF pulses and circular excitation, the test methods used in this work use a continuous wave (cw) sinusoidal RF signal and linear polarization. The different polarization does not change the E-field distribution in the isoplane of the xz-plane in terms of homogeneity, but the magnitude of the field is higher for the linear polarization resulting in a better SNR, as displayed in Annex M of Ref. [4]. The typical measurement time for medical device testing is 15 minutes with cw excitation, which corresponds to an average MR examination time with many short RF pulses.
The BC is placed on a table in an RF cabin with sufficient distance to each wall. The system is powered by RF cables connected to a filter plate that runs outside the cabin. A two-channel function generator (FG) supplies power to two amplifiers. Couplers are connected after the amplifiers to monitor the transmitted and reflected power after each amplifier with an oscilloscope. From the couplers, the RF cables are connected to the outside of the filter plate. The circuit is schematically presented in Fig. 3.1.
A two channel function generator (FG) is used and the unit of the amplitude is

set to dBm. The frequency is set according to the S-parameter measurement made before each measurement with the BC.

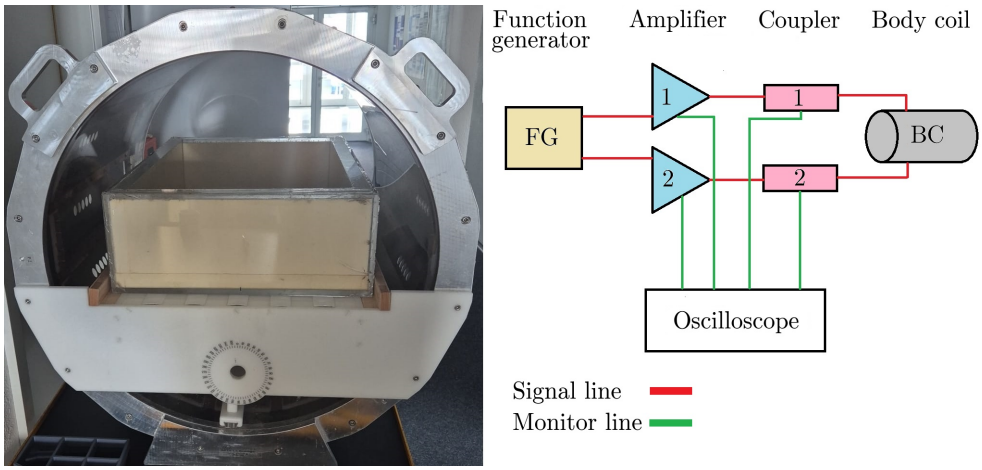

Figure 3.1: The body coil forms the bore loaded with the ASTM phantom so that the isocenter of the coil aligns with the isocenter of the TSM filled phantom on the left and a schematic overview of the supply line including the signal line with the two channels from the function generator (FG) to the body coil (BC) and monitoring line to the oscilloscope, logging the transmitted and reflected power.

The S-parameters describe the frequency at which the reflection is smallest and the amount of coupling between the channels. Since the rung material is sensitive to room temperature and is additionally heated by the current flow when the system is turned on, its expansion changes slightly with the temperature of the material. This material expansion changes the distance between the rungs and therefore the capacitance of the capacitors connecting them. It is therefore necessary to match the frequency to the actual coil condition to avoid high reflections. The S-parameters of the BC are exemplary presented in Fig. 3.2.
The S-parameters show a slight difference between the channels. The resonance frequency is within the requirements of 64 MHz$\pm$5 %, as listed in table 2.3. The S_{11} and S_{22} are at -15.37 dB at 62.91 MHz and -17.37 dB at 62.95 MHz, respectively, with narrowband resonance. S_{21} and S_{12} are by definition equal at -20.77 at 63.04 MHz describing the coupling between the two channels. The smaller the S-parameters, the more signal is transmitted rather than reflected. During a measurement, the temperature of the material increases, causing the resonant frequency to increase slightly. For example, the frequency was increased from 63.00 MHz to 63.08 MHz during ten consecutive temperature measurements, with each run lasting six minutes. Details of this measurement can be found in section 5.2.
Two 500 W amplifiers from TOMCO Technologies (TOMCO) are used, producing 57 dBm of gain. An oscilloscope is used to monitor the behavior of the BC, recording the transmitted and reflected power for both channels picked up by the couplers every 0.5 seconds. The typical load and measurement probes and setups are described in the following section 3.1.2.
On each measurement day, the S-parameters are determined and the current resonance frequency is set at the FG. After the system is set up and turned on, it takes about 30 minutes to reach a steady state and a nearly stable E-field value and

distribution inside the phantom. This is due to the warm-up time of the amplifiers and coil components. The measurement time varies considerably depending on the measurement task. For a typical temperature measurement, the coil is turned on twice for 15 minutes without any warm-up time. For an E-field mapping measurement, the coil warms up for 30 minutes before starting the mapping, which can take another 30 to 60 minutes, depending on the desired mapping resolution. As described earlier, the frequency changes slightly as the coil material warms up. The longer the system is on, the warmer the coil material becomes as a result of the currents flowing through the material. Therefore, the resonance frequency increases slightly during the measurement time. In addition, the E-field slowly continues to decrease over the measurement time. Thus, the longer the measurement time, the more the E-field distribution changes. An additional factor in this change is the changing conductivity of the TSM depending on its temperature.
Because of this, it is important to monitor the system closely with the oscilloscope. However, even with monitoring, it is difficult to ensure the same measurement conditions on different measurement days and for different times the system is turned on.

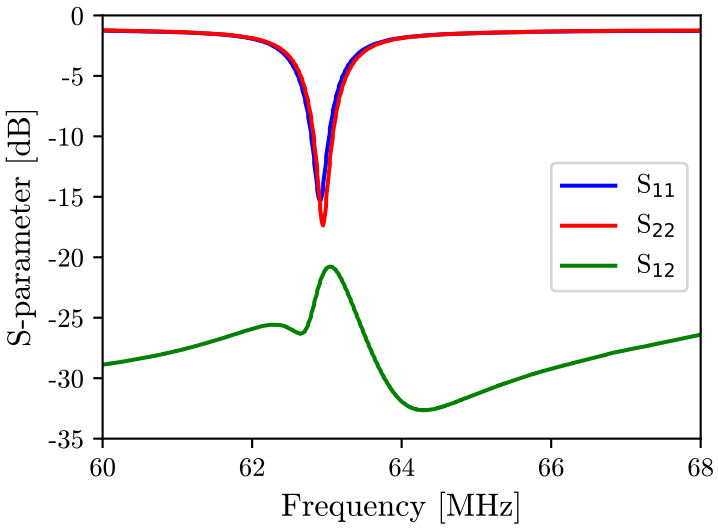

Figure 3.2: S-parameter for the body coil for the frequency range between 60 and 68 MHz to determine the resonance frequency and system conditions.

3.1.2 Components of the measurement setup

In principle, phantoms can have different sizes and shapes. However, in all measurements related to this work, the ASTM phantom is used because it is the largest phantom available, displayed in Fig. 3.1. The phantom is usually filled with TSM. In this work, two different TSMs are used. A saline solution is used for E-field measurements, while a gelled solution is used for temperature measurements due to its higher heat capacity. Both TSMs have the same conductivity and permittivity and are prepared according to the requirements and formulation described in Ref. [3].
The energy generated by the E-field of the BC is absorbed by the medium in the phantom. It is defined as the Specific Absorption Rate (SAR), which is described

by

$$SAR = \lim c\frac{\Delta T}{\Delta t} = \frac{\sigma \mid E \mid^2}{2\rho} = \frac{\sigma E_{\text{rms}}^2}{\rho}, \tag{3.1.1}$$

where $c = 4150\,\text{J/(kg°C)}$ is the specific heat, ΔT is the temperature rise and Δt the measurement time. The peak E-field is $\mid E \mid$ and E_{rms} is the root mean square (rms) of the E-field, σ is the electrical conductivity in S/m and ρ the mass density in kg/m^3.
Annex M of Ref. [4] shows the expected E-field distribution inside the ASTM phantom for linear and circular polarization. To measure the extent of RF-induced heating, it is necessary to achieve stable and known measurement conditions that must be re-evaluated from time to time to ensure reliability. Therefore, the E-field inside the phantom must be measured with a suitable probe. MR:comp offers several E-field probes. The Time Domain Sensor (TDS) system from Schmid & Partner Engineering AG (SPEAG) includes E-field probes and H-field probes that measure the field in a specific direction [49]. In this work, the E-field probe is used, which measures the E-field radial to the probe axis, as shown in Fig. 3.3a). The probe is connected by fiber optics to a remote unit that is connected to a measurement receiver such as a network analyzer. The probe consists of a dipole located at the tip of the probe, with a tip to dipole center distance of 1.55 mm. The probe length is 433 mm. The probe allows the direct measurement of the amplitude and phase of the desired E-field component.
Calibration within TSM is not available at the time the measurements for this thesis were made. Therefore, the results from the TDS system can only be used to validate the phase distribution. For the amplitude, only the relative results are used, and only for small E-field values, since the probe results are not linear with the E-field.

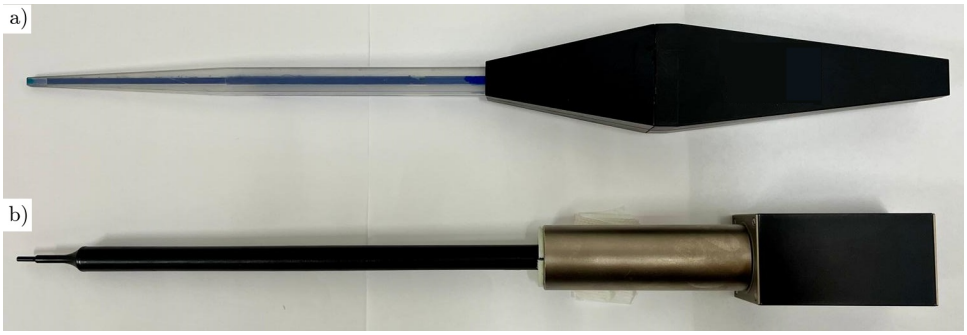

Figure 3.3: The a) TDS probe for measuring the z-component of the E-field in amplitude and phase and b) Easy 6 probe for measuring the rms value of the total E-field.

The second available E-field measurement system is the Easy 4/6 system from SPEAG [50]. During the time of this work, the Easy system was updated from Easy 4 to Easy 6. The update included a new Data Acquisition Electronics (DAE) connected to the probe and a new software. However, the probe itself did not change. The Easy 4 system had its own Easy 4 device, that is based on a PC, to which the probe is connected via the Easy electric over fiber (EoF) cable. The Easy 6 probe is connected to the new DAE, which is connected via EoF to a remote unit (Easy-RU) that converts the optical signal to an electrical signal and is connected to a PC,

where the software is installed. The Easy 6 probe is presented in Fig. 3.3b).
The probe used in this work is the EX3D SAR probe. This dosimetric near-field probe, measures the SAR and the E_{rms}-field. The tip diameter is 2.5 mm, for a length of 20 mm. The total length of the probe is 337 mm, and the distance between the probe tip and the dipole center is 1 mm. The size of the DAE changed from 60x60x67.5 mm for the Easy 4 system to 38x38x72 mm for the Easy 6 system. The total length of the probe parts placed inside the coil consists of the probe, the DAE, the connector and the cable, which should not be bent too much. Depending on the placement position in the exposure system, the measurement volume is limited.
Establishing a measurement setup in which the Easy probe produces reliable results is part of this work and will be discussed in the following section 3.2.1.

To measure the temperature in the phantom, two types of fiber optic temperature probes are used in this work. The TS2P probe and the TS5 probe are fiber optic temperature probes from WEIDMANN Technologies Deutschland GmbH (WEIDMANN), which consist of a gallium arsenide (GaAs) crystal, attached to a fiber optic cable that can be connected to the fiber optic temperature measurement device (FOTEMP). Both types of probes have an accuracy of $\pm 0.2\,^{\circ}\mathrm{C}$ and a resolution of $0.1\,^{\circ}\mathrm{C}$. The crystal diameter is 0.55 mm. The difference between the two types of probes is that the TS2P has the crystal directly at the tip of the probe and the TS5 has the crystal embedded in a coating material as shown in Fig. 3.4 on the left side.

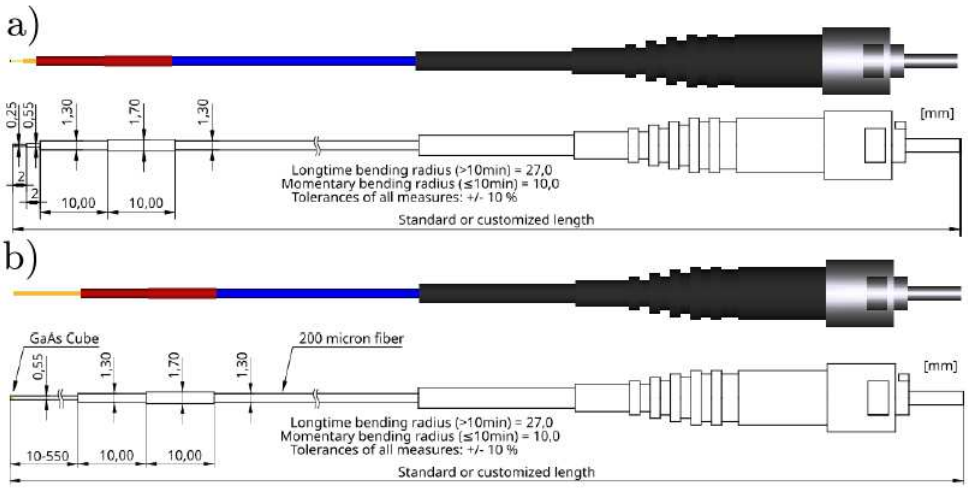

Figure 3.4: Schematic representation of the two different temperature probes used in this work. In a) the TS2P probe with an open crystal at the tip on the left side and in b) the TS5 probe with an embedded crystal at a defined distance from the tip inside the orange part [51, 52].

To fix and move the different types of probes inside the exposure system, several 3D printed probe holders are constructed. These holders can optionally be fixed to a movement system. This movement system was built as a bachelor thesis and the design is based on a 3D printer [53]. The system is mostly placed around the exposure system, with a traverse placed inside the coil. The design is displayed in Fig. 3.5. The BC is shielded, so that the frame of the system does not interfere with

the E-field inside the coil. The material of the traverse is polyvinyl chloride (PVC) to minimize any E-field distortion.

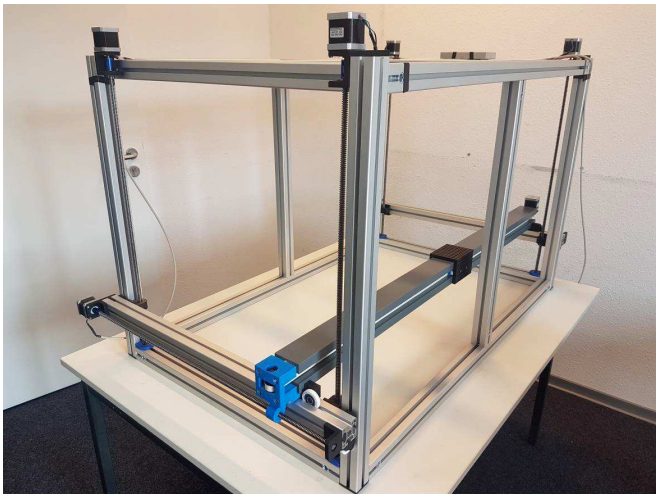

Figure 3.5: Overview of the movement system that can be placed around the exposure systems to move the probes, which can be attached to the carriage in black, in the three spatial directions.

As presented in Fig. 3.5, the traverse is fixed at both ends, which are moved in x-direction by two step motors. The movement in y-direction is done by four step motors. There is a movable carriage on the traverse to which the probes can be attached. The system is controlled using G-code to move the carriage in all directions. The smallest movement step is 0.1 mm and the movement range is 500 mm in x-direction, 700 mm in y-direction and 1200 mm in z-direction. The system is used for E-field mapping measurements where the probe is moved continuously through the phantom or to place a probe at a precise position within the phantom.

In a typical measurement setup where the E_{rms}-field is measured, the ASTM phantom is placed in the BC, so that the isocenter of the coil is aligned with the isocenter of the TSM inside the phantom at [325/45/210] as x-, y- and z-coordinates in mm relative to the origin marked in Fig. 3.6. The traverse is placed above the phantom and the E_{rms}-field probe is attached to the carriage. Due to the size of the probe and the traverse and the limited space inside the coil above the phantom, the E_{rms}-field probe can only be placed in a small area of the phantom. In addition, the tilt angle of the probe limits the measurement volume. In the case where the E_{rms}-field probe is mounted parallel to the traverse, a little more than a quarter of the xz-plane can be measured without rearranging. If the probe is placed perpendicular to the traverse, the entire phantom is accessible in the z-direction, but only a limited area in the x-direction. The areas that can be measured with the two probe placements are illustrated in Fig. 3.6, including the typical test object and reference position. The green area corresponds to the measurement volume that can be reached without repositioning the probe. There is no way to measure the entire E_{rms}-field distribution in the BC with one setup. As mentioned above, it is almost impossible to create exactly the same measurement conditions after turning the system off and on again. When measuring passive implants, where the object placement is always in the same phantom area, the E_{rms}-field distribution can be measured and determined with one

setup. However, during a measurement with a TO in place, the E_{rms}-field probe is placed on the opposite side of the phantom from the TO, as indicated in Fig. 3.6. Due to the fact that it is not possible to measure the E_{rms}-field value on both sides simultaneously, the informative value for the absolute E_{rms}-field value at the TO position may be limited.

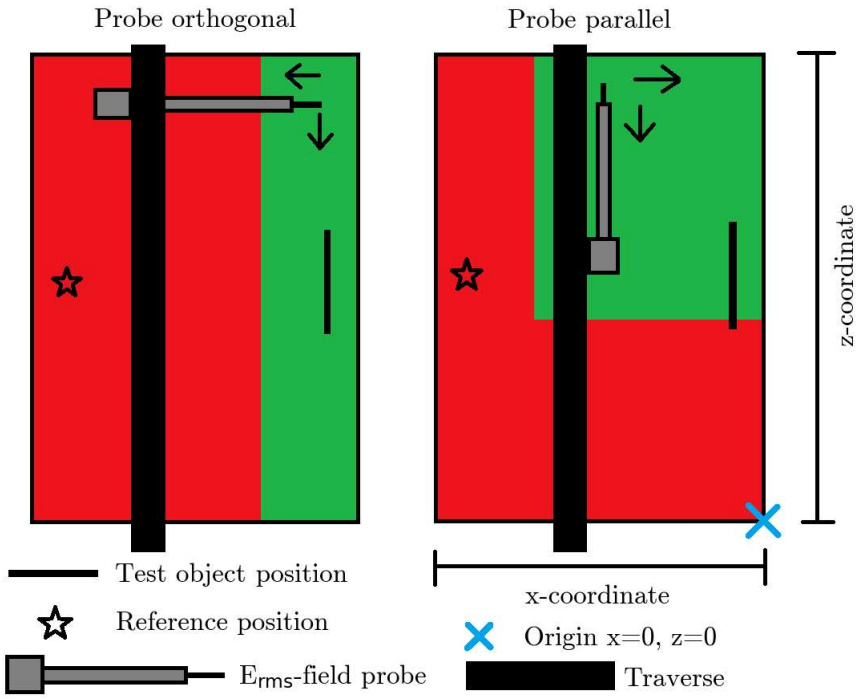

Figure 3.6: Schematic overview of the accessible measurement area in green of the phantom inside the BC depending on the probe orientation and fixation in parallel or orthogonal to the traverse of the movement system, including the standard test object position, the reference position and the origin in x- and z-coordinate for the isoplane at $y = 45\,\mathrm{mm}$.

The Tier 3 power deposition determination for active implants is based on the agreement between the E_{rms}-field distribution inside the exposure system and its numerical prediction. Therefore, the E_{rms}-field distribution must be measured for the entire measurement volume. Without the ability to measure the entire distribution with a single measurement setup, the comparability between the individually measured parts is limited and may increase the overall uncertainties for the TF validation procedure.

In addition, as described in section 2.3, the homogeneity of the E_{rms}-field distribution should be within $\pm 1\,\mathrm{dB}$ over the entire TO volume. The E_{rms}-field distribution for the area, where the TOs are typically placed in a BC was measured with the Easy 4/6 probe fixed in orthogonal orientation and displayed in Fig. 3.7, including the $\pm 1\,\mathrm{dB}$ lines. The distribution shows the expected E_{rms}-field distribution for a BC inside the ASTM phantom from Annex M in Ref. [4]. The comparison with internal numerical simulations of the BC is in good agreement, at least for the measured part of the phantom. The mean value of the relative difference between the numerical prediction and the measured values is $-0.79 \pm 3.25\,\%$. This shows

that the distribution is reliable, at least for this part of the phantom. The relative deviation distribution has a systematic error of about 2-3 mm due to a position shift in the z-direction caused by the limited access of the BC to precisely place the probe.

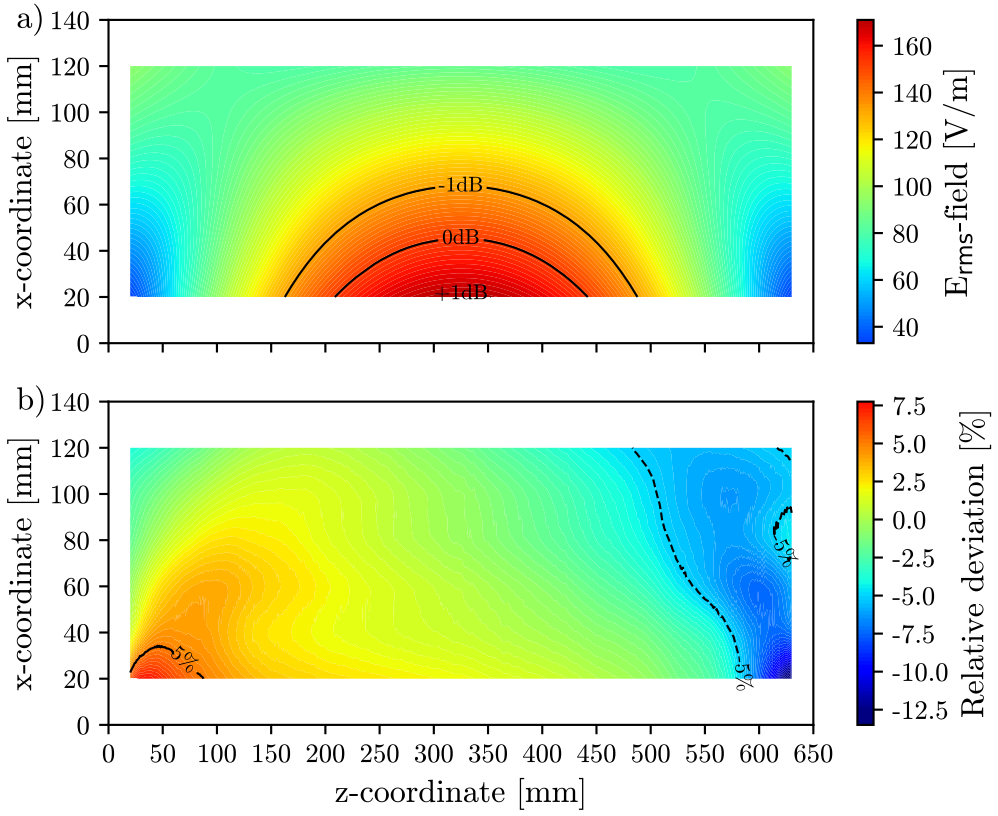

Figure 3.7: The E_{rms}-field distribution of the isoplane within the possible measurement area with orthogonal orientated probe, including the ± 1 dB isolines for the measurement position at 20 mm distance to the phantom wall in a) and their relative deviation compared to the numerical predictions in b).

The requirements of the test methods for the implant position are at least 20 mm distance to any surface or phantom wall and the homogeneity of the E_{rms}-field distribution over the entire implant volume should be within ± 1 dB. The distribution in Fig. 3.7 proofs, that the highest E_{rms}-field value within the measurement volume is at 20 mm. Therefore, placing the TO at this position will result in the best SNR and the highest ΔT possible for a given input power. The distribution also shows a strong field gradient along the x-axis. Assuming that the highest E_{rms}-field value along the z-line at 20 mm distance is the value corresponding to +1 dB, the length of the homogeneous part of the line is ± 150 mm. For a TO width of 20 mm, this length is reduced to ± 125 mm, and for a width of 40 mm, the length is reduced to ± 60 mm. TOs exceeding these dimensions, are outside the homogeneity requirements of Ref. [3]. Additional testing is required in this case. For a frequency of 64 MHz, TOs with a length of half the resonance wavelength inside the medium

are expected to produce the highest ΔT. This length for 64 MHz is approximately 250 mm [54].
The measured ΔT of each TO is scaled to the mean incident E_{rms}-field over the entire TO volume, i.e. the local SAR, before the results are applied to the *in vivo* conditions. Therefore, the uncertainty of the predicted ΔT is lower for a more homogeneous E_{rms}-field distribution. For the given E_{rms}-field distribution, several TOs exceed the dimensions for which the homogeneity requirement is fulfilled, increasing the uncertainty or the measurement and investigation effort.
In the next section the general probe behavior and the optimal use for the different probes are investigated.

3.2 Investigation of the typical hot spot distribution

There are several methods recommended by ISO/TS [4] to determine the spatial power distribution of a hot spot. One can either use numerical predictions and validate the predicted distributions with a number of measurement points, or one can measure the full 3D distribution with an E_{rms}-field probe, a SAR probe or a temperature probe.
This chapter examines the behavior of the E_{rms}-field probe and the temperature probes and evaluates their suitability for measuring the 3D hot spot distribution. First, the optimal probe placement and movement is determined to provide reliable measurement results. Based on this, the hot spot distribution and its influences are tested. A typical active implant consists of one or more leads with one or more electrodes at the lead tips, which represent the potential hot spot of the implant. To represent such an implant, a 500 mm long straight lead with eight electrodes spaced 5 mm apart is used as the TO. This TO is chosen as an abstract object to investigate the possible radial symmetry of the hot spot around the electrodes in order to reduce the required measurement volume from 3D to 2D. As a final step, the radial E_{rms}-field distribution is investigated and evaluated whether the probe position along the electrode has any influence on the radial E_{rms}-field distribution at this location. In addition, different combinations of active electrodes and different input power ratios between them are applied. Depending on the extent of influence of these factors on the E_{rms}-field distribution, it may be possible to further reduce the measurement volume and calculate the power deposition from a few measurement lines, thus saving considerable measurement time.

3.2.1 Influence of probe orientation and behavior

Due to the limited space inside the BC, the probe position and the resulting reachable measurement volume depend on the probe orientation. Therefore, it is necessary to determine the measurement conditions under which the probes provide reliable and repeatable results.
To simplify the measurement setup, the measurements were performed in a smaller phantom of 140x95x190 mm filled with 90 mm saline solution outside the exposure systems and the RF cabin. Instead of generating a power deposition around the electrodes by E-field exposure inside a radiating exposure system, one can generate a power deposition around the electrodes by directly injecting a voltage into the

power supply wires of the electrodes. The 500 mm long straight multi-electrode lead with eight 3 mm long electrodes is used as the test object and the power is injected directly into the wires. The electrodes are potential individual hot spots and therefore suitable for evaluating the probes.
A schematic setup with the possible directions of probe movement is shown in Fig. 3.8. The TO was placed horizontally in saline solution in the phantom. The phantom was attached to a print plate of a 3D printer. The probes were attached to the nozzle of the printer and moved. Measurements were made with the Easy 4/6 E_{rms}-field probe and with the TS2P temperature probe.
First, the dependence of the probe rotation on the E_{rms}-field is investigated. The E_{rms}-field probe was placed as close as possible above and lateral to the injected electrode of the TO and rotated around its own axis in 10° steps to measure the E_{rms}-field three times for each angle. The effective distance between the TO and the sensitive element of the E_{rms}-field probe was estimated to be about 1-2 mm. The injected voltage at 64 MHz was set to 5 Vpp for the first electrode only and was left on for the entire measurement.

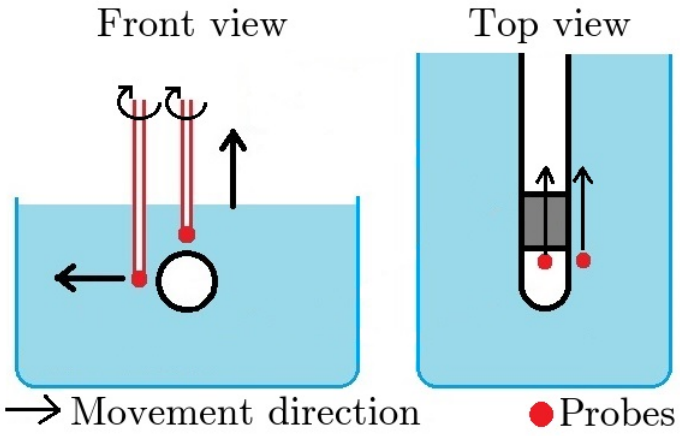

Figure 3.8: Schematic overview of the measurement setup with the test object including the active electrode (gray) and the probe placement (red) and possible movement directions (black arrows) inside the smaller phantom (blue) in front and top view.

The E_{rms}-field for each angle of rotation for both positions above and lateral to the TO are visible in Fig. 3.9. The E_{rms}-field measurement lateral to the TO is strongly dependent on the rotation angle of the E_{rms}-field probe. The minimum E_{rms}-field is $109.98 \pm 0.74\,\mathrm{V/m}$, which is 71.54 % of the maximum E_{rms}-field of $153.72 \pm 0.39\,\mathrm{V/m}$ for the lateral position. The behavior is symmetrical for each 120° rotation. For the E_{rms}-field probe placement above the TO, no rotation angle dependence is visible and the measured value is stable at $152.88 \pm 0.51\,\mathrm{V/m}$ over all angles.
These results clearly indicate, that the Easy 4/6 E_{rms}-field probe should be placed above or orthogonal to the TO to obtain stable E_{rms}-field values regardless of the rotation of the E_{rms}-field probe.

As the next measurement step, the E_{rms}-field probe was moved along the electrode to represent rotation angles of 10°, 70°, and above the electrode. The results of the E_{rms}-field along the electrode are presented in Fig. 3.10.
Not only does the maximum E_{rms}-field value change with rotation angle and position,

but also the width where an E_{rms}-field increase is measured. The shape of the measured curves varied substantially for 10° and 70° and is only repeatable for the position above the electrode. Therefore, the E_{rms}-field must be placed orthogonal to the TO at all times.

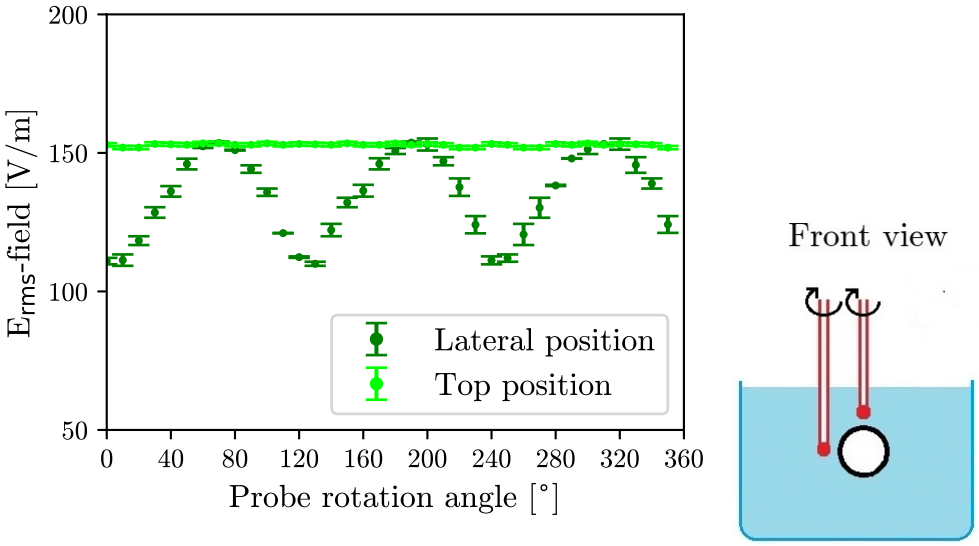

Figure 3.9: Measurement results of the E_{rms}-field depending on the probe angle for the two positions of the probe to the electrode, modified from Ref. [7].

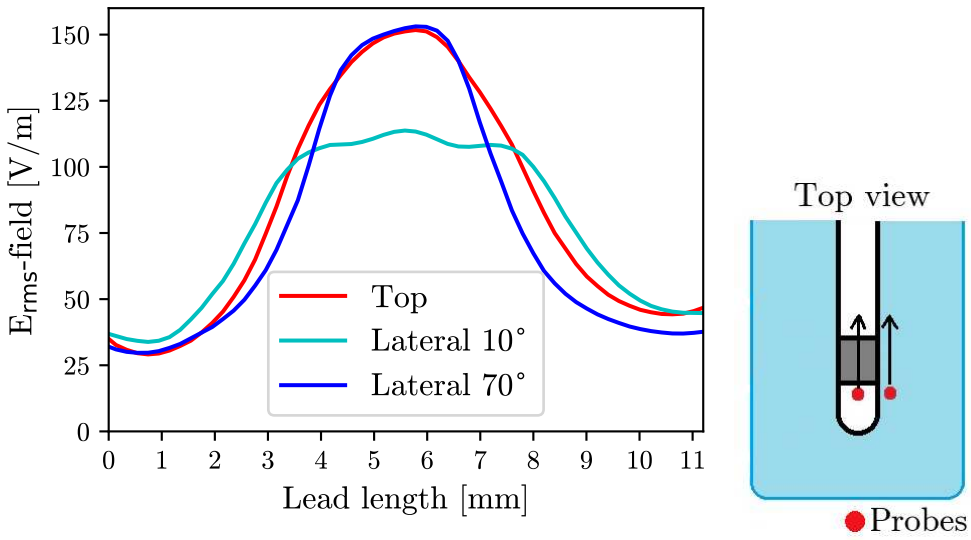

Figure 3.10: The E_{rms}-field distribution along the active electrode of the test object for different E_{rms}-field probe angles 10° and 70° at lateral probe position and the top position as reference.

To investigate the effect of probe placement, the temperature probe was also placed above and to the side of the TO. However, instead of rotating the temperature probe, it was moved radially away from the TO. For this, the temperature probe

was placed in the center of the electrode. The temperature crystal is symmetric and therefore not angle dependent. Thus, the temperature distribution and the influence of possible convection are investigated. In total, eleven positions with different distances per temperature probe placement were measured, with the largest distance being 5 mm. The injected voltage was turned on for 30 seconds. Each position was measured three times to compensate for variations and to calculate the mean and standard deviation. The results for the different probe positions, where the temperature probe was placed above the electrode are presented in Fig. 3.11 for the smallest distance at 0 mm and the largest at 5 mm.

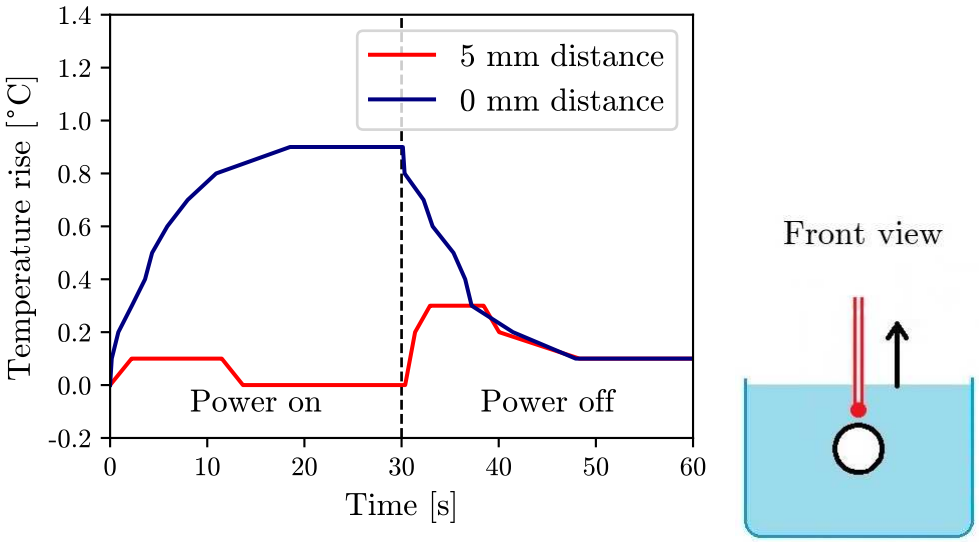

Figure 3.11: Measurement results for the temperature rise ΔT for 0 mm and 5 mm distances of the temperature probe to the electrode over 60 s where the power is turned on for the first 30 s.

The progression of the temperature over time shows a second temperature rise after turning the power off. This second temperature rise is not caused by the injected power, but can be explained by convection. The effect is worse for the position above the electrode, as expected, because the warmer medium moves upward and can be measured by the temperature probe when it is placed above the TO. The temperature rise due to convection can add to the temperature rise due to the injected power and therefore overestimate the measured temperature rise at greater distances. If only the temperature rise due to the injected power contributes to the measured temperature rise, the temperature should decrease after the power is turned off. Therefore, the temperature probe should be moved laterally to the electrode if it is to be used to measure the hot spot distribution in the radial direction. As a final step, the radial E_{rms}-field distribution was also measured with the E_{rms}-field probe in the radial direction above the TO. It was also placed above the center of the electrode. The radial distance was increased in 0.2 mm increments up to a total distance of 10 mm. To compare the measured E_{rms}-field values above the TO with the temperature values beside the TO, the temperature values are recalculated

to E_{rms}-field values using the following equation

$$E_{\mathrm{rms}} = \sqrt{\frac{\Delta T}{\Delta t}\frac{c\rho}{\sigma}} \tag{3.2.1}$$

where ρ is the density, σ the electrical conductivity and c the local heat capacity of the TSM. The ΔT is calculated for the first 10 seconds of each measurement. The results are illustrated in Fig. 3.12.

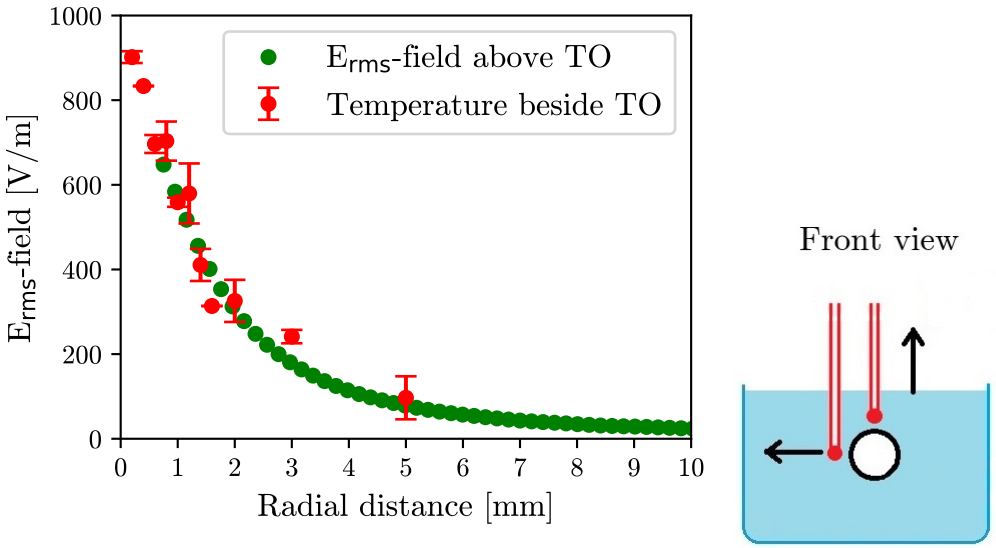

Figure 3.12: Comparison of the measured E_{rms}-field values above and the converted temperature values besides of the electrode for the radial distribution, modified from Ref. [6].

The measured E_{rms}-field values in green and the converted temperature values in red are in good agreement. Therefore, the orientation for both measurement probe types is determined for all further measurements. Whether the apparent symmetry of the distribution for the two positions is valid for each radial direction is investigated in the next section.

3.2.2 Radial symmetry of the hot spot distribution

The next step is to investigate the E_{rms}-field distribution of a hot spot. The first step is to determine if the hot spot distribution is radially symmetric or if it depends on the internal structure of the lead, e.g. the lead wires. For this measurement, the same multi-electrode lead is used as the test object in the same measurement setup. This time, the second and fourth electrodes are chosen for this investigation because they have a different number of supply wires in close proximity and enough distance between them to avoid coupling effects between the injected electrodes. A total of five measurement runs were performed. After each measurement run, the lead was rotated around its own axis so that position 1 corresponded to the orientation where the power supply for electrode 1 was at the top of the lead and therefore closest to the measurement probe. For position 2, the lead was rotated so that the

power supply for electrode 2 was at the top of the lead. The current supply wire per electrode is shown schematically in Fig. 3.13.

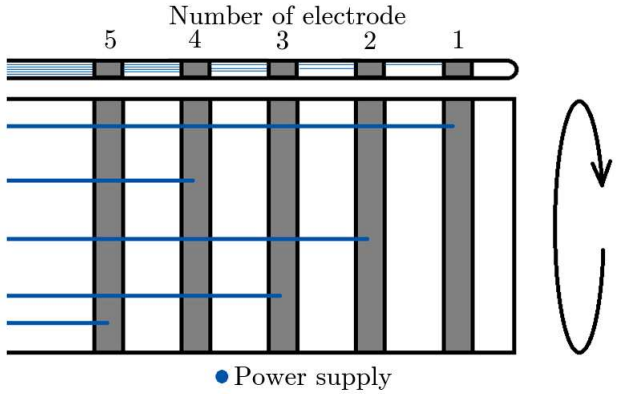

Figure 3.13: Schematic overview of the order of the power supply wires for the first five electrodes of the test object, shown for the unrolled TO.

For each measured position the E_{rms}-field probe was placed above the TO and moved along it, starting at the rear end of the fourth electrode and ending at the front end of the second electrode. The measurement was performed five times for each position to calculate the mean value and its standard deviation. The results are displayed in Fig. 3.14.

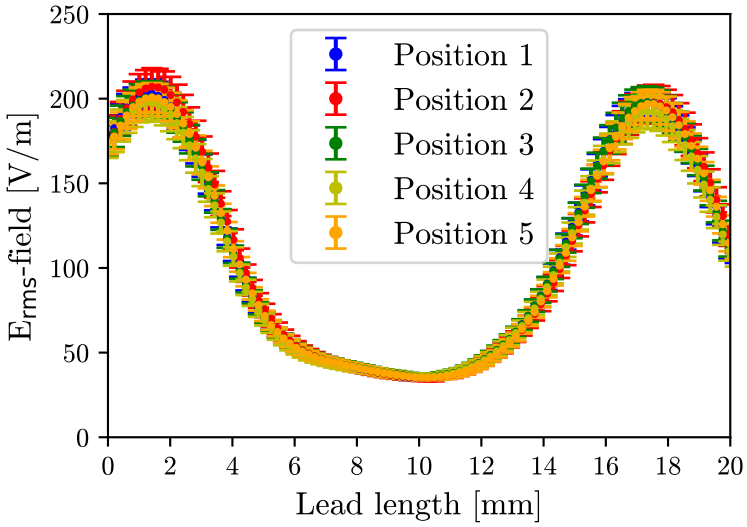

Figure 3.14: Measurement results of the distribution of the E_{rms}-field along the test object for five different test object rotations, as electrode two and four are active, modified from Ref. [6].

The measured E_{rms}-field distribution along the lead does not depend on the rotation of the lead and is radially symmetric. Measurements of the same position at different angles of rotation are consistent within their measurement uncertainties. The position of the E_{rms}-field probe and its movement are the largest factors in the

measurement uncertainty, which is between 4.11 % and 5.30 % for all five positions. The hot spot distribution can be assumed to be radially symmetric for this particular TO and probably for straight leads in general. Further investigation may be required for helical leads. In this work, however, only straight leads are used as TOs to generate the E_{rms}-field distribution and to investigate probe behavior and optimal measurement setups for measuring hot spot distributions or point-by-point measurements.

3.2.3 Influences on the hot spot expansion

After establishing that the hot spot distribution is radially symmetric for the TO used, the two-dimensional hot spot distribution along and in the radial direction is examined to assess whether the distribution in the radial direction depends on whether the E_{rms}-field probe is placed at the edge or in the center of the electrode. If it can be shown that the E_{rms}-field distribution does not depend on this position, it may be sufficient to measure only a few lines and calculate the 3D power deposition from the measurement instead of measuring the full 3D distribution.
For this investigation, the same TO and the same setup are used as before. The TO was placed in saline solution and the spatial distribution of the hot spot was measured with the E_{rms}-field probe, fixed to the movement system of the 3D printer. To measure the entire distribution of the hot spot of both the second and the fourth injected electrodes, the E_{rms}-field probe was placed above the TO and moved in the radial direction. The E_{rms}-field probe was moved continuously at 0.2 mm/s, measuring the E_{rms}-field value every second up to a total distance of 10 mm. The E_{rms}-field probe was then moved 0.1 mm along the lead. For each 0.1 mm step along the electrode, a line was measured in the radial direction. As a result, a two-dimensional E_{rms}-field plane was measured above the electrodes, as schematically displayed in Fig. 3.15.

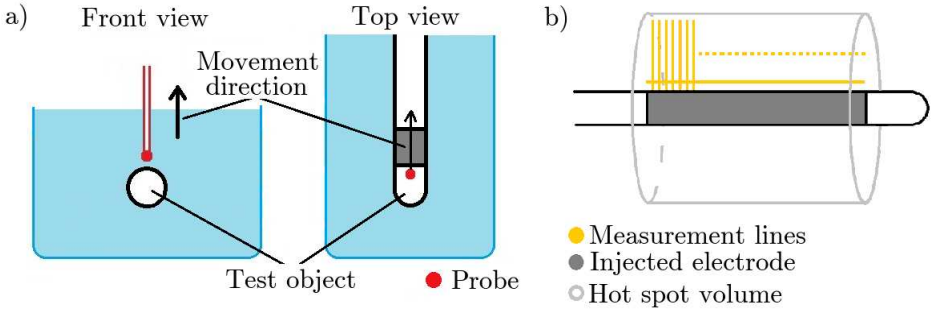

Figure 3.15: Schematic overview of the measurement setup of the test object and measurement probe inside the phantom in a) and the measurement volume (light gray) and measurement lines (orange) around the injected electrode (gray) in b), modified from Ref. [8].

Each line measured in the radial direction was normalized to its own maximum at the closest proximity to the electrode to compare the relative distribution in the radial direction per position. In addition, a close-proximity measurement was made along the lead. The results for both measurements along and in the radial direction when electrodes two and four are injected are shown in Fig. 3.16. The

E_{rms}-field distribution along the TO in Fig. 3.16a) increases in the vicinity of the injected electrodes. Compared to Fig. 3.14, the different distance between the TO and the E_{rms}-field probe results in a higher measured maximum of the E_{rms}-field, as expected.

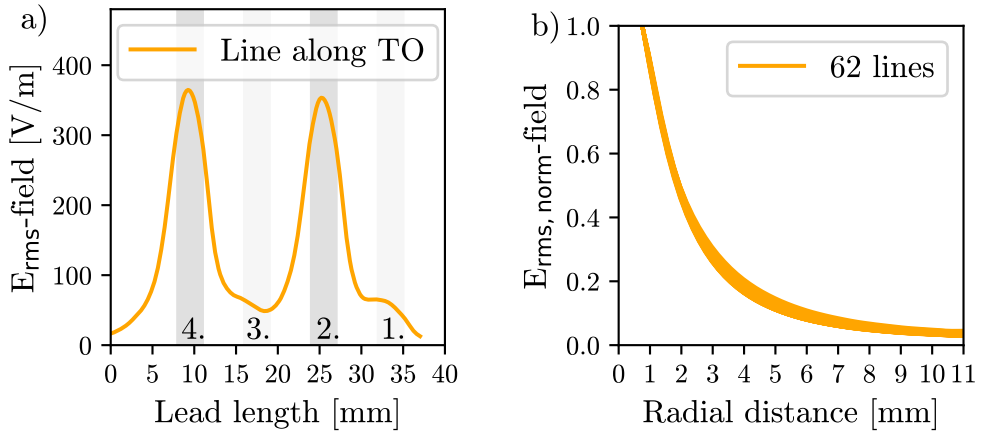

Figure 3.16: The E_{rms}-field distribution in a) along the test object for the second and fourth injected electrode highlighted in dark gray and in b) the normalized E_{rms}-field in radial direction for 31 positions along each injected electrode, modified from Ref. [8].

The radially measured normalized lines along the two electrodes are compared to see if the progression of the lines along the electrode varies depending on the position. Fig. 3.16b) shows a similar E_{rms}-field decrease along the electrode or between the two electrodes with a mean standard deviation of 6.44 %.
This measurement was performed for different combinations of two of the eight injected electrodes (2./4., 1./3., 1./4., 2./3.) and for different injection power ratios between the electrodes between 3 Vpp and 5 Vpp in ten different combinations to evaluate their influence on the radial E_{rms}-field distribution. The measured E_{rms}-field curves for the different electrode combinations and power ratios are individually normalized and compared to each other and to the curves in Fig. 3.16b). The results for all measured lines are displayed in Fig. 3.17.
The data demonstrates once again that the radial distribution of the E_{rms}-field does not depend on the combination of the injected electrodes nor on the power ratio between them.

To evaluate whether this behavior can be transferred to a radiated setup in the BC, an additional measurement was performed inside the BC. The TO was placed in the ASTM phantom at a distance of 20 mm from the phantom wall in TSM. As discussed in section 3.2.1, the E_{rms}-field probe must be placed orthogonal to the TO and moved radially to produce reliable results. Since the placement options of the E_{rms}-field probe inside the coil are limited due to space constraints, the E_{rms}-field probe cannot be placed above the lead, but at a 30° angle. The distance was increased step wise in y- and x-direction, calculated with sine and cosine, to increase the radial distance in the desired steps. The starting point was as close as possible to the electrode at the maximum E_{rms}-field value along it. The radial distance was increased to a total distance of 10 mm.

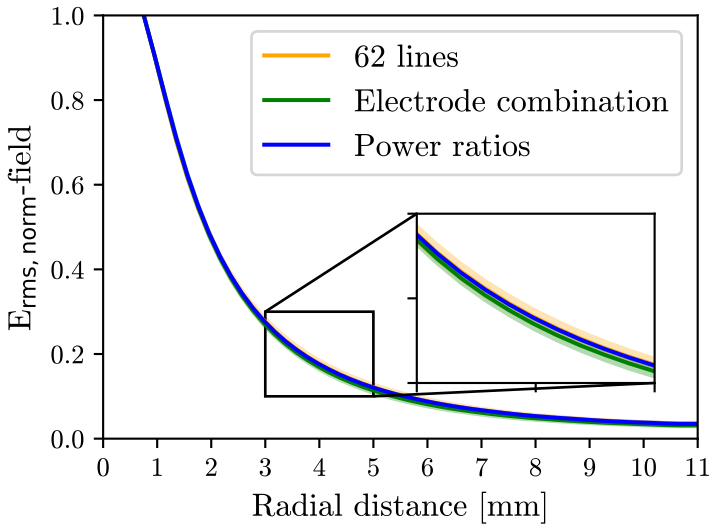

Figure 3.17: The mean normalized radial E_{rms}-field distributions including the $\pm 1\sigma$-error band for all measurement lines of the two injected electrodes including different electrode combination and different power ratios of the injected electrodes, modified from Ref. [8].

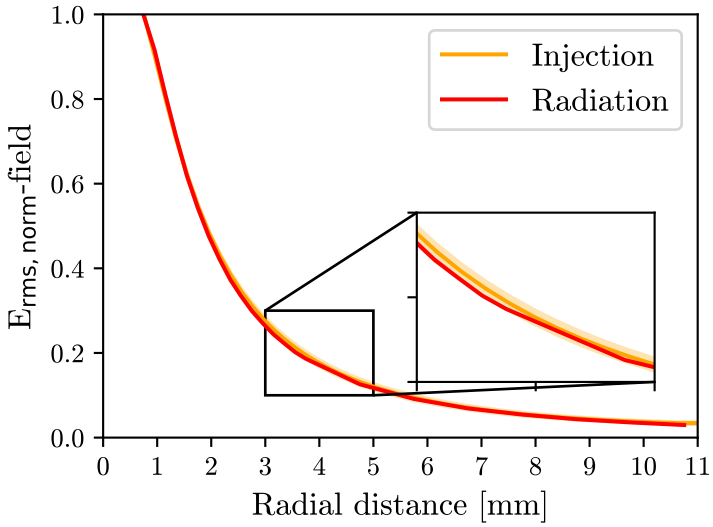

Figure 3.18: The mean normalized radial E_{rms}-field distributions including the $\pm 1\sigma$-error band for the measurements in the injected setup and the measured normalized radial E_{rms}-field in the radiated setup in the body coil, modified from Ref. [8].

To subtract the incident E_{rms}-field, this measurement was performed with and without the TO in place. The mean values and standard deviations of the measured lines in the injected setup in Fig. 3.17 are calculated and compared with the mean results of the measurement in the irradiated setup in BC. The resulting E_{rms}-fields are shown in Fig. 3.18.

The E_{rms}-field of the injected setup and the E_{rms}-field of the radiated setup are in good agreement. It is therefore possible to generate a normalized model function describing the radial E_{rms}-field distribution from a small number of radial lines measured in an injection setup. The measurement along the line at a defined distance can then be used to scale the model to each individual position.
To test this assumption, additional calculations are performed using the measurement lines presented in Fig. 3.16b). For each electrode, 31 radial lines are normalized. The resulting E_{rms}-field distribution over the plane is compared with the results calculated using the averaged measurement line describing the radial E_{rms}-field distribution, which represents the case where only a few radial lines are measured and averaged. The measured distribution over the two electrodes, the calculated distribution from the averaged line and the deviation between them for the first radial 6 mm are displayed in Fig. 3.19.

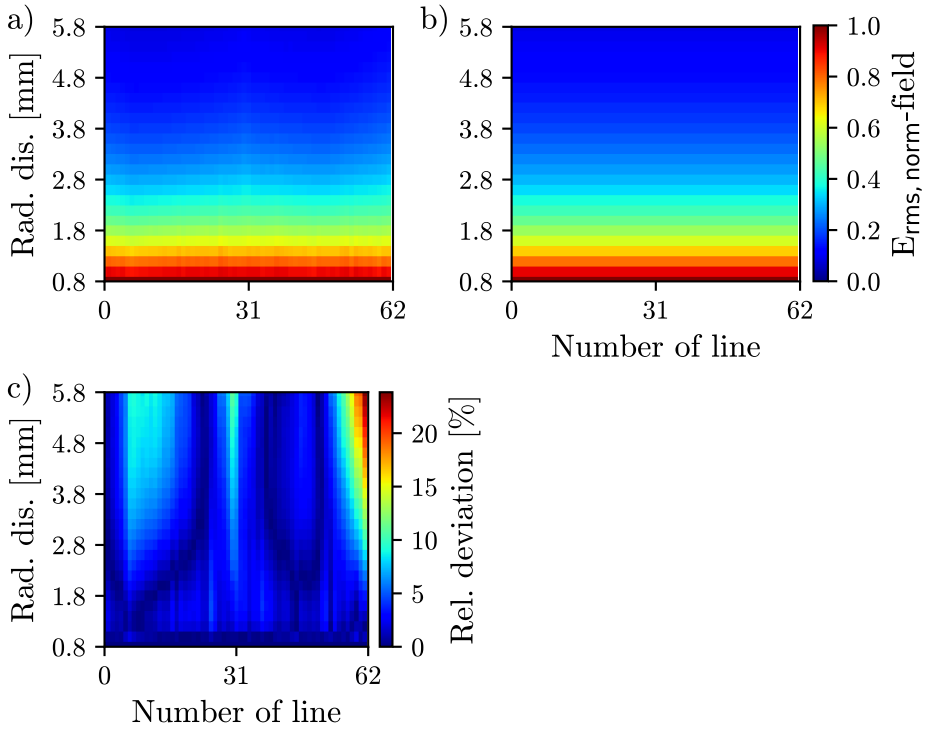

Figure 3.19: The a) measured and b) calculated normalized E_{rms}-field distribution for the 2D plane above the two electrodes in radial distance and c) the relative deviation between them, modified from Ref. [8].

There is only a small deviation between the measured and calculated hot spot distribution, with an average deviation of 3.4 % over the entire plane. The deviation is higher at larger distances from the electrodes, where the E_{rms}-field has already decreased substantially.
Therefore, the hot spot distribution can be calculated from a model function describing the radial E_{rms}-field decrease, that can be obtained from a small number of radial measurements. This model should be normalized to a certain distance from the TO. At this distance, a measurement should be made along the entire lead. The model function can then be scaled to each value along the lead. Due to the radial

symmetry of the distribution, the power deposition can be calculated from the scaled model function using the cylindrical geometry. For each increment along the TO, the corresponding circular disk can be calculated and added up to the total volume. To cover the values at a distance of less than 1 mm from the TO, which the E_{rms}-field probe cannot reach, additional temperature measurements are recommended. For this study, three additional measurement points were measured. The temperature probe was placed in the center of the electrode and the ΔT was measured for 10 seconds and recalculated to the corresponding E_{rms}-field value, as described above. The model function used to describe the radial decrease was obtained and modified from the electric field theory and the distance square law

$$y \sim \frac{1}{r^2}. \tag{3.2.2}$$

The results of the temperature measurement and the resulting model function are shown in Fig. 3.20.

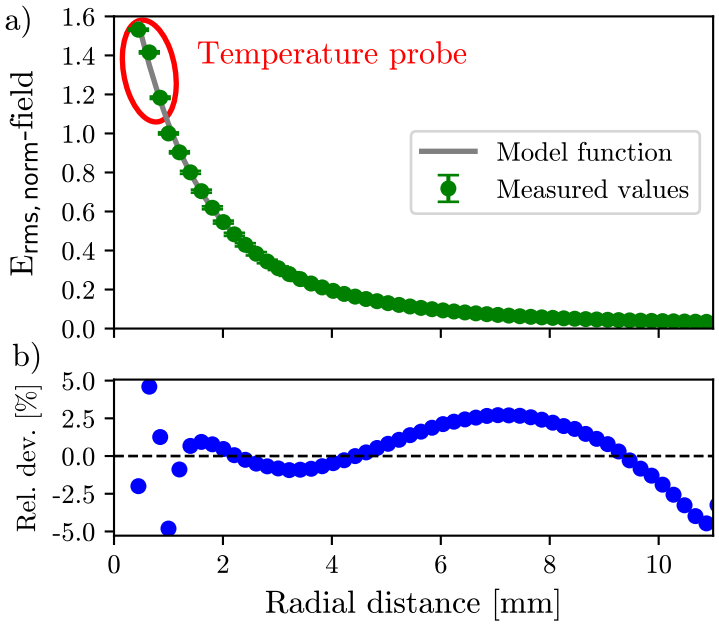

Figure 3.20: The combined measurement results of the E_{rms}-field values and the ΔT values and the resulting model function describing the radial distribution in a) and the relative deviation between them in b), modified from Ref. [8].

The resulting model function had the form

$$y = \frac{a}{(-1.5 - x)^3} + \frac{b}{(-1.5 - x)^2} + \frac{c}{(-1.5 - x)} + d, \tag{3.2.3}$$

where $a = 12.39 \pm 1.25$, $b = 15.47 \pm 1.03$, $c = 1.80 \pm 0.25$, and $d = 0.09 \pm 0.02$. The model describes the measured values with a mean value and its standard deviation of $0.24 \pm 1.98\,\%$. The deviation increases for the values measured with the temperature probe and varies between $+4.60\,\%$ and $-4.81\,\%$ The additional data points measured with the temperature probe are necessary to describe the radial decrease and to cover

the small distances to the TO, where typically the highest power deposition occurs. This study demonstrates, that the hot spot E_{rms}-field distribution of an electrode of a multi-electrode straight lead is independent on the radial direction. The radial E_{rms}-field decrease shows a similar behavior independent of the starting position along the electrode and did not vary for the injection of different pairs of electrodes and not for different power levels between the injected electrodes. Therefore, a normalized model function can be obtained from a small number of radial measurement lines and a small number of temperature measurements. This model can be scaled to measurement values along the TO at a defined distance and the power deposition can be calculated using geometric calculations and numerical integration.
It is shown, that the deviation between the measured distribution of the plane above the injected electrodes and the reconstructed distribution from the model function is 3.4 %. Therefore, the time-saving approach of using a smaller number of measurements and a model function does not drastically increase the uncertainty compared to a full 3D measurement. Whether this approach is applicable to all types of leads with electrodes should be investigated by measuring a sufficient number of radial lines and comparing their normalized progression.

3.3 Summary and discussion

This chapter provides an overview of the equipment used for this work. The available body coil used as the RF exposure system is reviewed and its advantages and disadvantages are described. Although the E_{rms}-field distribution generated by the BC is similar to a typical E_{rms}-field distribution of an MR scanner, there is only a small area where the E-field distribution is homogeneous enough for passive implant testing. In addition, the limited space inside the coil makes it impossible to measure the entire E_{rms}-field distribution with a single setup. Due to the sensitivity of the coil and its material to temperature, the state of the coil in terms of resonance frequency and E_{rms}-field distribution changes slightly after it is turned off and on again. This can lead to increased uncertainties in the E_{rms}-field measurement. On the one hand, the E_{rms}-field probe for monitoring and scaling for passive implant testing is placed on the opposite side as the TO, and since both sides cannot be measured under the same coil conditions, it can only be assumed that the distribution is symmetrical.
On the other hand, the agreement between the measured E_{rms}-field distribution measured with multiple setups will be worse compared to a numerically predicted distribution used for testing active implants. This increases the overall uncertainty of the model prediction of the temperature rise of the TO for any given tangential E_{rms}-field along the TO.
As a next step, the behavior of the measurement probes and their limitations were evaluated, and a measurement approach that provides reliable results is developed. It is found that the E_{rms}-field probe should be oriented orthogonal to a TO at all times during a measurement. Due to the limited placement options of the E_{rms}-field probe inside the BC, the position next to a TO is the most practical. However, the angle dependence of the results is too significant, when the E_{rms}-field probe is placed next to the TO. The angle of rotation leads to a possible underestimation of up to about 28 %.
The temperature probe can be placed around the TO at any suitable position in close proximity to the TO. For a measurement where the radial distribution of a

hot spot is of interest, the temperature probe should be placed laterally to the TO to minimize the influence of convection on the results. For the correct orientation and probe placement, the measured E_{rms}-field values and temperature values are comparable and in good agreement in the radial direction.
It is presented, that the hot spot distribution, at least for this tested object, and potentially for all straight leads, is radially symmetric and independent of the position of the power supply cables within the lead. With this confirmation, an approach to reduce the measurement volume from a full 3D measurement to a 2D measurement and potentially to a few lines is evaluated. The results of a large number of radial measurements under different conditions show that the normalized radial E_{rms}-field decrease does not vary over the width of the electrode and is not dependent on the additional injection of neighboring electrodes or different injection power ratios between the electrodes. With one measurement along the TO at a defined distance and a few measurements in the radial direction with a few additional temperature values in close proximity, the entire 3D hot spot distribution can be reconstructed and calculated. This approach can be done outside the MR setup or BC in an injection setup, with no placement limitations.

The findings discussed in this chapter are used and respected for the further measurements of this work. In particular, the knowledge about the correct use of the different probes is taken into account.
The obvious limitations of the BC for testing the extent of RF-induced heating of passive and active implants, due to the limited space for measurement setups, the sensitivity to the temperature of the coil material, the probe positioning, the limited access, and the unsuitable distribution of the E_{rms}-field inside the ASTM phantom, led to the need for another RF exposure system that overcomes the disadvantages of a BC. In the next chapter, a possible solution for an RF exposure system that meets the requirements of the test methods is presented, validated, and compared to the BC system.

4 The advanced dipole-based RF exposure system

4.1 Motivation

The standard system used to test implants for MR safety and compatibility is an MRI scanner or a stand-alone body coil. The primary goal of these systems is to produce a precise, homogeneous magnetic field to achieve the highest possible imaging quality. From an imaging standpoint, the E-field component is an unavoidable by-product that limits the input power levels of the MRI scanner. SAR limits exist depending on the patient's size and weight. These limits may be even more restrictive for patients with implantable medical devices, resulting in reduced image quality.
As described in section 2.2, the RF-induced heating depends on the tangential E-field. The latest version of the ASTM F2182-19 changed the results to be reported from temperature per global SAR to temperature per local SAR or E-field respectively. For the global SAR, the entire phantom volume is taken into account, while for the local SAR only the implant volume is used, which increases the reliability of the measurement results [55]. This opens the possibility to use exposure systems with an E-field distribution that differs from the typical MR scanner distribution.
The requirements described in the ISO/TS [4] and ASTM F2182 [3] declare that the incident E-field variation over the entire implant volume should be less than ± 1 dB with a phase variation less than ± 20 degrees. The ideal E-field distribution should provide nearly uniform tangential E-field incident along the TO. In addition, the E-field within the system used should be stable over time and repeatable on a daily basis.
As shown in section 3.1.2, a BC meets these requirements only for a small area inside the phantom. If the incident field exceeds the ± 1 dB limit, further investigation is required.
In addition to the lack of homogeneity of the incident E-field, the handling of measurements inside a BC is challenging. The diameter of the coil limits the space and placement of measurement equipment. Furthermore, each measurement setup must be assembled in the phantom outside the coil and then moved to the desired position inside the coil. The movement of the test setup can result in small movements of the TOs or probes, increasing the measurement uncertainty. Therefore, a BC is not the ideal solution for testing implants for RF-induced heating.
There are different exposure systems that overcome some of the disadvantages of a BC. The MITS-TT from ZMT [56] is a cylindrical system with 500 mm diameter, generating a E-field of approximately 60 V/m, and is used for TF validation according to Ref. [4]. A second system is a 300x300 mm rectangular E-field generator, introduced in [57] for passive implant testing and used in [58] for TF validation measurements. Due to the smaller size compared to the ASTM phantom, these exposure systems are either limited to a smaller implant sizes or limited in the generated E-field amplitude for sufficient SNR.
In collaboration with the ING Gao, a 64 MHz exposure system was developed with

the size of the ASTM phantom and an E-field where the tangential component should be aligned with the z-axis. The E-field gradient in all three dimensions should be as small as possible, resulting in a measurement volume large enough to cover the range of passive implants with an E-field distribution within ±1 dB. The ING Gao designed and modified a system in the numerical domain until the requirements were fulfilled. After the construction, the system was delivered and had to be validated. Derived from the desired E-field distribution, the system is called the ***L**inear **E**xposure **S**ystem* (LES).
In the following sections, the system is fully validated, including the investigation of the general behavior, the optimal measurement conditions, and the comparison of the measured E-field distribution with the numerically predicted distribution. If the measurement results and the numerical predictions are in sufficient agreement, the numerical predictions can be used for several steps during the testing phase.
For the testing of passive implants, the numerical predictions can be used to calculate the mean incident E-field for the specific implants *in silico* and additionally to calculate the homogeneity. In addition, the optimal position of the implant in the phantom can be determined from the distribution of the numerical predictions. The phase setting and position can be adapted to the implant shape to ensure the maximum homogeneity of the tangential E_{rms}-field along the specific implant.
For the testing of active implants, the numerical predictions are essential. As described in section 2.4, a TF developed to describe the specific active implant is used to predict its temperature rise at the location inside the human body. This TF must be validated, exposing the implant to a set of exposure conditions. The results of the TF prediction, using the tangential E_{rms}-field of the numerical predictions, are then compared to the measurement, where the implant is exposed to the same tangential E_{rms}-fields as in the numerical prediction. The better the agreement between measurement and numerical prediction is, the smaller the uncertainties with which the TF can predict the temperature rise for a given implant.

4.2 Design and technical details

The LES consists of a phantom container and two independent dipole antennas connected to a balun, that balances the circuit. The antennas are attached to the wall along the z-axis with one end plate on each side, as presented in Fig. 4.1. The components of the system are tuned and matched to operate between the first resonance at $\lambda/2$ and the second resonance at $3\lambda/2$. The system is developed to a operating frequency of 64 MHz. The S-parameters, which describe the frequency-dependent reflection per channel S_{11}, S_{22} and the coupling between the two channels S_{12}, S_{21}, are measured with a network analyzer connected to each channel. Tuning changes the resonance frequency and matching adjusts the value of the S-parameters. The S-parameters are displayed in Fig. 4.2. The results of the LES are more broadband than those of the BC. S_{11} is at -28.86 dB, S_{22} at -29.34 dB and $S_{12} = S_{21}$ at -22.86 dB each at 64 MHz. The lower the value of S_{11} and S_{22} the lower the reflection. Compared to the S-parameter of the BC in Fig. 3.2, more signal is transmitted instead of reflected, leading to a better performance.
The phantom container has the same dimensions as the ASTM phantom and can be filled with TSMs of different conductivity up to a height of 90 mm. For measurements, the LES is placed on a table in an RF room.

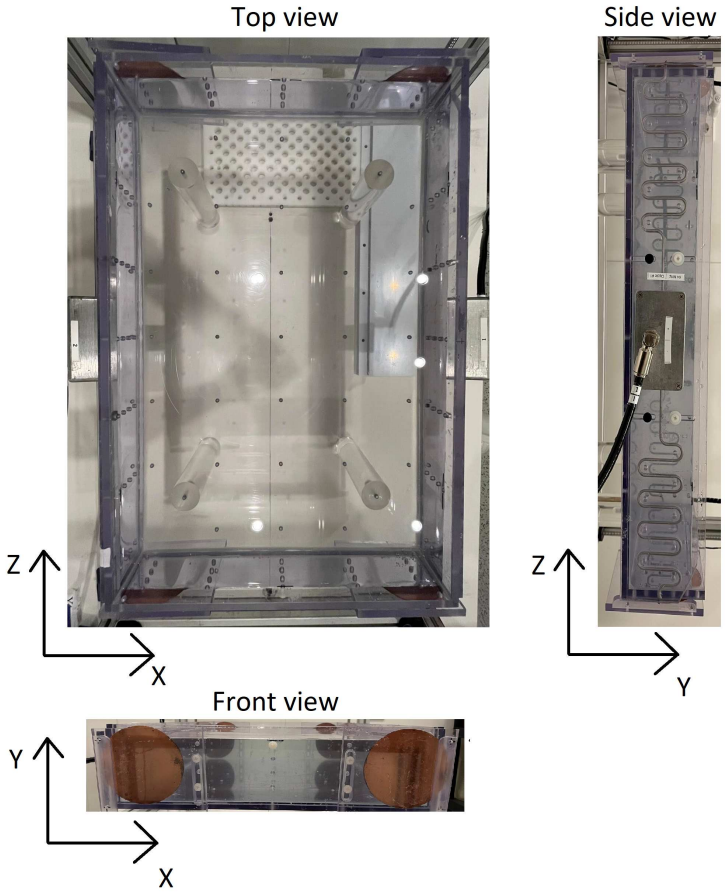

Figure 4.1: Overview of the LES showing the attached dipole antennas and the transparent rectangular phantom in front, side and top view, reused from Ref. [14].

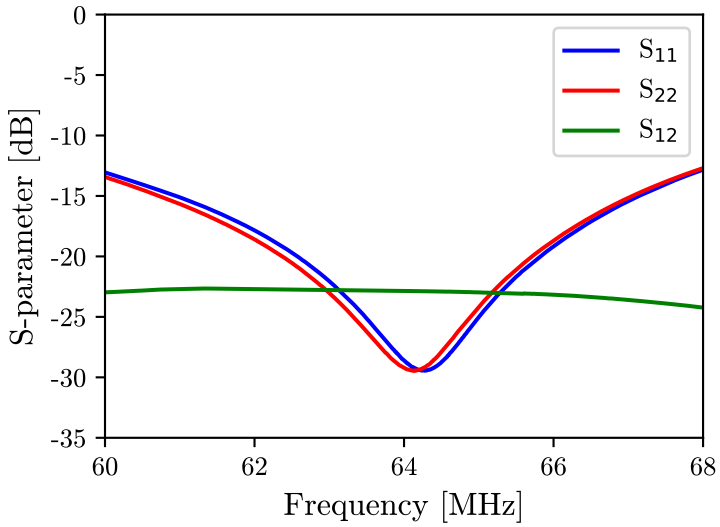

Figure 4.2: S-parameter for the LES for the frequency range between 60 and 68 MHz to determine the resonance frequency and system conditions.

The distance between the phantom and the table is 160 mm and at least one meter to any wall to avoid any possible reflections. In addition, the movement system can be placed around the system. The movement system is described in section 3.1.2 and its minimum distance from the LES components is 200 mm to reduce any E-field disturbances. The system is powered and monitored from the same supply line as the BC.
Numerical predictions of the E-field distribution within saline solution are provided by ING Gao. They include the real and imaginary values for each channel, so that any phase relation between the channels can be calculated.
Compared to the BC, the LES is an open system that provides full access to the phantom during the measurement, allowing optimal probe placement. In addition, the entire phantom volume can be scanned with an E-field probe or a temperature probe in a single setup. The general behavior of the system is examined in the following sections, and further possible advantages are pointed out.

4.3 Validation

To carry out a comprehensive validation, different measurements are performed and discussed in the next sections of this chapter. The LES connected to the supply line is tested for stability, linearity, repeatability, the generated E-field distributions for each channel and the distribution for multiple phase differences between the channels. The measured E_{rms}-field distributions are compared with the numerical predictions and finally a temperature measurement is performed with a standard SAIMD-2 test object according to ISO/TS Annex I to fulfill the requirements of the proposed standard validation for RF exposure systems.

4.3.1 Stability and Linearity

Stability

The first step is to study the general behavior of the system. This includes the stability and the linearity of the E-field, measured for each channel individually and for their combination. The ideal combination of the RF cables and amplifiers is determined. For this, the Easy 4/6 probe measured the E_{rms}-field over time and a fixed position. The phantom was filled with 90 mm saline solution and the E_{rms}-field probe was placed at [20/45/325] for channel 1 and [400/45/325] for channel 2 (CH1 and CH2), respectively. The amplitude was set to −5 dBm and the measurement time was 1000 s per configuration. Two measurements were taken for each channel, one with amplifier 1 and one with amplifier 2 (Amp 1 and Amp 2). The measured E-field values are normalized and compared to determine which combination gives the most similar behavior of the channels. The normalized E_{rms}-field decrease over the measurement time for each combination is presented in Fig. 4.3. To operate both channels simultaneously, there are two possible configurations available: The first where amplifier 1 is connected to channel 1 (blue) and amplifier 2 is connected to channel 2 (purple), and the second where the amplifiers are switched (green and red). Fig. 4.3 shows that the shape of the curves of the two channels is different for the blue-purple configuration, while the shape of the curves of the two channels is similar for the green-red configuration.

After about $10 - 15$ minutes, the E_{rms}-field value remains stable over time.
For all following measurements included in this work, channel 1 is connected to amplifier 2 and vice versa. A warm-up time of 15 minutes is determined to achieve a stable state for all components and therefore a stable E_{rms}-field. The warm-up time is reduced by half compared to the BC in section 3.1.1 because only the amplifiers need time to stabilize.

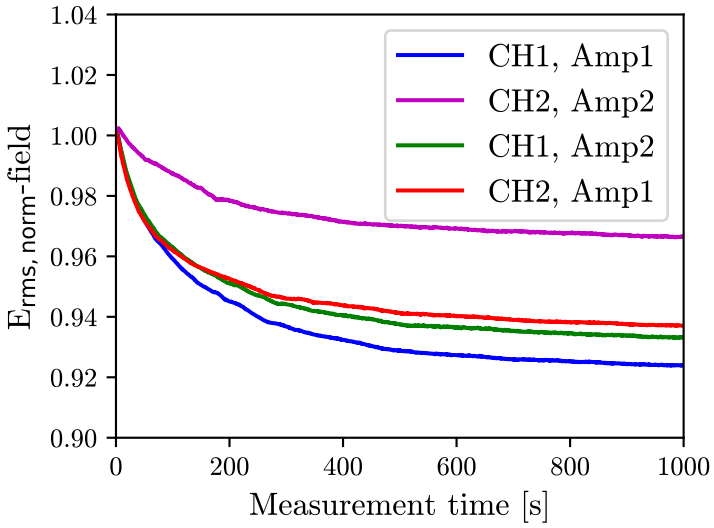

Figure 4.3: The normalized temporal E_{rms}-field decrease during 1000 s measurement time for each channel combined with both amplifiers.

Linearity

To investigate the linearity of the system for different input power levels, both channels were connected and the E_{rms}-field probe was moved in the x-direction between [20/45/325] and [400/45/325]. This line measurement was performed with a phase setting of 0°. The amplitude was set to eight different values (-18, -15, -12, -10, -9, -8, -7 and -5 dBm). For each input power value, one line was measured and the results are presented in Fig. 4.4. Fig. 4.4a) shows, that the E_{rms}-field is higher at higher input powers, as expected. After normalizing the values to their maximum at the start position, the linearity of the E_{rms}-field distribution is visible in Fig. 4.4b). There is a good agreement between the normalized lines and the relative deviation of each line from the reference line at -12 dBm is within $+6.04$ % and -2.36 % in Fig. 4.4c). The largest deviation is measured in the center of the phantom and the deviation increases with the input power. The amplification factor between the input powers does not result in a corresponding increase in the E_{rms}-field value for the higher input power values, as presented in Fig. 4.4d). An increase of 6 dBm should result in a doubling of the E_{rms}-field value and the lines should be straight. Therefore, the input power for this system should not be higher than -7 dBm, depending on the purpose of the measurement. For -5 dBm the relative deviation exceeds 5 % and performance decreases in terms of the linear energy transfer. A reference amplitude of -12 dBm is chosen to provide a sufficient SNR while limiting the global SAR to a small value to avoid a conductivity shift due to TSM heating and thus a changing E_{rms}-field distribution. An amplitude of -12 dBm results in an

average E_{rms}-field of about 100 V/m. According to equation 3.2.1, this value results in a background ΔT of about 1 °C per 900 s of measurement time.

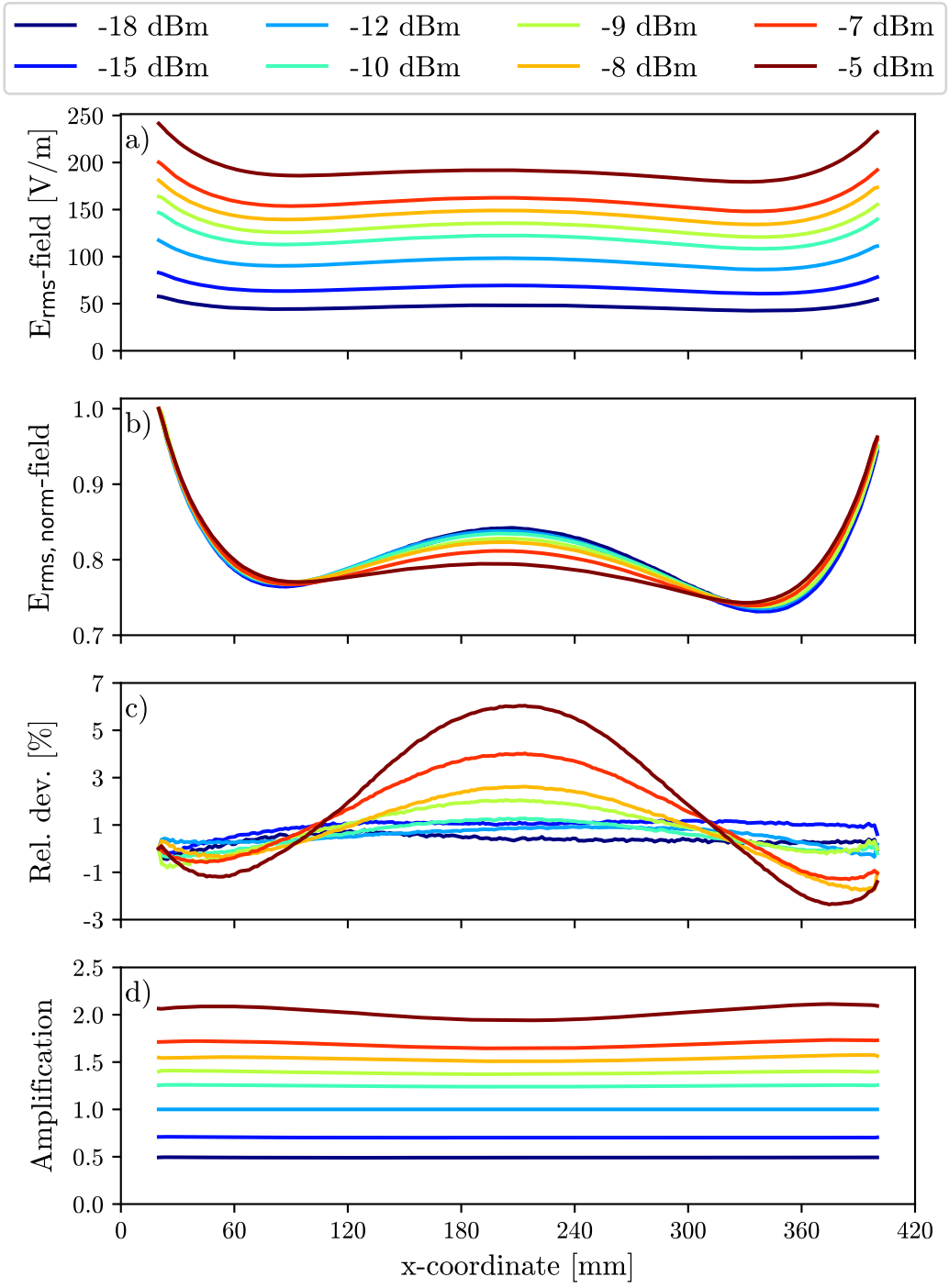

Figure 4.4: The E_{rms}-field distribution in a), the normalized E_{rms}-field in b), the relative deviation to −12 dBm in c) and the amplification to −12 dBm in d) for different input power levels between −18 dBm and −5 dBm along the central line in x-direction.

4.3.2 E-field distribution and repeatability

As a next step, the E_{rms}-field distribution and repeatability is investigated. The E_{rms}-field distribution was measured several times. First, the setup for the linearity measurement was used to identify phase settings between the channels, that result in a suitable E-field distribution for different implant shapes and sizes. The phase of channel 1 was changed in increments of 10 ° from 0 ° to 350°. The amplitude was set to -12 dBm. The results of only every third measurement are displayed in Fig. 4.5 for clarity.

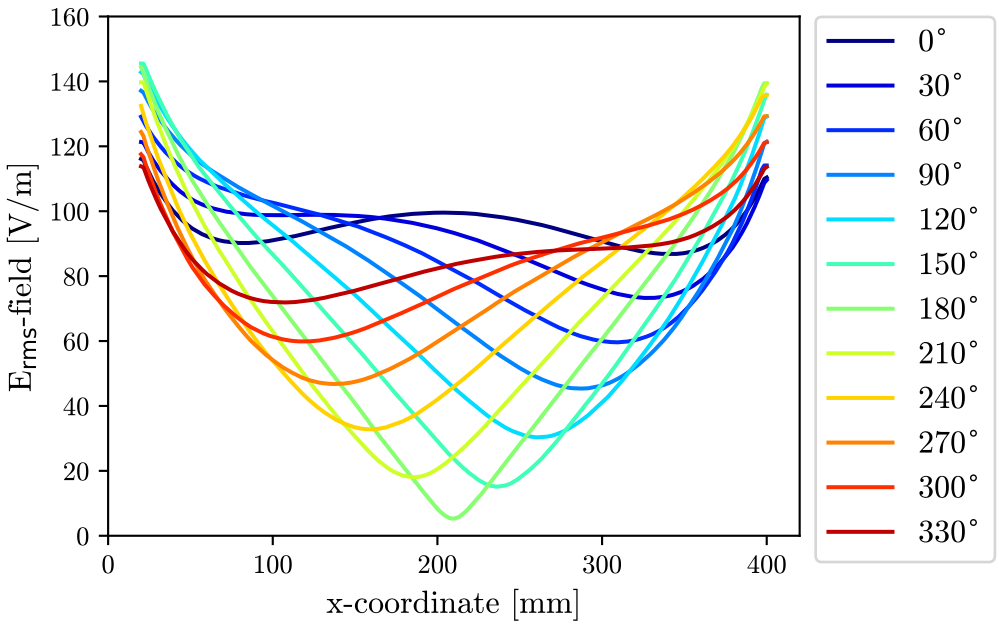

Figure 4.5: The E_{rms}-field distribution for different phase differences every 30° between the channels along the central line at $z = 325\,\mathrm{mm}$ in x-direction.

The E_{rms}-field distribution varies for the different phase settings between the channels. The line measured at 0° and 180° degrees are the lines with the highest and lowest E_{rms}-field at the phantom center at $x = 210\,\mathrm{mm}$. At 0° phase difference between the channels, the E_{rms}-field has the smallest gradient in x-direction and is the most homogeneous. If the distribution is also homogeneous in the y- and z-directions, it is suitable for passive implants with larger 3D extensions, such as orthopedic joints. At 180° phase difference between the channels, the gradient in x-direction is the steepest and the E_{rms}-field value at the start and end position of the line is the highest. Depending on the E_{rms}-field distribution in the z-direction, this phase relation may be suitable for elongated passive implants with a small expansion in the x-direction, such as stents.
Overall, the E_{rms}-field distribution varies significantly with different phase settings, which can be used to expose the passive implant to an ideal tangential E-field, depending on the shape of the implant, or for the testing method of active implants. Both cases are discussed in chapter 5 and 6.

4.3.2.1 E-field mapping

With the available equipment it is possible to measure the E_{rms}-field inside the phantom with the Easy 4/6 probe and the phase and partially the amplitude of the relevant field components with the TDS probe. Due to the calibration of the TDS probe, which is only valid in air, there is no linear probe behavior of the TDS for the amplitude measurement in saline solution.

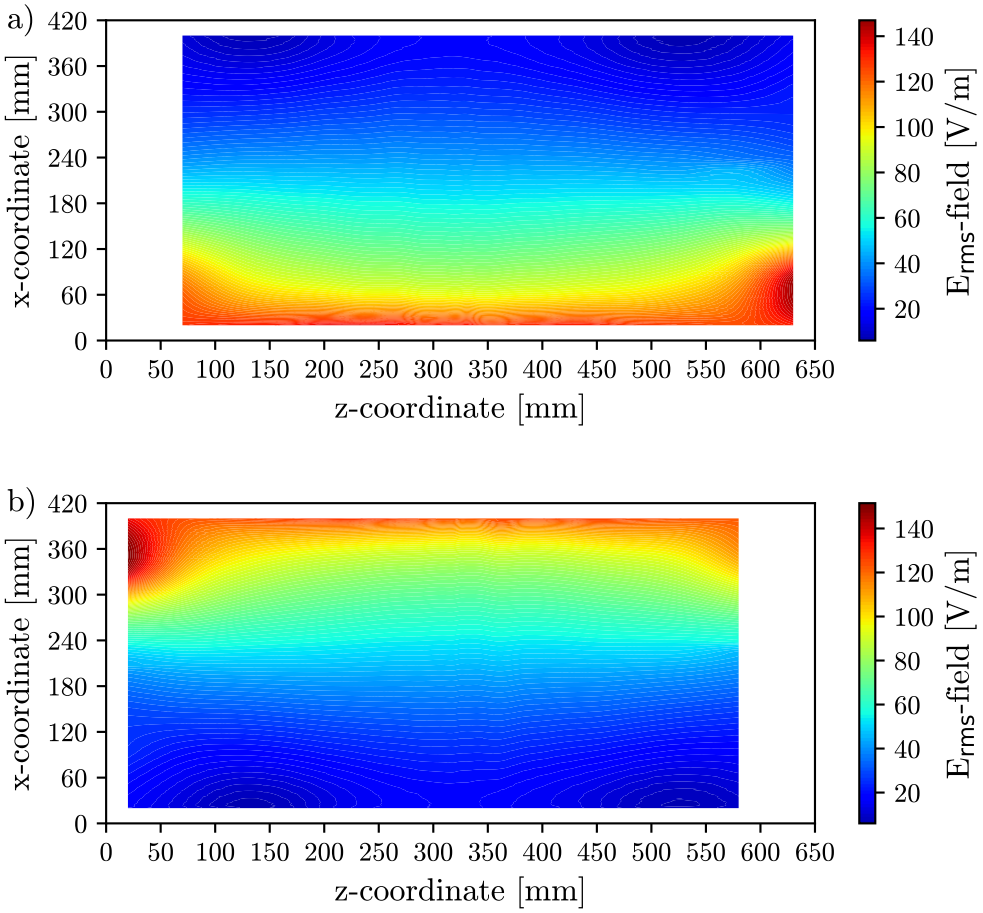

Figure 4.6: The E_{rms}-field distribution for a) channel 1 and b) channel 2, as only one channel is active at a time for the isoplane at $y = 45\,\text{mm}$.

The E_{rms}-field measurements are performed for each single channel and for the channel combinations with 0° and 180° phase difference between the channels. The probes are fixed to the movement system and placed orthogonal at the start position. The probe is moved on a grid, programmed for the movement system. Several measurements are performed, with different directions of movement, depending on the desired plane, with a step size of 1 mm to 5 mm between a measurement value during one line measurement. The number of lines also depends on the measurement plane. The measurement data is linearly interpolated between the lines.
The first measurement is performed separately for each channel. The Easy 4/6 probe measures the E_{rms}-field in the x-direction for 23 lines. The measurement is done for the isoplane, i.e. the xz-plane at $y = 45$. The results for both channels are presented

in Fig. 4.6.
Both channels show a similar behavior, with a steep gradient in the x-direction and a small gradient in the z-direction.
Depending on the phase relation between the channels the combined field interferes constructively or destructively.

For the combined measurement of both channels, the main movement direction was in the z-direction and 39 lines were measured in the isoplane with 10 mm distance between them. The start position was [20/45/20] and the end position was [400/45/630]. The results for the isoplane are presented in Fig. 4.7.

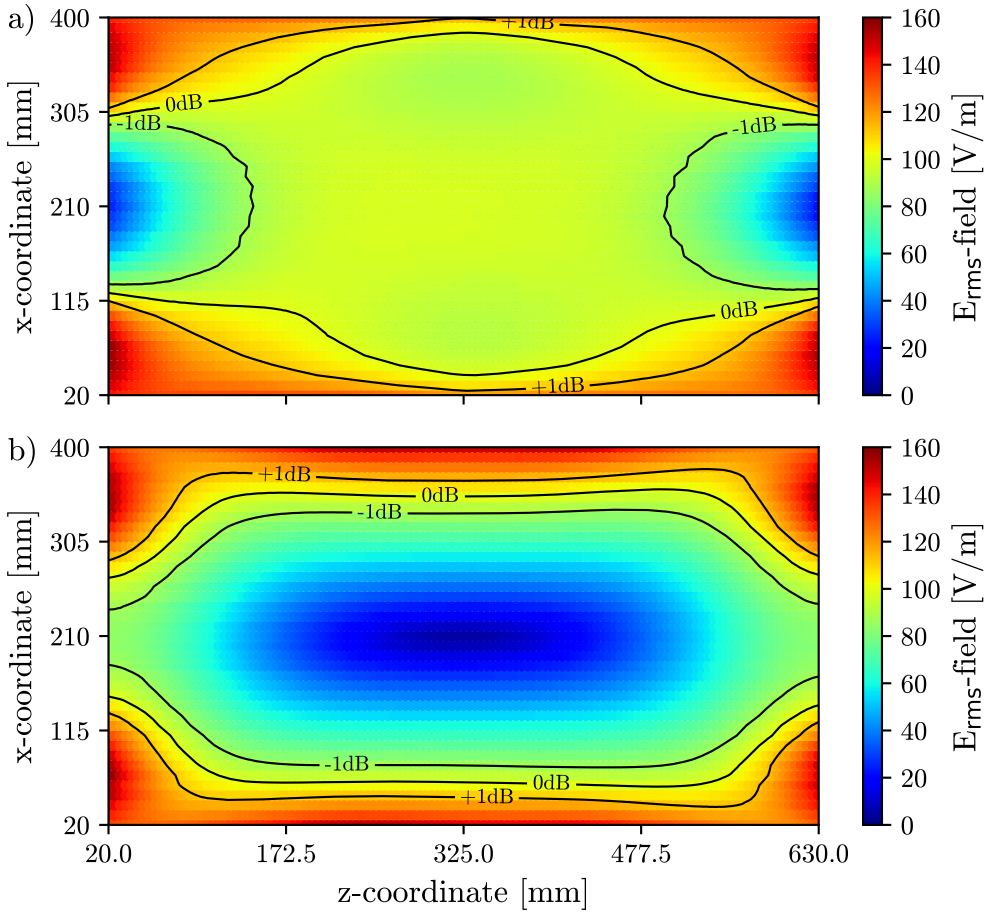

Figure 4.7: The E_{rms}-field distribution for a) 0° and b) 180° phase difference between the channels for the isoplane at $y = 45$ mm including the isolines for −1 dBm, 0 dBm and +1 dBm, modified from Ref. [9].

The E-field distributions of the isoplane indicate, that the phase setting of 0° leads to a large central elliptical volume with a homogeneous E_{rms}-field with the size of approximately 400x300 mm. For the phase difference of 180°, the field along the z-axis is at a stable value for the edges in the x-direction over almost the entire length, suitable for elongated objects with an x-dimension of less than 10 mm.
For the orthopedic joints, not only a two-dimensional homogeneous E_{rms}-field is required, but also a three-dimensional one. Therefore, six additional planes were

measured for the phase difference of 0°, three xy-planes and three yz-planes. The E_{rms}-field is presented in Fig. 4.8.

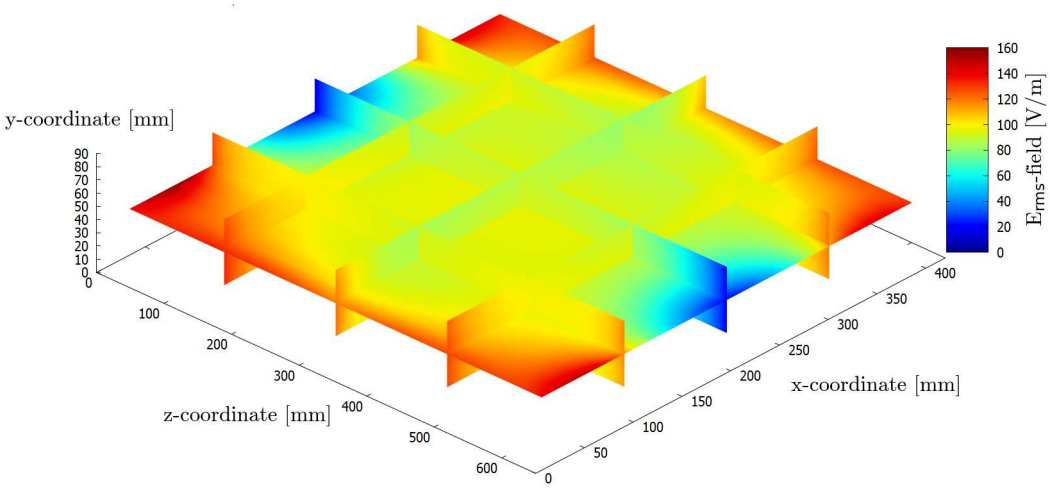

Figure 4.8: The E_{rms}-field distribution for 0° phase difference inside the phantom for seven measurement planes.

The additional planes demonstrate, that the E_{rms}-field is also stable in the y-direction. Additionally, the xz-planes at $y = 20\,\mathrm{mm}$ and $y = 70\,\mathrm{mm}$ were measured. The E_{rms}-field between these two planes and the isoplane is less than 5 V/m. The homogeneous volume, where the E_{rms}-field is within $\pm 1\,\mathrm{dB}$, is 400x300x50 mm. Within this volume, the E_{rms}-field distribution for 0° phase difference is comparable to a plane wave setup, where the E_{rms}-field is unidirectional with the same amplitude and phase over the exposed volume.
For implants exceeding 50 mm in the y-dimension the height of the TSM may be increased. A verification measurement is recommended for the specific height to ensure the field homogeneity for the individual implant. The implants and TOs used in this work are within the dimensions of the homogeneous volume for a TSM height of 90 mm.

To evaluate the repeatability and stability of the E_{rms}-field distribution, two measurements with the same measuring grid are compared. They were performed on different days and the setup was rebuilt at 0° phase difference for $-12\,\mathrm{dBm}$ input power. The measured E_{rms}-field for each point on the measuring grid is shown in Fig. 4.9. There is a strong correlation between the measurements with a coefficient of determination $R^2 = 0.993$ and a regression with $y = 1x$. The mean value and its standard deviation of the difference of day 2 compared to day 1 is $-0.73 \pm 2.61\,\%$. This standard deviation is confirmed for the measurements with different measurement grids.

In a second series of measurements, the phase and amplitude of the z-component of the E_{rms}-field were measured with the TDS probe, since the z-component should be the dominant E_{rms}-field component. The TDS probe was fixed to the movement system and placed orthogonal to the xz-plane inside the phantom. As mentioned

before, the TDS probe is not calibrated for the TSM. Therefore, the results of the TDS measurement are not the absolute values, but the relative values and are only valid for the area, where the amplitude was not too high.

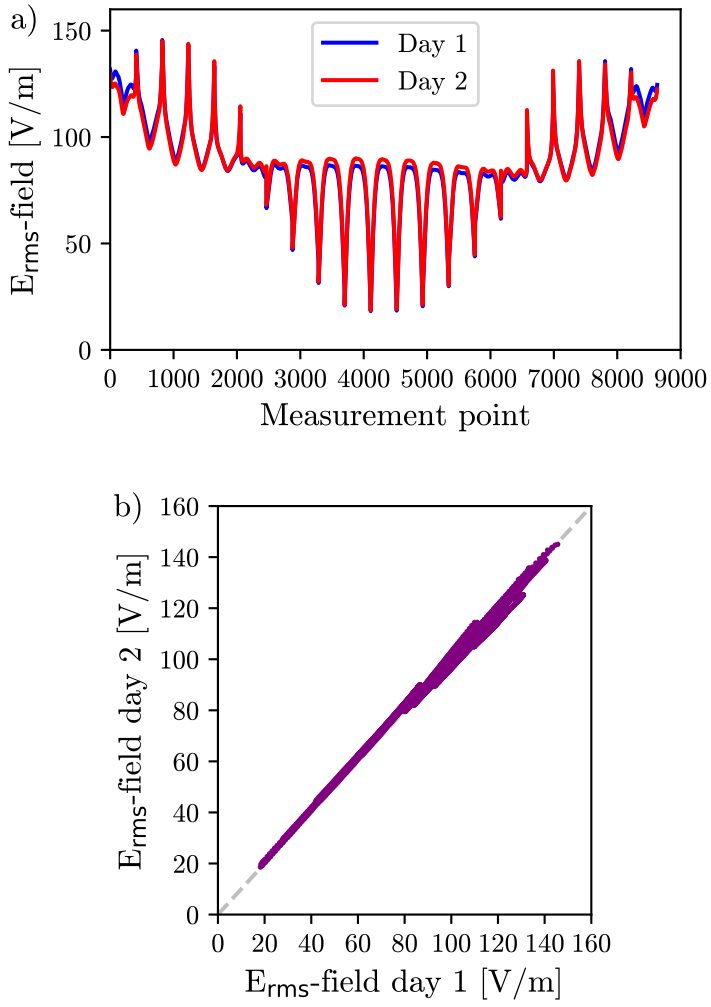

Figure 4.9: Measurement results of the E_{rms}-field distribution of the isoplane measured along the z-direction for 21 different x-distances at two different days in a) and the correlation between the E_{rms}-field distribution per day in b).

As a first measurement, the amplitude and phase of the z-component of both single channels were measured and compared for seven lines with a length of 610 mm measured in z-direction ($x = 20, 140, 200, 210, 220, 280, 400$). Since the antennas are attached on different sides, the line at x=20, when channel 1 is active, is compared with the line at x=400, when channel 2 is active, to investigate if their behavior is symmetrical. The amplitude and phase for both channels are displayed in Fig. 4.10. The amplitude and phase distributions for the seven measurement lines are similar for both channels. As intended, the channels operate symmetrically. The relative mean value and its standard deviation of the difference of CH2 compared to CH1 is 0.08 ± 4.76 % in amplitude and 1.64 ± 3.29 % in phase. The higher standard deviation

of up to ±19.86 % occurs in the first and last 30 mm of the lines, where the absolute values are small, and at the phase jumps measured for line 7.

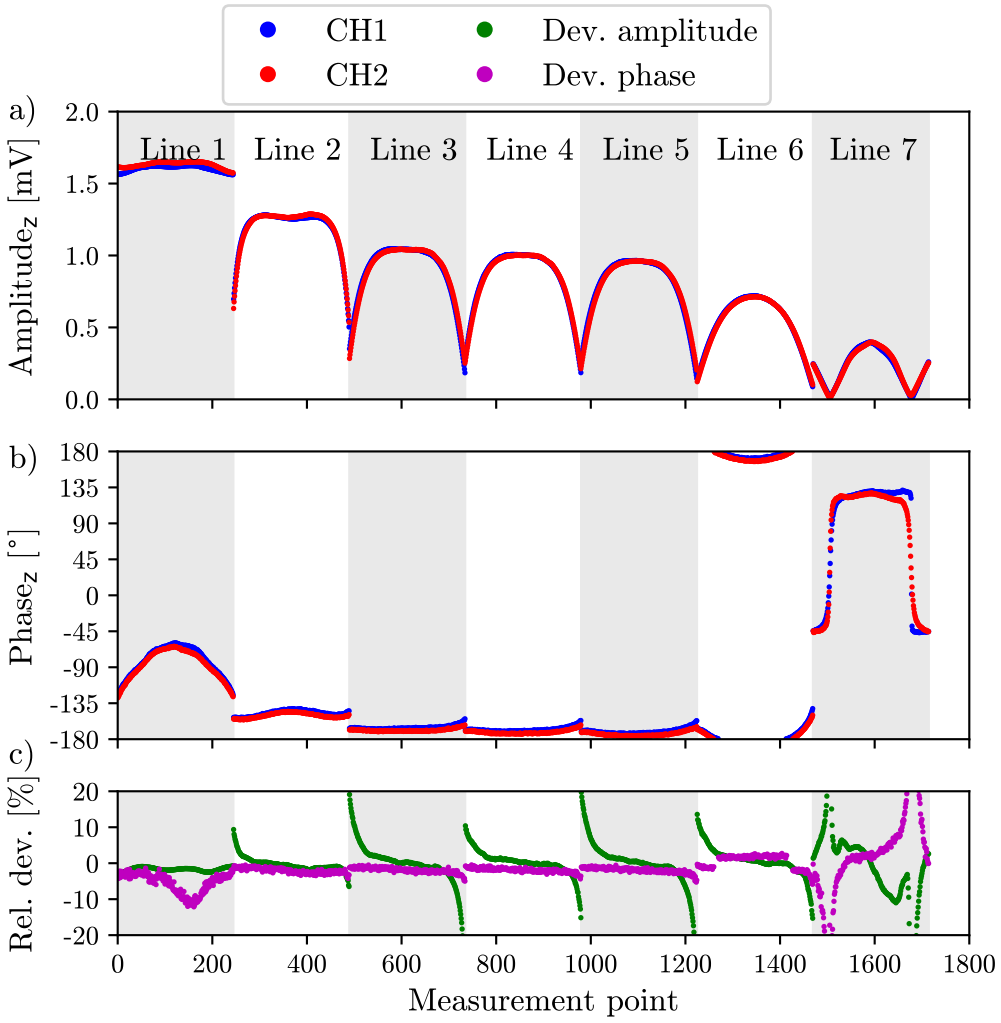

Figure 4.10: The tangential E_{rms}-field a) amplitude$_z$ and b) phase$_z$ in z-direction for both channels individually, as only one is active at a time and the relative deviation between the channels in c).

For the same seven lines, the distributions for the channel combinations at 0° and 180° phase difference are measured on two different days. The results for 0° phase difference are displayed in Fig. 4.11. The amplitude and phase are in good agreement for both measurement days. For day 2 compared to day 1, the relative mean value and its standard deviation of the difference of the amplitude are -0.62 ± 1.11 %. For the phase, the mean value and its standard deviation are $0.00 \pm 0.82°$. The deviation of the amplitude increases for small absolute values at the beginning and end of the lines. In addition, the distribution of the E_{rms}-field in the z-direction is similar to the E_{rms}-field, which indicates that the polarization purity is high. Not only the amplitude is homogeneous over a large area, but also the phase is within ±20° for the lines between $x = 140$ and $x = 280$.

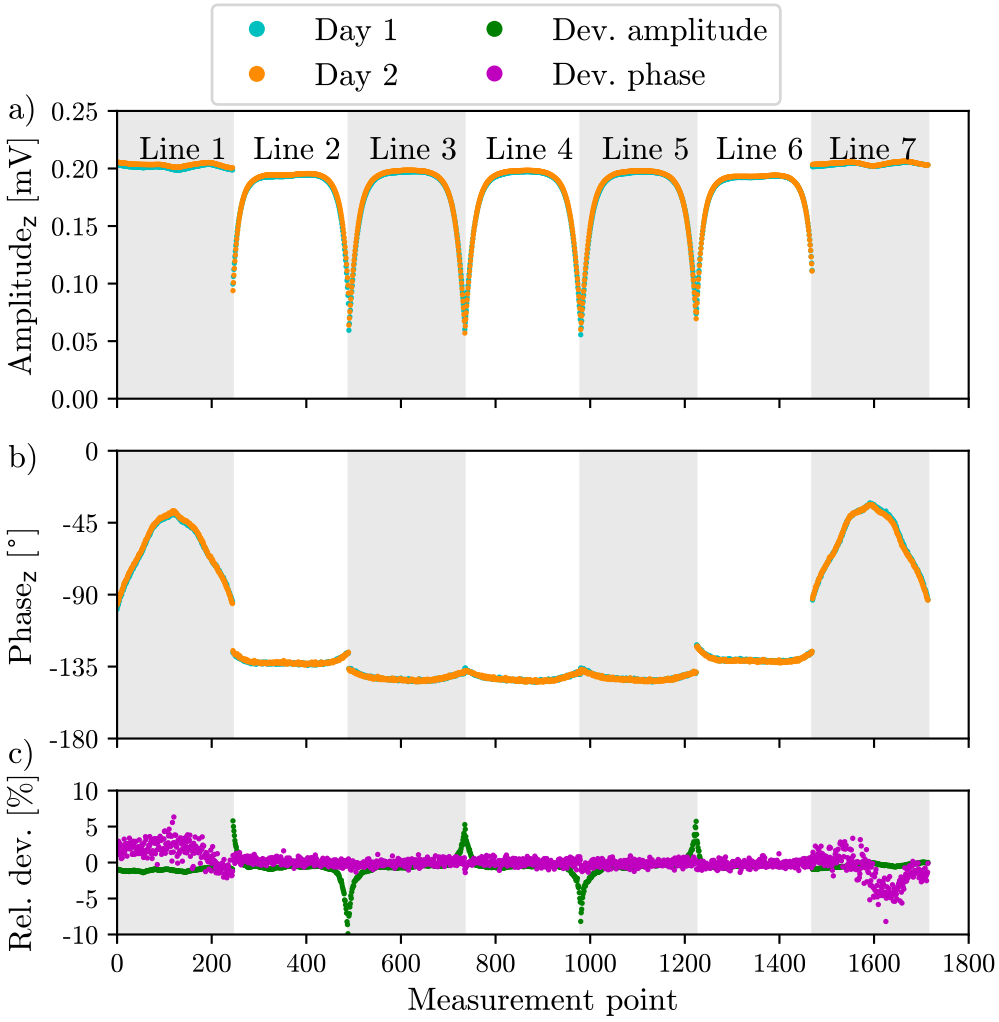

Figure 4.11: The tangential E_{rms}-field a) amplitude$_z$ and b) phase$_z$ in z-direction for 0° phase difference between the channels and the relative deviation between the measurement days in c).

The E_{rms}-field distribution for a phase difference of 180° are presented in Fig. 4.12. The amplitude and phase for 180° are in good agreement. However, the standard deviation for 180° is larger than for 0° phase difference and differs substantially between the lines. The relative standard deviation for the amplitude increases, because of the small absolute values for the three lines in the phantom center. For the phase distribution, the standard deviation increases for the same three lines, because a phase shift occurs in the center of the phantom, making the measurement very sensitive to the measurement probe position. Excluding line 3, line 4 and line 5, the mean value of the relative difference between the measurements and its standard deviation is $-0.16 \pm 2.67\,\%$ for the amplitude and $0.22 \pm 1.52°$ for the phase, with line 2 increasing the deviation for phase and amplitude at the start and end of the line. The stronger x-gradient of the distribution for 180° makes the deviation even more sensitive to the placement of the E_{rms}-field probe and its orientation. Therefore, it is recommended to place TOs only between $x = 20\,\mathrm{mm}$ and $x = 100\,\mathrm{mm}$ or on the opposite side.

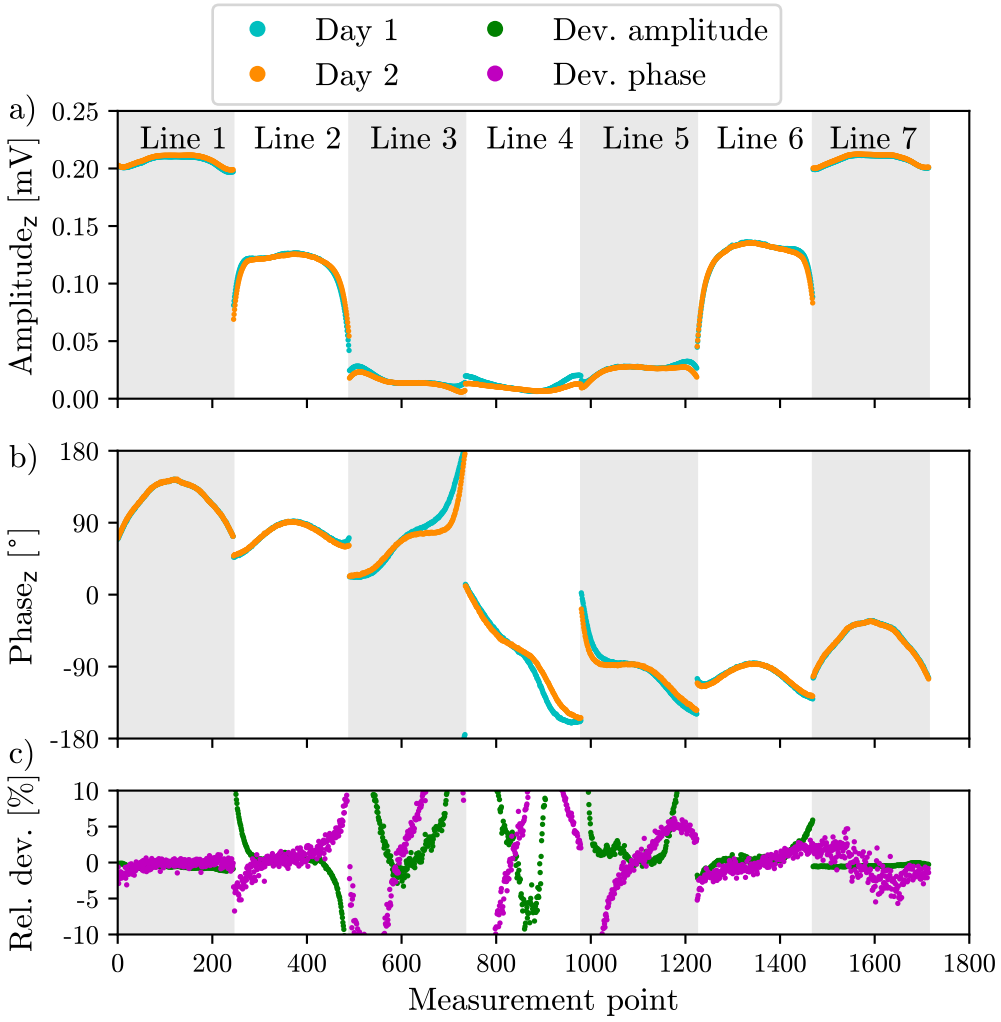

Figure 4.12: The tangential E_{rms}-field a) amplitude$_z$ and b) phase$_z$ in z-direction for 180° phase difference between the channels and the relative deviation between the measurement days in c).

4.3.2.2 Numerical prediction from E-field simulation

As mentioned before, the numerical predictions for the E_{rms}-field distribution were carried out by ING Gao. They provided the real and imaginary part for each component for each channel with 1 mm resolution for the isoplane. The input power for the numerical prediction corresponds to the input power of −12 dBm setting at the frequency generation, which allows the absolute comparison of the values.
To compare the numerical predictions with the measurements, the E_{rms}-field values are calculated for each single channel and the combination for 0° and 180° phase difference. Additionally, the amplitudes and phases for the x-, y-, and z-components are extracted. Since the computer simulation is performed individually for each channel, no possible coupling between them is considered. Therefore, the results of the numerical predictions must be compared with the measurement results of the individual channels and their combination in order to evaluate the coupling during

the measurement and thus whether the numerical predictions can be used for combined predictions. The results are given for the isoplane at 20 mm distance to the wall, since no measurements take place for a smaller distance from the wall. The E-field distribution for 180° for all three components including the total E-field is presented in Fig. 4.13. In addition, the E-field distribution for the z-component for both single channels and the total field of the channel combinations at 0° are presented in Fig. 4.14.

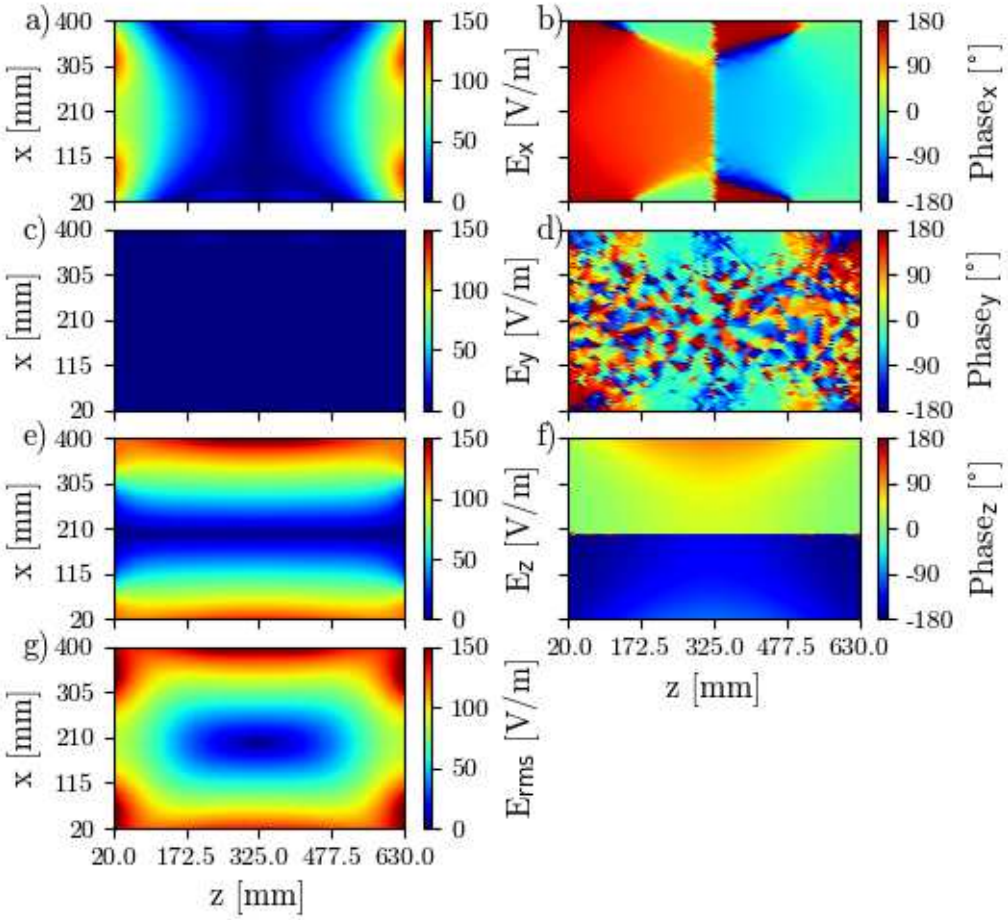

Figure 4.13: The numerical predicted total E_{rms}-field distribution and the tangential E_{rms}-field distribution for all three components in amplitude in a) E_x, b) E_y, c) E_z and phase in b) Phase$_x$, d) Phase$_y$, f) Phase$_z$ and in g) the total E-field for 180° phase difference between the channels.

The numerical predictions show, that for all four cases, the amplitude of the z-component is the main component contributing to the total E_{rms}-field. The amplitude of the y-component is negligible, since the amplitude is less than 10 V/m over the entire plane, even when both channels are active, as displayed in Fig. 4.13. The amplitude of the x-component contributes mainly at the positions of the end plates at the antennas, as expected and is less than 10 V/m in the area around the phantom center. The x- and y-components for CH1, CH2 and 0° are displayed in section A.1.
The behavior of each channel is similar and symmetrical in amplitude and phase.

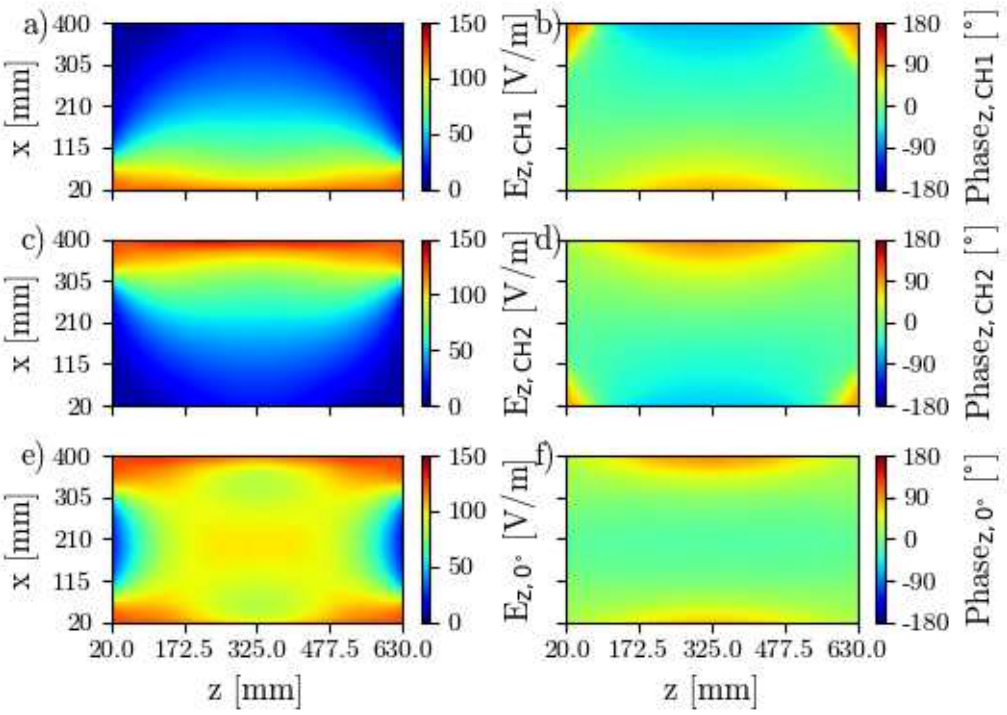

Figure 4.14: The numerical predicted tangential E_z-field for CH1 in a) amplitude $E_{z,\mathrm{CH1}}$ and b) $\mathrm{Phase}_{x,\mathrm{CH1}}$, CH2 in c) amplitude $E_{z,\mathrm{CH2}}$, and d) $\mathrm{Phase}_{x,\mathrm{CH2}}$ and 0° phase difference in e) amplitude $E_{z,0^\circ}$ and f) $\mathrm{Phase}_{x,0^\circ}$, partially reused from Ref. [14].

The phase distribution of the components varies considerably. However, the phase distribution of the main component in the z-direction is smooth over the entire plane for the individual channels and 0° phase difference. In addition, the phase distribution is homogeneous and within ±20° over a large central area. The phase for 180° of the z-component is also smooth, but has a phase shift at the central line in z-direction. Furthermore, the distribution for 180° phase difference has a strong gradient in the x-direction. Therefore, this phase setting is sensitive to imprecise placement of the TO in the measurement setup and the movement system, which is already visible in the repeatability measurement in Fig. 4.12. The amplitude of the z-component of the distribution at 180° show, that the E_{rms}-field along the z-axis is homogeneous over almost the entire z-line. This distribution may be suitable for elongated passive implants with small dimensions in the x- and the y-directions. The most homogeneous line in z-direction is at $x = 60\,\mathrm{mm}$ distance from the phantom wall.
The distribution for 0° phase difference displays a central homogeneous E-field in amplitude and phase, as desired, for a large part of the plane. It is therefore suitable for all types of 3D extended passive implants.

4.3.2.3 Comparison of the measured E-field to the numerical predictions

To determine how well the measured results agree with the theoretical assumptions of the numerical predictions, the absolute values of the E_{rms}-field of the isoplane for

0° and 180° phase difference are used, since they were measured with the Easy 4/6 probe. The phase and partially the amplitude of the z-component are compared relatively, measured with the TDS probe. The tangential E-field in the z-direction is compared for each channel individually, while the lines with the highest and lowest amplitude are excluded from the amplitude comparison due to the non-linearity of the TDS probe. The amplitude of the measurement is scaled to the range of the predicted E-field. The scaled amplitude and phase for both channel 1 and channel 2 are displayed for each measurement point and compared to the predictions in Fig. 4.15.

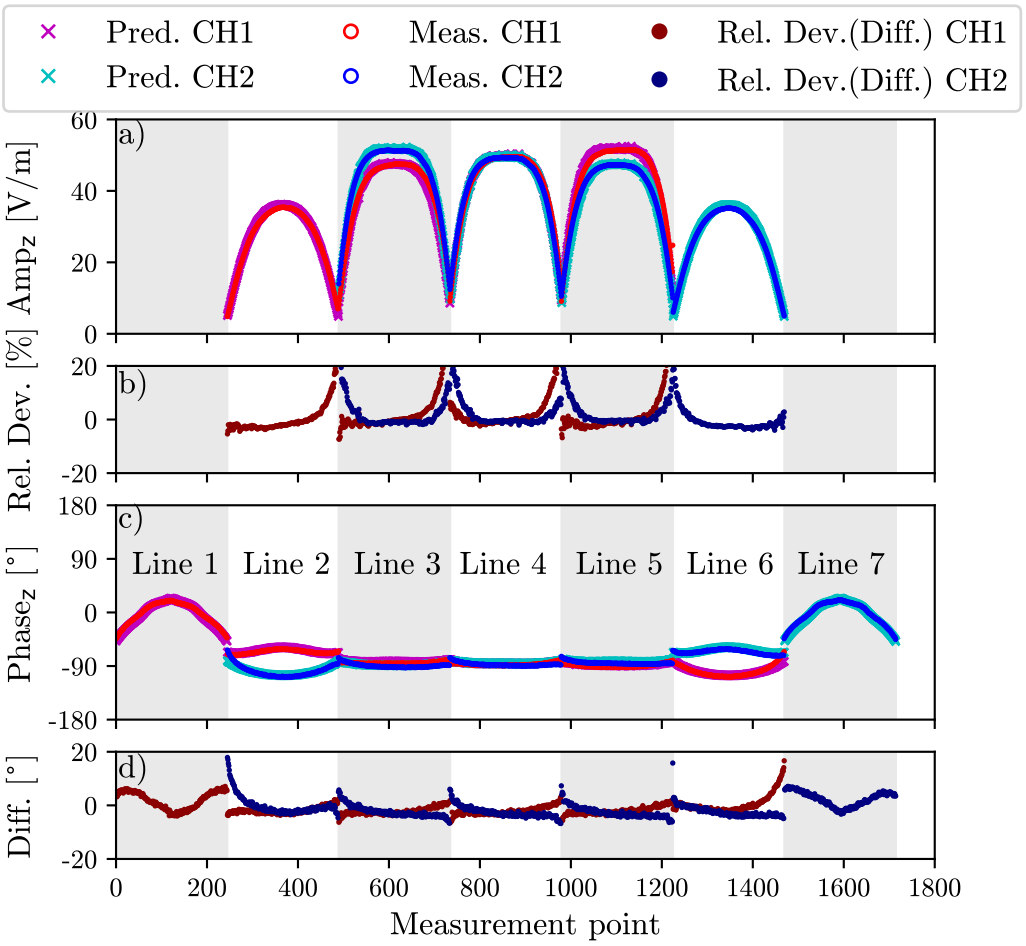

Figure 4.15: The comparison between the E_z-field distribution of the single channels from the numerical prediction and the measurement in a) amplitude$_z$, b) the relative deviation between prediction and measurement, c) phase$_z$ and d) the difference between prediction and measurement for each channel of the z-component.

There is good agreement between the measured data and the numerical predictions for both single channels for the z-component in amplitude and phase. The described symmetry between the channels also applies to the measured results. The difference between the predicted and measured phase per channel is in good agreement and increases at the both ends of the line to 16.64° for CH1 and 22.79° for CH2. Excluding the outer 30 mm of the lines reduces the difference to 5.71° and 6.01°.

The relative deviation of the amplitude of the measured E-field compared to the predicted E-field increases at the start and at the end of all lines, where the absolute values are small, increase to a maximum relative deviation of 48.97 % for CH1 and to 35.72 % for CH2. Excluding the first and last 30 mm reduces the maximum deviation to 10.24 % and 5.59 %, respectively. In addition, the relative deviation of the amplitude increases for the smaller values, due to the limited linearity of the TDS probe and the lack of calibration for the TSM. However, due to the good agreement for the main part of the lines, it is assumed that the tangential components of the E_{rms}-field are as expected from the numerical predictions.
The results for the difference between the numerical prediction and the measurement of the total E_{rms}-field for the whole isoplane for 0° and 180° phase difference are shown in Fig. 4.16, as the absolute error ΔE for both phase settings.

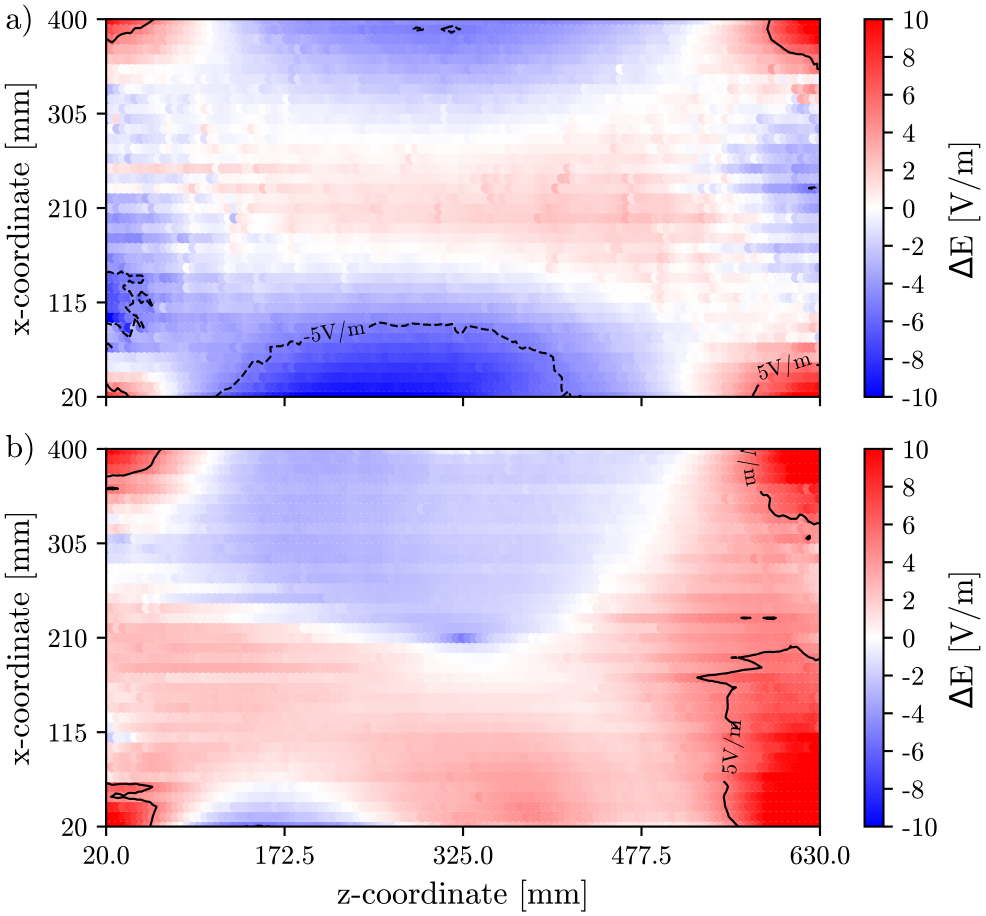

Figure 4.16: The absolute difference ΔE between the numerical prediction and the measurement values for the E_{rms}-field distribution for a) 0° and b) 180° phase difference between the channels.

The measurements with the Easy 4/6 E_{rms}-field probe are in good agreement even when comparing the absolute values. The maximum absolute deviation between measurement and numerical prediction is 18.5 V/m for 180° and 14.5 V/m for 0°, respectively. The distribution of the absolute difference illustrates, that it increases at the edges of the isoplane at the position of the end plates. For the intended

measurement volume for 0° phase difference, expanding 400x300 mm, the absolute error is within ±5 V/m. For 180° phase difference, the absolute error is within ±5 V/m for almost the entire plane except the edges.
The relative difference for both phase settings for the isoplane excluding the edges is displayed in Fig. 4.17.

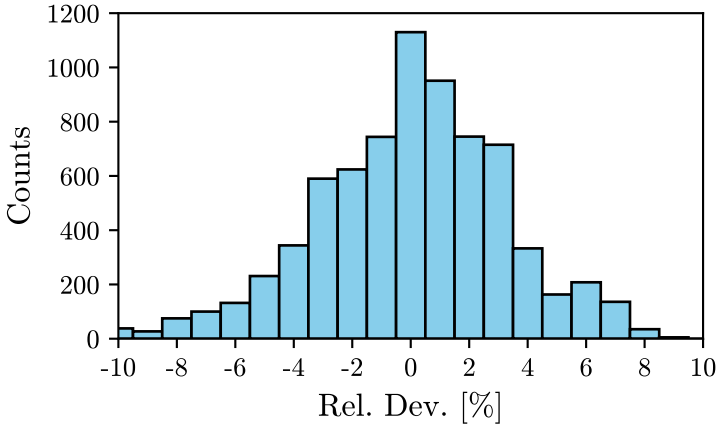

Figure 4.17: The relative deviation between the numerical prediction and the measurement values for the isoplane for 0° and 180° phase difference between the channels.

The mean value and its standard deviation are 0.02 ± 3.31 %.
Overall, the numerical prediction and the measurement of the E_{rms}-field distribution are similar for each single channel and their combination at 0° and 180° phase difference. The amplitude and phase as well as the E_{rms}-field show symmetrical behavior and different tangential E_{rms}-field distributions are applied and validated. The deviation for the measurement with combined channels is not increased compared to the single channel measurement. Therefore, the coupling between the channels is negligible, at least for the input power of −12 dBm and the phase differences of 0° and 180°. Based on the results of the linearity measurements in section 4.3.1, the relative deviation between the numerical predictions and the measurement results at different input power levels should be evaluated individually, especially in the context of the testing of active implants.

4.3.3 Annex I validation

As an additional validation step, the procedure for RF exposure systems according to the ISO/TS 10974 Annex I is performed [4]. This procedure uses the SAIMD-2 as a reference test object, which is placed in the RF exposure system inside the gelled TSM [4]. The ISO/TS provides the expected ΔT scaled to the square of the incident E-field for various radial distances from the TO. These values are the target values for the validation measurement of a particular RF exposure system.
For the validation measurement for the LES, the SAIMD-2 was placed as the TO in the center of the phantom, aligned with the z-axis. The phase difference between the channels was set to 0° and the start amplitude was set to -8 dBm to provide

a sufficient SNR for six minutes of measurement time. The measurement setup is shown in Fig. 4.18. The Easy 4/6 E_{rms}-field probe was placed together with one temperature probe at a reference position at [260/45/325]. Two additional temperature probes P1 and P2 were placed at one end of the TO and P3 was placed inside the hole on the same side. These temperature probes were fixed for all measurement runs. One temperature probe P4 was fixed to the movement system and placed at the other end of the TO. This temperature probe was moved after each run in the direction of the red arrow in Fig. 4.18, to measure the ΔT at different radial distances. The setup of the first run at the distance of 0.5 mm is displayed in Fig. 4.18. All temperature probes were TS2P probes. A total of seven runs of six minutes each were performed. During the measurement, the amplitude was readjusted so that the E_{rms}-field value at the reference location was 150V/m.

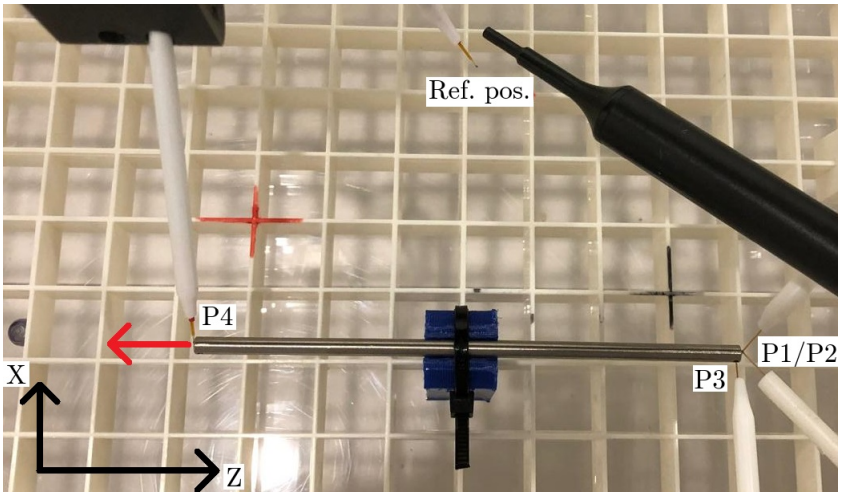

Figure 4.18: The measurement setup of the SAIMD-2 including the locations of temperature probes P1-P3 and the moving probe P4 along the red arrow and the reference position of the E-field and temperature probe inside the phantom.

To scale the E_{rms}-field value at the reference location to the measurement location of P4, an E_{rms}-field measurement was performed at this location without the TO in place. The incident field at the measurement location of P4 is 162.5 V/m and the absolute ΔT ranges from 17.3 °C at the closest proximity to 8.6 °C at 5 mm radial distance. The ΔT within the six minute measurement time is divided by the squared E_{rms}-field at the TO position and compared with the target values from Annex I in Ref. [4]. For the fixed temperature probes, seven values are available to determine the mean ΔT and the standard deviation at their location. The result for P3 at the hole of the TO is $0.629 \pm 0.008\,\mathrm{mK/(V/m)^2}$ and the target value from Annex I is $0.621\,\mathrm{mK/(V/m)^2}$, which is within the measurement uncertainty. The results for the temperature probes P1 and P2 fixed at one end of the TO are $0.652 \pm 0.012\,\mathrm{mK/(V/m)^2}$ at 0.5 mm distance and the target value from Annex I is $0.660\,\mathrm{mK/(V/m)^2}$. The standard deviation of the ΔT for all three fixed temperature probes is within ±0.2°C. Since only one temperature measurement was taken for P4 at each radial distance, the standard deviation of the temperature probe is estimated to be ±0.2°C. The results for P4 and the target values from Annex I are presented in Fig. 4.19. The data show that the target values for each radial distance are within

the standard deviation of the measured values.
In conclusion, all measured values are in agreement with the target values and therefore the Annex I validation has been successfully completed for the LES.

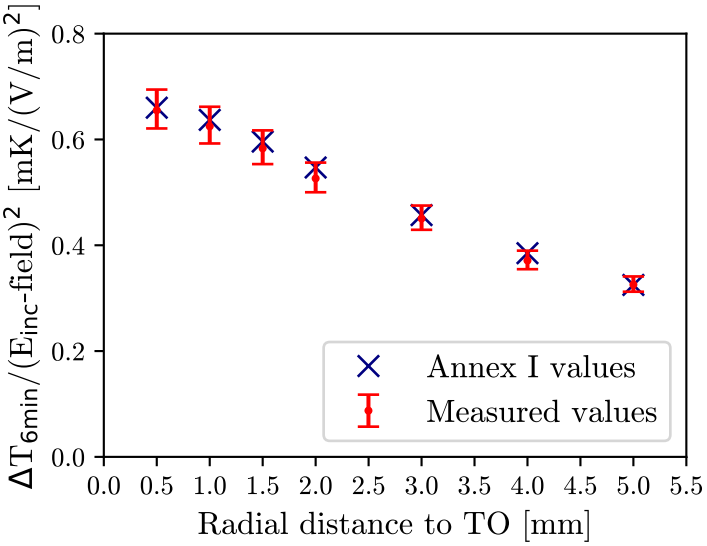

Figure 4.19: The comparison of the measured ΔT scaled to the incident field at different distances to the test object and the target values listed in Annex I for the test object [4], reused from Ref. [14].

4.4 Summary and discussion

The investigation of the behavior of the LES indicates that the system is operating as intended. The S-parameters show a broadband resonance at 64 MHz. There is no frequency shift during measurements or between measurement days as there are no temperature dependent capacitors as in the BC.
A supply line combination is determined to achieve a similar channel behavior during measurements with both channels active. The E_{rms}-field decrease after switching on the system is constant for both channels and can be avoided by readjusting the amplitude at the frequency generator.
During the validation procedure, the linearity of the system is confirmed for input power levels between −18 dBm and −5 dBm. However, for input levels higher than −7 dBm, depending on the measurement task, additional investigations are necessary, because the linearity decreases especially in the central area of the phantom.
Since both channels are independent, it is possible to change the phase difference between them, resulting in various E_{rms}-field distributions. The distributions are measured for both channels individually and for the combination at 0° and 180° phase difference. These phase settings represent the cases with the smallest and largest field gradient in the x-direction. At 0° over a central volume of 400x300x50 mm there is practically no E-field gradient in the x- and z-directions. The main direction of the E_{rms}-field is in the z-direction with high purity. This large homogeneous E_{rms}-field distribution is suitable for 3D orthopedic implants such as knee or shoulder joints. In contrast to this, at 180° phase difference, there is a large field gradient in the

x-direction. However, the tangential E_{rms}-field in z-direction is homogeneous along almost the entire z-component of the phantom. In addition, the E_{rms}-field amplitude is the highest of all phase differences at the standard measurement position at 20 mm distance from the phantom wall, leading to the best SNR without increasing the input power. This E-field distribution is therefore suitable for elongated implants such as stents.
The measurement results for the different E_{rms}-field distributions are in good agreement with the numerical predictions. Both the amplitude and phase distributions are validated. This opens up the possibility of using the numerical predictions in the test procedure to find the ideal location and E-field distribution individually for each passive implant, ensuring the best homogeneity for the tangential E_{rms}-field. It can also be used in the validation procedure of the TF of an active implant.
The novel LES system is more efficient and user-friendly than the conventional setup for testing the influence of the RF-induced heating on implants. With the LES, measurement probes and TOs can be conveniently positioned within the system. The Easy 4/6 E_{rms}-field probe can be precisely aligned orthogonal to the xz-plane, and the integrated movement system allows full access to the entire phantom in a single measurement without additional movement of the TOs as required by the conventional setup. In addition, any components that might interfere with the system can be placed at the maximum possible distance to ensure optimal measurement conditions.
The impact of these advantages of the LES and the possibilities they open up for the testing methods of passive and active implants are analyzed in the chapters 5 and 6.

5 Improvement of the testing method for passive implants

As described in section 2.3, the goal of the measurement for passive implants, is to determine the ΔT per average incident E_{rms}-field for a certain implant. The tangential field component along the implant should be as uniform as possible to produce the highest ΔT for that implant. The more the E_{rms}-field distribution varies along the TO, the greater its influence on the ΔT is. To reduce the patient risk, it is important to determine the maximum possible ΔT per average incident field so that the risk is not underestimated.
This chapter examines the extent to which the user-friendly LES improves the testing of RF-induced heating of passive implants. Therefore, a series of measurements are performed in both systems, the conventional body coil (BC) and the LES. In a first measurement, four different rods are used as elongated TOs with different lengths and small x- and y-dimensions. The influence of the homogeneity of the E_{rms}-field distribution and the influence of the E_{rms}-field decrease over time on the ΔT are investigated. In a second, more comprehensive measurement, 3D extended objects representing the wide range of passive implants are used. The influence of the E_{rms}-field distribution and a possible misplacement of the TO are investigated. The TOs are chrome-vanadium-steel Allen keys as abstract objects. On the one hand, these metallic objects guarantee a high ΔT at the hot spot, and on the other hand, a conflict of interest with a possible implant manufacturer can be avoided. Additionally, an exemplary generic knee implant is used to present a realistic passive implant.

5.1 Influence of the E-field distribution on elongated objects

The first set of measurements includes only elongated objects, which are exposed to the E_{rms}-field generated by the BC and the LES. The ASTM phantom was used for the measurements in both systems. In a first step, the incident E_{rms}-field was measured in the area, where the TOs will be placed in both systems. The dimensions of the measurement plane are 100x610 mm in the isoplane with a 20 mm distance to each wall. As shown in section 4.3.2.2, the optimal measurement position inside the LES for elongated objects is at $x = 60$ mm distance to the wall and a phase difference of 180° between the channels. Inside the BC, the same position was used. The larger distance to the wall compared to the recommended distance of 20 mm, reduces possible reflection effects [59]. The four TOs have different lengths between 100 mm and 300 mm. Six lines were measured along the z-axis with one value every 1 mm and a distance of 20 mm in the x-direction. The interpolated E_{rms}-field distributions for both systems are displayed in Fig. 5.1, including the measurement position and dimensions of the largest TO and the ± 1 dB isolines.
The E_{rms}-field distribution differs considerably in the two systems. In the LES, the

E_{rms}-field is homogeneous over the entire volume of all TOs. In the BC, the E_{rms}-field varies over the volume and the ±1 dB homogeneity limit is not fulfilled for the 300 mm long object.

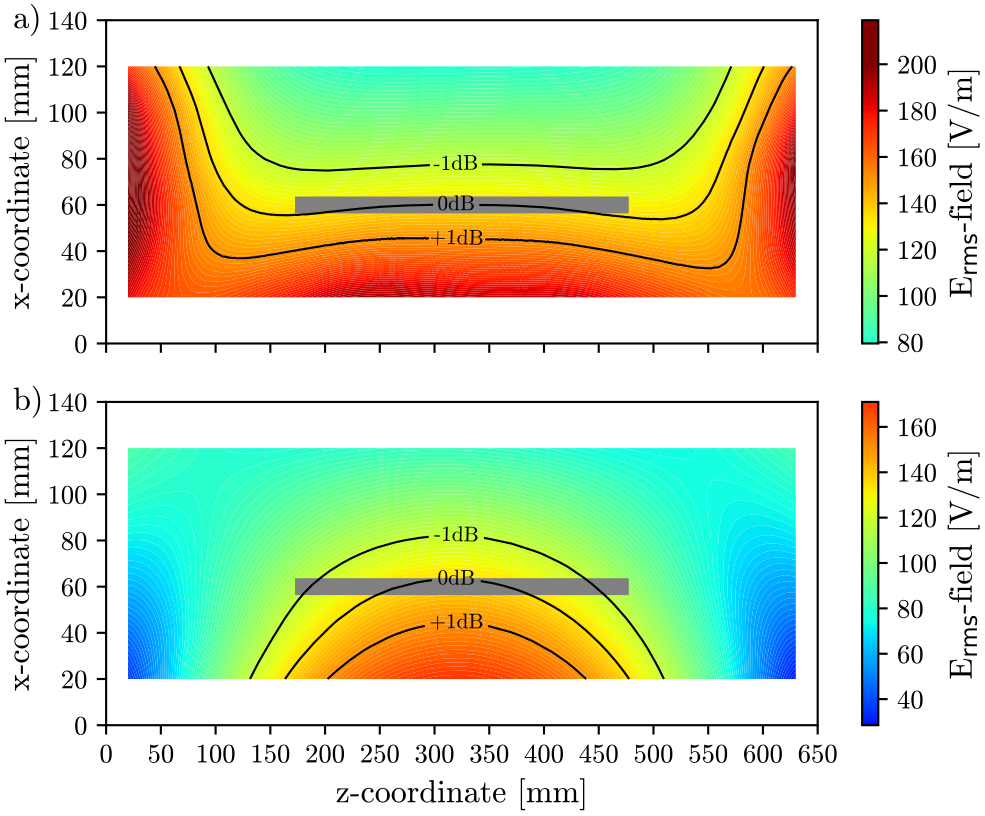

Figure 5.1: The measured E_{rms}-field distributions with the 0 dB and the ±1 dB isolines and the placement of the 300 mm-long rod for the a) LES and b) body coil case. The placement is representative for all four used test objects. The figure is modified from Ref. [10].

The maximum deviation from the mean E_{rms}-field value per object length and system is listed in table 5.1, where Deviation + is defined as the relative deviation of the maximum E-field value from the mean value and Deviation − is the relative deviation of the minimum value from the mean value over the length of the TO.

	LES		BC	
Length [mm]	Deviation +	Deviation -	Deviation +	Deviation -
100	0.25 %	-0.21 %	1.01 %	-2.34 %
200	0.68 %	-1.53 %	3.26 %	-8.02 %
300	1.59 %	-3.05 %	7.08 %	-16.14 %

Table 5.1: The E_{rms}-field variation over the test object length for the different systems including the highest value scaled to the mean value deviation + and the lowest value scaled to the mean deviation -, modified from Ref. [10].

The E_{rms}-field over the TO volume varies substantially between the systems and the object length. For the LES, the maximum deviation from the mean incident E_{rms}-field is $-3.05\,\%$ to $1.59\,\%$ for the 300 mm TO. The homogeneity requirement of $\pm 12.6\,\%$ (± 1 dB) is fulfilled for all objects.
Within the BC, the deviation is larger for all TOs compared to the LES. For the length up to 200 mm the deviation is within $\pm 12.6\,\%$, but for the 300 mm long TO, the deviation is up to $-16.14\,\%$.

In a second measurement, the four TOs are successively placed centrally in the phantom in the z-direction, as presented in Fig. 5.1. The 100 mm long titanium rod (SAIMD-2) and three stainless steel rods ($\varnothing$= 6 mm, length: 100 mm, 200 mm, 300 mm) are used and two fiber optic temperature probes (TS2P) are placed at each end P1/P2 and P3/P4, as shown in Fig. 5.2. To monitor the measurement conditions, the Easy 4/6 E_{rms}-field probe was placed at a reference location on the opposite side of the TO location [325/45/360].

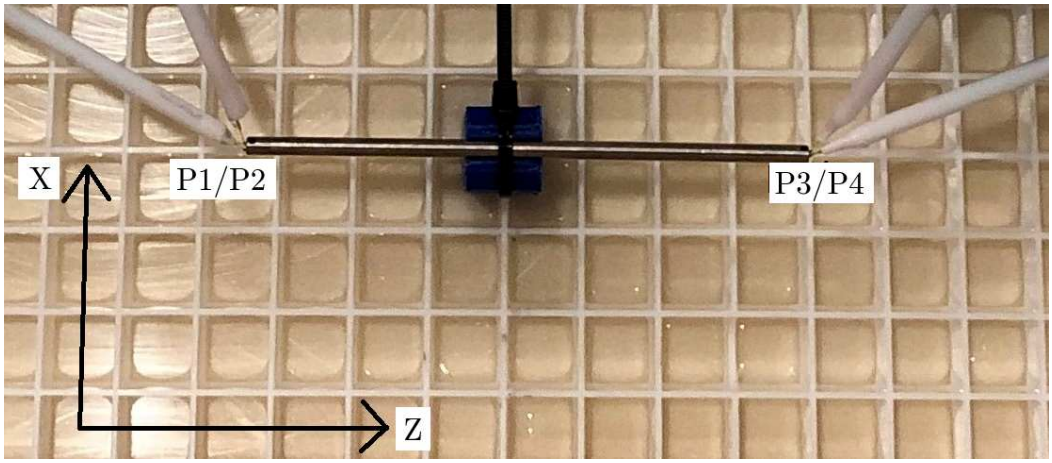

Figure 5.2: The setup of the titanium rod and temperature probe placement P1/P2 and P3/P4 for all four probes. This setup is representative for all objects, modified from Ref. [10].

To investigate the influence of the E_{rms}-field homogeneity, the TOs were placed in the phantom of both systems and the measurement time was six minutes per run. The temperature rise was measured for each TO with and without the object in place. From these two measurements the ΔT is calculated. To compare the results, the ΔT is normalized to a mean incident E_{rms}-field of 150 V/m. During the six minutes measurement time, the amplitude was readjusted at the function generator to a stable E_{rms}-field value at the reference position.
The ΔT of the four temperature probes is averaged and the standard deviation is calculated for each measurement run. The ΔT divided by the square of the incident E_{rms}-field for SAIMD-2 inside the LES is $0.656 \pm 0.009\,\mathrm{mK/(V/m)^2}$, which is consistent with the target value from Annex I in Ref. [4]. The ΔT per TO are listed in table 5.2, recalculated for a mean incident E_{rms}-field of 150 V/m.
The ΔT is higher in the LES for all TOs compared to the BC. The difference in ΔT between the two systems increases with the inhomogeneity of the E_{rms}-field. The ΔT in the BC differs by $4.02\,\%$ from that in the LES for the SAIMD-2, and by $4.36\,\%$ for

the 100 mm rod. For the 200 mm rod, the deviation between the systems increases to 6.40 % and for the 300 mm rod to 11.88 %. Therefore, the measurement setup in the BC is not sufficient and underestimates the potential ΔT for a potential implant. The larger the implant is, the greater and therefore severe the underestimation, which can be potentially dangerous for patients with passive implants.
For the LES, the good E_{rms}-field homogeneity of all TOs and its E_{rms}-field purity in the z-direction fully aligned with the TO represent the worst-case for these objects, resulting in the highest ΔT.

	SAIMD-2	100 mm rod	200 mm rod	300 mm rod
LES	$14.77 \pm 0.21\,^{\circ}\mathrm{C}$	$9.54 \pm 0.21\,^{\circ}\mathrm{C}$	$15.90 \pm 0.31\,^{\circ}\mathrm{C}$	$13.55 \pm 0.29\,^{\circ}\mathrm{C}$
BC	$14.12 \pm 0.18\,^{\circ}\mathrm{C}$	$9.16 \pm 0.25\,^{\circ}\mathrm{C}$	$14.89 \pm 0.18\,^{\circ}\mathrm{C}$	$11.94 \pm 0.27\,^{\circ}\mathrm{C}$

Table 5.2: The mean ΔT recalculated to 150 V/m and its standard deviation between the temperature probes for the four test objects in the LES and the BC.

The SAIMD-2 was used for an additional measurement to investigate the influence of the decrease of the E_{rms}-field over the measurement time on the ΔT, when the amplitude is not readjusted, as displayed in Fig. 4.3. For each system, one measurement with and without amplitude readjustment was performed. The ΔT for 150 V/m are listed in table 5.3.

	Constant E-field	Decreasing E-field
LES	$14.77 \pm 0.21\,^{\circ}\mathrm{C}$	$14.04 \pm 0.25\,^{\circ}\mathrm{C}$
BC	$14.12 \pm 0.18\,^{\circ}\mathrm{C}$	$13.59 \pm 0.22\,^{\circ}\mathrm{C}$

Table 5.3: The comparison of the mean ΔT recalculated to 150 V/m and its standard deviation between the temperature probes for both systems between readjusting the amplitude to a constant E_{rms}-field and no readjustment and decreasing E-field.

The E_{rms}-field decreases by 7.5 % for the BC and by 8.0 % for the LES. With no readjustments of the amplitude, the decrease in the E_{rms}-field leads to a smaller ΔT in both systems of 3.80 % and 4.95 %, respectively, and thus to an underestimation of the potential ΔT.
Although the effect of the readjustment on the E_{rms}-field in the BC was tested in this work, it is not common in the standard procedure. Instead, the decrease is only limited to a level of < 0.25 dB. If this requirement is not fulfilled, the standard requires additional analysis.
The difference between the ΔT in the LES with readjusted amplitude and the ΔT in the BC without readjustment of the amplitude for the SAIMD-2 is 7.99 %. Therefore, in any system, it is recommended to readjust the amplitude and monitor the E_{rms}-field during the measurement.
The next section describes a more comprehensive study with 3D extended objects, comparing the current ASTM F2182 approach in a BC with a potentially optimized approach in the LES.

5.2 Influence of the E-field distribution on 3D extended objects

A second comparison study between the BC system and the LES is carried out to investigate the extent of the influence of the E-field distribution on representative 3D extended objects as passive implants. The current ASTM F2182 standard recommended test method for passive implants as described in section 2.3 is used in the BC and potential optimizations enabled by the LES are investigated. As recommended, the optimal test position for a BC and in the ASTM phantom is at 20 mm distance from the wall with the main extension of the TO aligned with the z-axis. At this position, the amplitude of the E_{rms}-field is the highest and the RF coupling with the phantom surface is minimized. Additionally, the incident E-field distribution at this position is most likely to fulfill the ± 1 dB homogeneity requirement.
For the LES, the E_{rms}-field measurements shown in section 4.3.2.2 result in an optimal test position for 3D extended objects with 0° phase difference at the isocenter of the phantom aligned with the z-axis.
Six Allen keys are used as TOs, varying in length, width and diameter to represent the dimensions of the wide range of passive implants, schematically presented in Fig. 5.3.

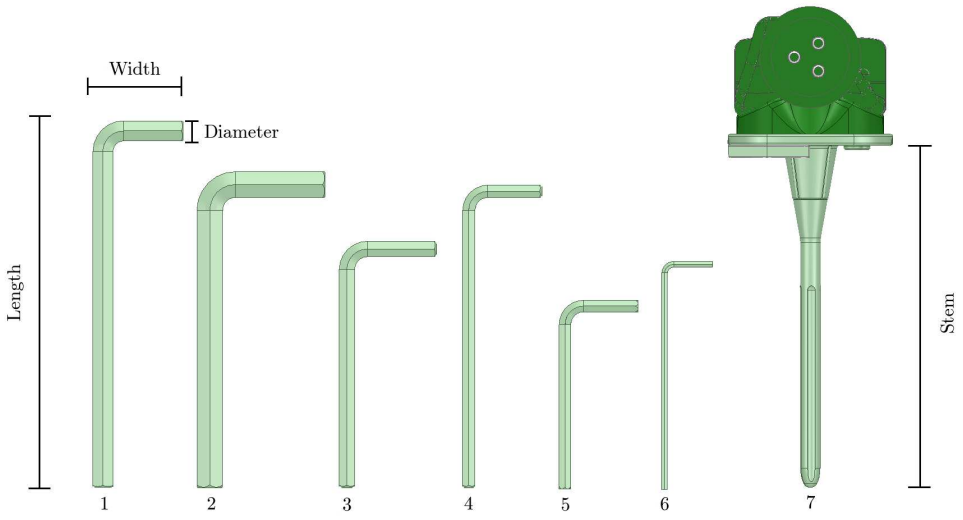

Figure 5.3: Schematic overview of the used test objects including the definition of the length, width and diameter, the number of the test objects and the stem of the generic knee, reused from Ref. [14].

Chrome-vanadium-steel is used for the Allen keys, which ensures a high ΔT. The aim of this study is to compare the ΔT produced in both systems under precise measurement conditions, such as a high SNR, and not to report the ΔT of the objects at a specific *in vivo* incident E-field. Therefore, any TO with the desired dimensions can be used, although it would never be allowed inside an MR scanner. Additionally, one generic knee implant is tested in both systems as an exemplary realistic implant. The TO parameters are listed in table 5.4.

TO	Length [mm]	Width [mm]	Diameter [mm]
1	175.0	43.0	9.53
2	123.0	50.0	10.00
3	96.5	38.0	6.00
4	118.0	27.0	4.76
5	74.0	29.0	4.50
6	90.0	19.0	2.25
7	200.0	60.0	10.00

Table 5.4: The listing of the different dimensions length, width and diameter of the seven test objects, modified from Ref. [14].

Since the ΔT must be normalized to the square of the incident E-field to compare the results of the two systems, the incident E-field was measured at each TO position for the size of the TO area.

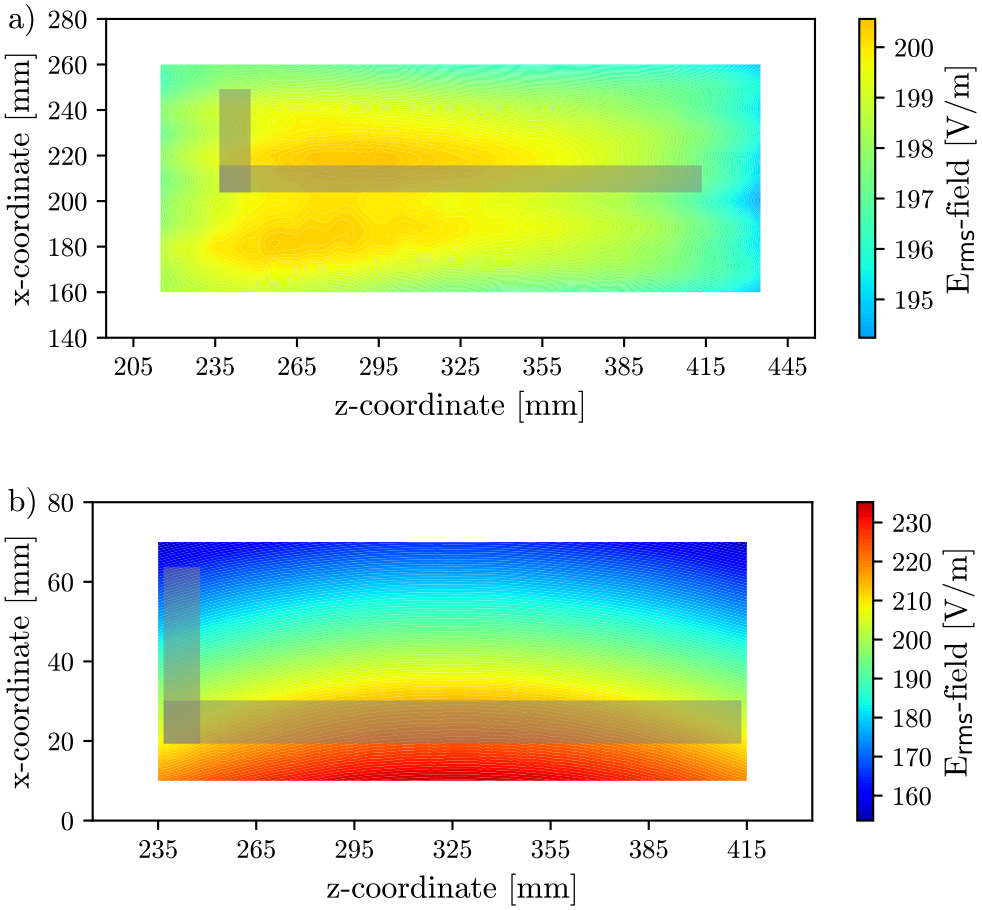

Figure 5.4: The incident E_{rms}-field distribution and the schematic individual test position exemplary for test object 1 for a) the LES and b) the BC, modified from Ref. [14].

Therefore, the E_{rms}-field probe was placed in both systems and lines with 10 mm distance were measured. The incident E_{rms}-field measurements are presented in

Fig. 5.4, including the schematic TO position. The color bar in Fig. 5.4 is scaled to the value range of the E_{rms}-field in each system and the value range of the y-axis varies for both systems according to the measurement position in x-direction. The expected E_{rms}-field distributions for both systems and the homogeneity for the LES are confirmed. The E_{rms}-field is homogeneous over the entire measurement area for the LES, while the E_{rms}-field varies substantially in the BC. The mean E_{rms}-field over the different TOs volumes are listed in table 5.5 for the LES and in table 5.6 for the BC.

TO	$E_{\mathrm{rms}}^{\mathrm{mean}}$ [V/m]	$E_{\mathrm{rms}}^{\mathrm{min}}$ [V/m]	$E_{\mathrm{rms}}^{\mathrm{max}}$ [V/m]	Deviation + [%]	Deviation - [%]
1	197.3	192.3	198.6	0.7	2.5
2	204.0	198.7	205.3	0.6	2.6
3	201.8	198.0	202.7	0.5	1.9
4	201.8	199.2	202.4	0.3	1.3
5	197.3	194.9	197.9	0.3	1.2
6	197.3	195.8	197.6	0.2	0.8
7	199.4	197.0	200.5	0.5	1.2

Table 5.5: The listing of the mean, minimal and maximal E_{rms}-field for each test object including the maximum deviation inside the LES, modified from Ref. [14].

TO	$E_{\mathrm{rms}}^{\mathrm{mean}}$ [V/m]	$E_{\mathrm{rms}}^{\mathrm{min}}$ [V/m]	$E_{\mathrm{rms}}^{\mathrm{max}}$ [V/m]	Deviation + [%]	Deviation - [%]
1	215.5	166.2	226.6	5.2	22.9
2	214.8	163.3	226.7	5.6	24.0
3	218.1	179.3	226.6	3.9	17.8
4	220.9	190.6	226.6	2.6	13.7
5	221.0	193.2	226.6	2.5	12.6
6	223.2	202.3	226.8	1.6	9.4
7	187.8	143.4	224.0	23.6	19.3

Table 5.6: The listing of the mean, minimal and maximal E_{rms}-field for each test object including the maximum deviation inside the body coil, modified from Ref. [14].

The E_{rms}-field values from the tables confirm the distributions in Fig. 5.4. For the BC, the negative deviation of the E_{rms}-field is larger than the positive deviation due to the strong x-gradient. The negative deviation increases with the width of the TOs. For the knee, the deviation in both directions is more similar, because the stem is placed at 50 mm distance from the wall and the joint expands symmetrically in both x-directions, with the smallest distance from the wall of 20 mm. Only two TOs 5 and 6 are within the homogeneity requirement of $\pm 12.6\,\%$, for the other TOs the deviation increases up to 24.0 %.
For the LES, the x-gradient is slightly stronger than the z-gradient. However, the maximum deviation of the E_{rms}-field is $-2.6\,\%$. For each TO, the incident E_{rms}-field was additionally measured, starting from the tip position with a resolution of 1 mm.

The E_{rms}-field along the TOs for both systems is additionally presented in Fig. 5.5 to highlight the influence on the TO dimensions, especially in the x-direction.

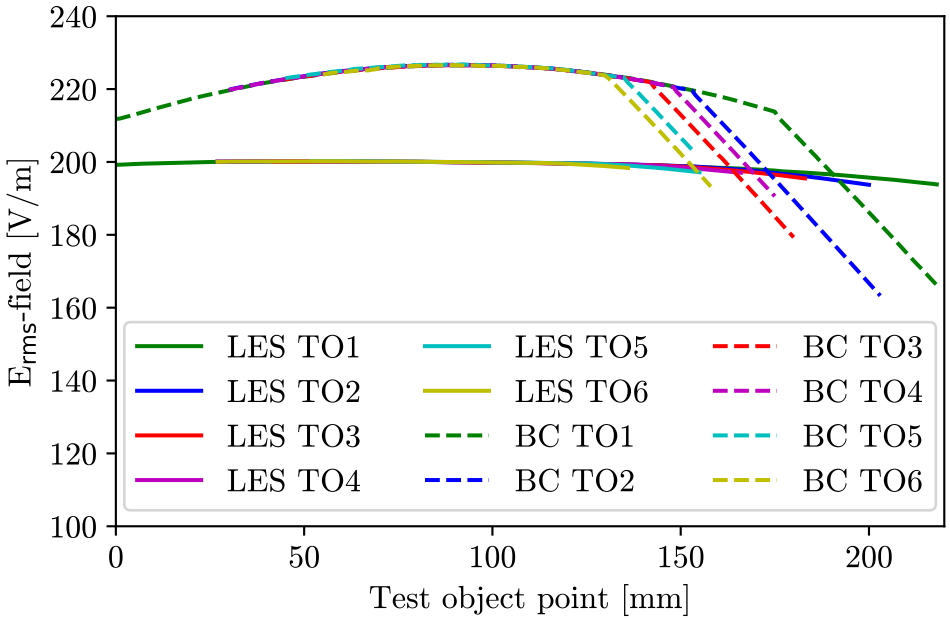

Figure 5.5: The E_{rms}-field distribution along the first six test objects for the body coil in dashed lines and for the LES in solid lines in position relation to each other, reused from Ref. [14].

The E_{rms}-field distribution in the body coil along the TOs illustrates that an implant expansion in the x-direction has a huge influence on the incident E-field. The part along the z-axis would have been within the homogeneity requirement, but even in this case the deviation in the LES is smaller.

After measuring the incident field per TO and system, the resulting ΔT is measured and normalized to the square of the mean incident field. To measure the ΔT for the TOs, two temperature probes (TS5) were placed at the center and at the edge of the TO tip. In addition, one temperature probe was fixed to the E_{rms}-field probe and both were placed at a reference location, as shown in Fig. 5.6. The TS5 probes with the coated crystal were chosen, to reduce the risk of probe damage. To ensure the same distance between the crystal and the TO, the temperature probes were positioned orthogonally at the TO. The TO and the probes were placed in the phantom filled with 90 mm of gelled TSM. The input power per system was individually set to a specific E_{rms}-field value at the reference position. During post-procession, the E_{rms}-field value at the reference location was transferred to the corresponding incident E-field at the TO location. For each measurement, the amplitude was readjusted to the desired value with a variation of $\pm 2\,\mathrm{V/m}$ to reduce the influence of the E-field decrease found in section 5.1. For each TO, ten measurement runs were performed with a measurement time of six minutes. After seven runs with the TO in place it was removed from the phantom as the temperature probes remained in place. Three additional runs were performed without the TO to measure the background ΔT. The entire procedure was repeated for all seven TOs, for a total number of 70

runs per system, with each TO was measured on a different day. Between the runs, the TSM was stirred to homogenize the temperature of the TSM in the phantom. This was done differently for the two systems. Since the phantom is accessible in the LES, the stirring is done without moving the setup. For the BC, however, the phantom had to be moved out of the system to stir the TSM. After stirring, the phantom was returned to the measurement position. Not only does this take more time, but the risk of inadvertently moving the TO or temperature probes, or not placing the phantom exactly where it should be, increases the likelihood of error.

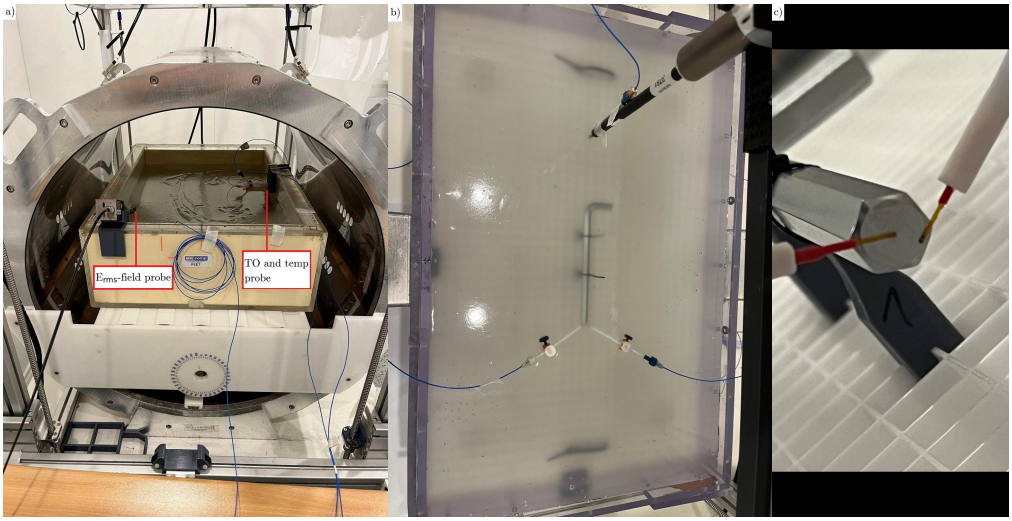

Figure 5.6: The measurement set up, including the phantom, the gelled TSM, the test object and the reference probes inside in BC in a) and the LES in b) and the temperature probe placement at the tip of the test object in c), reused from Ref. [14].

The frequency for the LES is set at 64.00 MHz for all measurements. For the BC, however, the frequency is set at 63.00 MHz and adjusted after $3-4$ runs to a maximum of 63.08 MHz to reduce the reflection. In total, a measurement run in the BC took 14 minutes, including two minutes of pre- and post-measurement monitoring, movement, and stirring. The same procedure in the LES took 12 minutes, reducing the total measurement time by 20 minutes.
The temperature probe at the reference location monitored the conditions in both systems and thus their stability and repeatability between the measurement runs and the measurement days. The ΔT at the reference location for all 70 runs per system are displayed in Fig. 5.7. The mean ΔT is $0.91 \pm 0.09\,°C$ for the LES and $1.56 \pm 0.20\,°C$ for the BC. The ΔT at the reference location is stable for the LES during the ten runs per day and between the different measurement days. For the BC, the deviation is larger and with a slight tendency during the measurement day, where the ΔT increases with the accumulated measurement time during the day. The absolute ΔT for the reference temperature probe is higher for the BC, because the temperature probe is placed in a location with a higher incident E-field, compared to the location inside the LES.
To compare the ΔT at the tip of the TO of the different systems, the mean ΔT and its standard deviation over the seven runs are calculated for each TO. This result is normalized to the corresponding mean incident E-field over the TO volume. The

ΔT at the TO tips for both systems are presented in Fig. 5.8, where the ΔT at the center and at the edge of each TO are included.

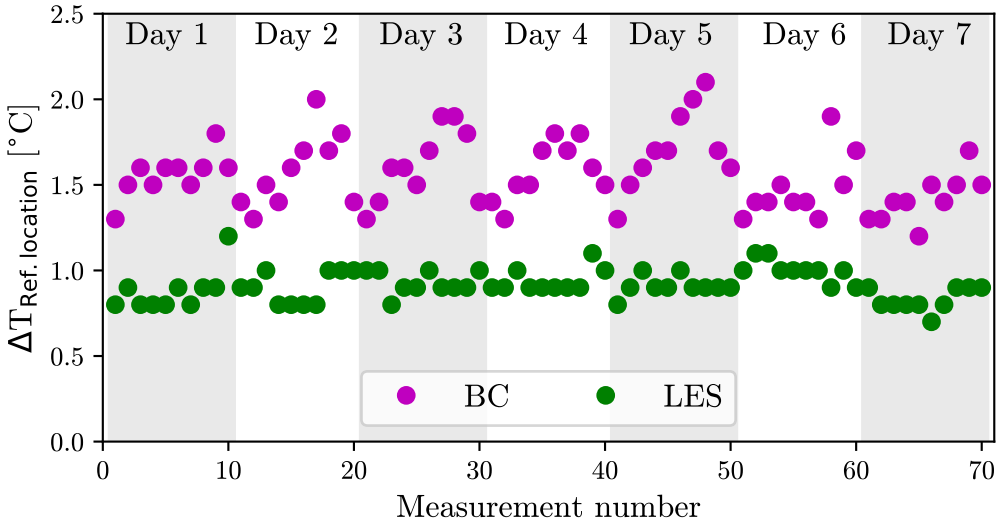

Figure 5.7: The ΔT at the particular reference position in each exposure system over all ten measurements per test object and measurement day, modified from Ref. [14].

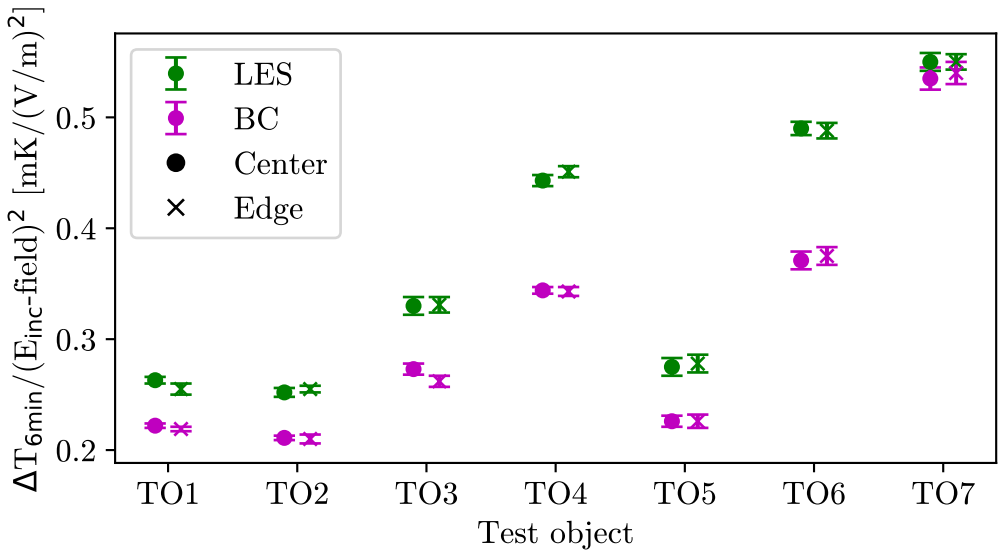

Figure 5.8: The temperature rise ΔT normalized to the squared incident field of each test object in both exposure systems for both temperature probe positions at the center and at the edge, modified from Ref. [14].

The difference between the ΔT at the edge and at the center of the tip is within the standard deviation of the seven measurements for each TO. The ΔT per TO is correlated for both systems. However, the ΔT scaled to the incident field is significantly lower in the BC for all TOs compared to the LES. The relative difference

of the ΔT in the BC to the ΔT in the LES varies between 14.2 % and 24.3 %, resulting in a significant underestimation of the potential patient risk for the BC.
The absolute ΔT at the tip ranges from 9.7 °C to 21.9 °C. The standard deviation of the measured ΔT is between ±0.1 °C and ±0.4 °C for the BC and between ±0.1 °C and ±0.3 °C for the LES. The standard deviation tends to increase with the absolute ΔT, which increases as the TO diameter decreases. The smaller diameter increases the gradient of the temperature distribution, making the measurement more sensitive to a measurement error due to small movements during the stirring.
For the generic knee implant, the scaled ΔT for the LES is also higher than for the BC, but within the standard deviation of the measurement. This may be due to the position at 50 mm distance from the wall, but should be further investigated for different positions and TOs.
Furthermore, the difference of the normalized ΔT of the TOs between the systems correlates not only with the inhomogeneity of the incident E-field, but also with the shape of the distribution and thus with the alignment between the TO and the tangential E-field component. For the LES, the tangential component is aligned with the z-direction and for the BC it is slightly curved, as indicated in Fig. 5.4. Thus, it is not aligned with the TO over its entire length.
The absolute ΔT depends, as expected, on the length of the TO and the diameter, with the diameter having the greater influence.

As a final step in the study concerning the testing of passive implants, the influence of imprecise positioning of the TO is investigated. The strongest gradient is the x-gradient compared to the y- and z-gradient. Therefore, the mean incident E_{rms}-fields for the cases where the TOs are shifted ±5 mm in the x-direction are calculated from the incident field measurement presented in Fig. 5.4. The resulting E_{rms}-fields are listed in table 5.7 for both systems.

	LES E_{rms} [V/m]			BC E_{rms} [V/m]		
TO	$E_{\mathrm{rms}}^{x_0}$	$E_{\mathrm{rms}}^{x_{-5}}$	$E_{\mathrm{rms}}^{x_5}$	$E_{\mathrm{rms}}^{x_0}$	$E_{\mathrm{rms}}^{x_{-5}}$	$E_{\mathrm{rms}}^{x_5}$
1	197.3	197.1	197.4	215.5	221.0	211.1
2	204.0	203.8	204.1	214.8	220.3	210.4
3	201.8	201.6	201.9	218.1	223.6	213.6
4	201.8	201.6	201.9	220.9	226.5	216.4
5	197.3	197.1	197.4	221.0	226.6	216.5
6	197.3	197.1	197.4	223.2	228.9	218.6

Table 5.7: The listing of the calculated mean incident E_{rms}-field over the test object volume for a test object shift of ±5 mm for the first six test objects in both exposure systems, modified from Ref. [14].

The incident E_{rms}-field calculations illustrate, that the E_{rms}-field for the LES does not vary despite changing the TO position 5 mm in both x-directions. For the BC, the mean incident E_{rms}-field varies by up to 2.6 % from the value at the desired position at x_0.
The ΔT per position per incident E_{rms}-field is calculated for each TO and system, presented in Fig. 5.9. The ΔT in the LES is stable and does not depend on the misplacement of ±5 mm. For the BC, however, the incident E_{rms}-field deviation of up to 2.6 % leads to a ΔT difference of up to 5.1 % for the different positions.
Compared to the BC, the smooth E_{rms}-field distribution of the LES does not cause

any additional uncertainty due to the misplacement. This analysis leads to the conclusion that the LES has a substantial advantage over the BC, since the position uncertainty has a smaller influence on the E_{rms}-field and ΔT for the LES. This leads to a simplified setup which corresponds to a reduced time to prepare the measurement.

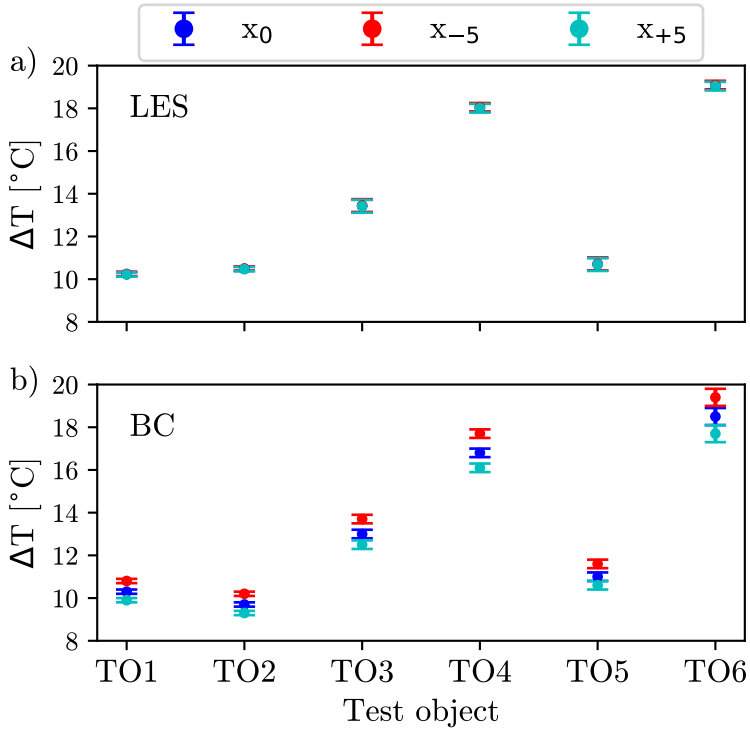

Figure 5.9: The resulting ΔT for all three test object positions for each test object inside a) the LES and in b) the BC, modified from Ref. [14].

5.3 Summary and discussion

Two analyses were presented in this chapter. A comparison between a BC exposure system and the LES was performed to determine if the LES could compete in performance with conventional BC systems and replace them to take advantage of the benefits discussed in chapter 4.
First, a study with elongated objects is performed, followed by a more comprehensive study with 3D extended objects. With these, not only the ΔT in both systems is compared, but also the sensitivity of the results to imprecise placement of test object.
The measurement procedure is as similar as possible in both systems. However, due to its greater accessibility, the total time required for the LES measurement series is less than that of the BC. For the BC, the phantom must be moved in and out of the coil to stir the TSM. Imprecise placement of the phantom and small movements of the measurement probes or the TO cannot be ruled out. Once the phantom is placed in the coil, the setup is no longer accessible. In the LES, no movement of the

phantom is required to stir the TSM between the measurement runs. In addition, the placement of the probe and TO is visible and can be monitored throughout the measurement.
Furthermore, the resonance frequency of the BC changes slightly from day to day and during a measurement day. Depending on the room temperature and the measurement time, the metallic components expand slightly due to heating by the current, changing the capacitance of the capacitors. The changed capacitance leads to a small change in the resonance frequency. For the study with the 3D extended objects, the frequency is adjusted every three to four runs. It is set between 63.00 MHz and 63.08 MHz. Depending on the coil design, a frequency adjustment may not be necessary for other coil systems.
The LES is resonant at a stable frequency of 64.00 MHz during all measurements and measurement days. In addition, the LES is not as frequency dependent, because the resonance is more broadband.
In both systems a readjustment of the amplitude during a measurement run can be done, so that the E_{rms}-field at the reference location is stable to $\pm 2\,\mathrm{V/m}$. This influence is investigated for one elongated object. The ΔT without readjustment of the amplitude compared to the ΔT with readjustment is 3.80 % and 4.95 % smaller for the BC and LES, respectively. Therefore, the readjustment of the amplitude is included in the measurements of the study with the 3D extended objects.
In addition to the advantages of accessibility and time reduction, the E-field distribution of the LES results in higher ΔT for all TOs in both studies. The E_{rms}-field distribution of the LES at the TO volume is comparable to a plane wave setup, where the TO is exposed to a homogeneous tangential E-field in amplitude and phase over the entire TO. The maximum deviation is 3.05 % from the mean E_{rms}-field value over the TO volume.
The deviation of the E_{rms}-field of the BC is higher for all TOs compared to the LES. For several TOs, the deviation is even greater than ± 12.6 %, increasing up to 24.0 %. Not only is the E-field homogeneity reduced in the BC, but also the direction of the E-field is not tangential over the entire length of the TOs. This results in a significantly lower ΔT for all TOs. The difference between the normalized ΔT to the mean incident E-field is between 4.02 % and 11.88 % for the elongated objects and between 14.2 % and 24.3 % for the 3D extended objects between the systems. Therefore, the ΔT inside the BC is underestimated.
The sensitivity of the measurement results to imprecise placement of ± 5mm in the x-direction of the TO is reduced to insignificance in the LES, while imprecise placement in the BC results in a ΔT difference of up to 5.1 %.
Overall it is shown, that the LES provides reliable and stable results for all TOs and measurements. The measurement procedure is more user friendly, less time consuming and less sensitive to placement or movement errors. For all TOs, the incident E-field in the LES is a worse case for the TO, resulting in a higher ΔT per incident E-field compared to the BC. This general underestimation of the ΔT of the BC due to the incident E-field distribution should be avoided in any case and a worst case of the incident E-field should be determined for each object individually. It is essential to determine the highest possible ΔT for a given mean incident field in order to correctly estimate the patient risk. If the ΔT for a mean incident field does not represent the worst case, the patient risk will be underestimated and may result in serious damage.

Whether the worst-case incident E-field is the plane wave setup should be determined prior to the measurement, e.g. by numerical prediction. If the plane wave setup is not be the worst case for a particular implant, the incident E-field distribution of the LES can be varied. This flexibility is an additional advantage of the LES over a BC or MR scanner, because the channels are individual and not connected to the same circuit.
In general, it is recommended that the amplitude be readjusted for each measurement, regardless of the system. In addition, more than one temperature run should be performed or more than one temperature probe should be used, although a combination of the two will provide the best statistics and standard deviation. The measurement results of the ΔT for the generic knee implant suggest that the minimum distance of 20 mm from the wall should be increased for more reliable results. Especially in the LES, an increased distance to the phantom wall is recommended, to avoid coupling between the antennas and the TO. The distance of the system components producing the E-field of the LES is significantly smaller than that of the BC or an MR scanner.
Considering the described advantages and the results of the measurements in both studies, the LES is an improved exposure system for testing passive implants, fulfilling all the requirements in table 2.3 and provides reliable ΔT results.

6 Improvement of the testing method for active implants

As described in section 2.4, the ISO/TS 10974 Clause 8 Tier 3 provides a procedure for assessing the safety risks of an active implantable medical device (AIMD) occurring due to RF-induced heating. To evaluate the heating of a specific object, the first step is to determine a mathematical lead electrical model, called a transfer function (TF), for each possible hot spot location, e.g. electrodes. This TF transforms the tangential incident E-field along the AIMD, measured or simulated in the absence of the AIMD, into the dissipated RF power or temperature rise ΔT. The TF can be developed numerically, analytically or experimentally. For this, the AIMD is exposed to a homogeneous E-field in amplitude and phase to measure its location-dependent response at the hot spot location [44].
In a second step, the TF has to be validated *in vitro* in a homogeneous TSM, as the AIMD is exposed to different incident E-fields along its trajectory, to cover a realistic distribution within an implantation volume during an MRI examination. The incident tangential E-field should vary in amplitude and phase, including, for example, ramps, linear changes, or phase reversal fields. Each individual tangential E-field along the TO represents one exposure condition. The ΔT at the hot spot should be measured for each individual exposure condition and compared with the corresponding TF prediction. If the TF prediction agrees with the measurement results, the TF can be used for *in vivo* predictions.
This chapter presents a novel combined validation approach that speeds up the process and potentially reduces the measurement uncertainty. The current approach suggests using different lead trajectories to change the exposure conditions for validation. This approach requires assembly and disassembly of the AIMD and the measurement probes inside the phantom for each trajectory. This is time consuming and inaccurate positioning can inadvertently bias the measurements. There is a strong temperature or E-field gradient within the hot spot distribution, so that the probe placement is the dominant uncertainty factor for this type of measurement, as discussed in section 3.2.
Other test laboratories use a vertically oriented BC and a cylindrical phantom to place the AIMD inside [56, 60]. They set up the AIMD and change the polarization between the two channels to change the exposure conditions instead of changing the trajectory and do not change the probe position. In [60], *Yao et al.* show that this approach is also valid when using two different trajectories. This approach is not feasible in the MR:comp test laboratory because the BC is in the horizontal orientation, required for the testing of passive implants. In addition, the cylindrical phantom is smaller than the ASTM phantom, which limits the placement possibilities of the measurement probes. Besides that, both channels of the BC feed into the same resonator circuit, limiting the variety of the E-field distributions within a phantom. A second exposure system used by *Song et al.* is a 300x300 mm rectangular E-field generator, and the measurement approach changes the trajectory within a homogeneous E-field based on the Hadamard matrix in Ref. [57, 58, 61]. This

exposure system is not only smaller, but the exposure conditions are limited and difficult to set up.
With the LES, it is possible to combine the advantages of the different approaches. As described in chapter 4, the entire phantom is accessible from the top. Therefore, the AIMD can be fixed to a measurement probe and both to the movement system. The whole complex can then be moved through the entire phantom to change the exposure conditions along the AIMD. In addition, the phase difference between the channels, the polarizations, can additionally be used to change the conditions at each position, since the channels can operate independently. With this measurement approach, a large number of measurements can be performed in a short time, since the probe position relative to the AIMD is fixed.
To investigate whether this approach is suitable for TF validation measurements, the standard test object SAIMD-U is used, which represents an active implant for which a validated TF is available [62]. In order to evaluate the extent of the time saving and uncertainty reduction, several questions have to be answered. First, the relation between the measured incident E_{rms}-field and the numerical predictions is investigated for additional polarizations compared to section 4.3.2.3.
In a second step, the possibility of using the E_{rms}-field probe instead of a temperature probe is investigated. Performing the validation procedure with the E_{rms}-field probe has several advantages. Saline solution can be used as the TSM instead of gel. The E_{rms}-field probe is able to measure the desired value in one second, whereas a temperature probe needs at least a few seconds to minutes for one measurement and is placed in gel where a waiting time for homogenization and stirring is necessary. After determining the repeatability of the E-field measurement with the SAIMD-U, the results are compared to the ΔT and the amplification due to the TO is calculated.
Then, going forward with the E-field probe, the difference between the measurement results with fixed probe-to-TO relation compared with readjusting the probe position for each TO position inside the phantom is evaluated.
For one explicit position, the radial hot spot distribution is measured to transfer the results from the fixed distance to the position with the highest expected ΔT.
To compare the TF predictions with the measured E-field at the TO tip, the tangential incident E_{tan}-field along the TO must be calculated from the numerical prediction for each position and polarization. Additionally, the influence of the TF resolution along the TO is investigated. After comparing the TF prediction with the measured values at the hot spot, the TF is calibrated. A second data set of different exposure conditions is measured to investigate whether the calibrated TF is valid for any kind of exposure conditions and therefore applicable to an *in vivo* situation.
Finally, an uncertainty analysis of this approach is performed and a validation criterion is defined.

6.1 Fixed measurement approach validation measurements

The TO used is the SAIMD-U [62]. It is an AIMD with an implantable pulse generator (IPG) with one 600 mm long insulated lead with a 2 mm long open tip. The diameter without insulation is 2 mm and the conductor diameter is 0.72 mm, as described in Annex U in Ref. [62] and presented in Fig. 6.1a). The normalized TF

for the SAIMD-U is provided in Ref. [62] and is available in a 20 mm resolution. This TF has already been validated and is therefore ideal for validating the measurement approach within LES.
The TO trajectory used for the measurement is the U-shape, shown in Fig. 6.1a). The distance between the straight parts is 120 mm, to avoid any coupling [63]. The U-shape is chosen to potentially expose the TO to E_{rms}-field conditions, where the field along the two straight parts of the U are of the same or the opposite phase. For these particular exposure conditions, the E_{rms}-field or temperature at the hot spot is the lowest and highest [60].

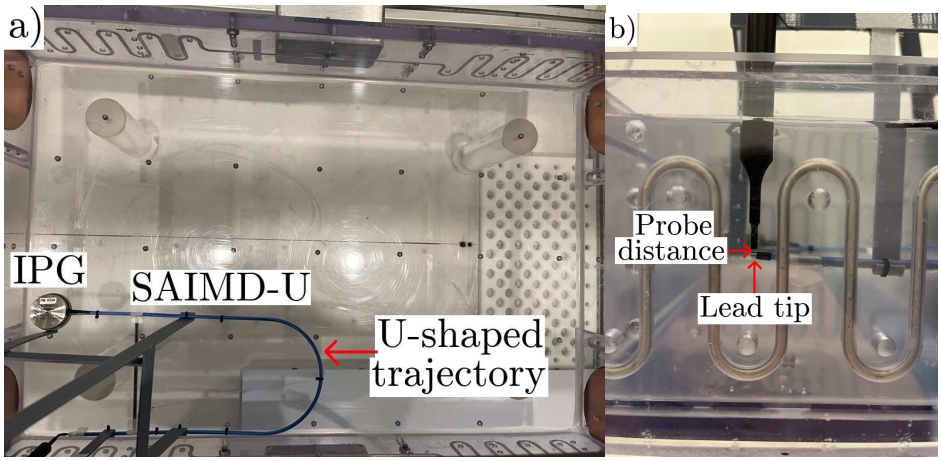

Figure 6.1: The measurement setup of the SAIMD-U mounted in an U-shaped trajectory to the holder and the movement system in a) and the measurement probe fixed at the measurement position and placed at the starting position of the measurement series in b).

6.1.1 Incident E-field

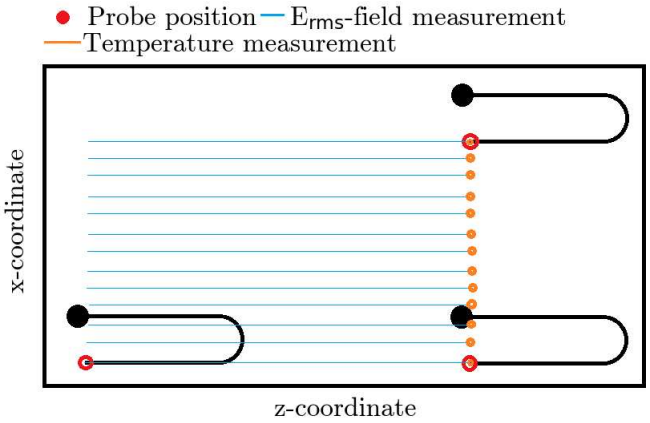

Figure 6.2: Schematic overview of the mapping movement and resulting measurement positions for the E_{rms}-field measurement and the temperature measurement inside the phantom with and without the test object in place, modified from Ref. [13].

The first measurement is performed with the Easy 6 system and the phantom is filled with 90 mm height saline solution as TSM without the TO, to measure the incident field. The E_{rms}-field probe is fixed to the movement system and vertically oriented. The start position is at [20/45/60].

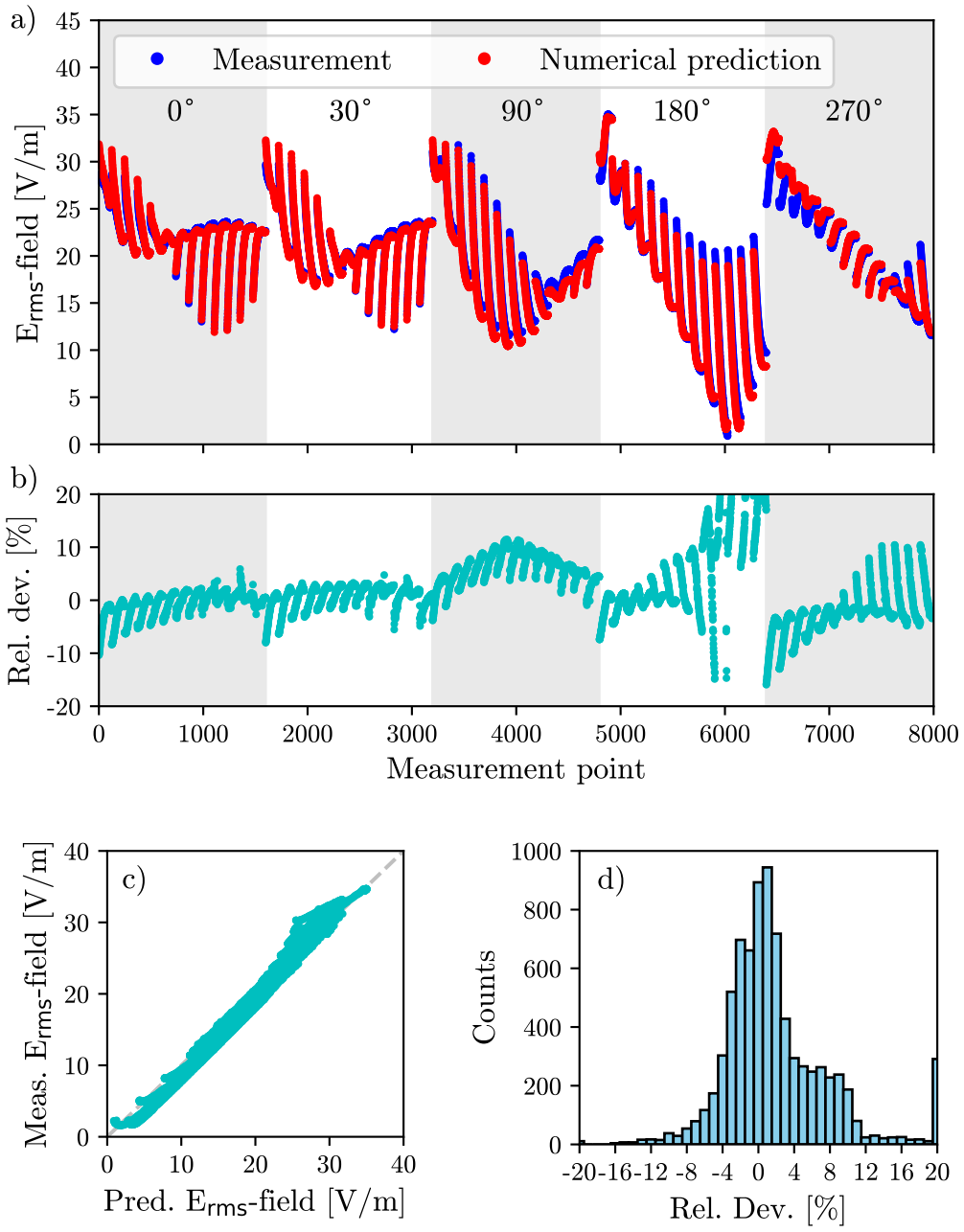

Figure 6.3: The comparison between the measured and numerical predicted incident E_{rms}-field for different polarizations in a), the relative deviation of the measured E_{rms}-field compared to the predicted E_{rms}-field for each exposure condition in b) and counted in a histogram in d). Additionally, the correlation between measured and numerical predicted E_{rms}-field is shown in c).

After the system is turned on and a waiting time of 15 minutes for the E_{rms}-field value to stabilize, the E_{rms}-field mapping begins. The input power is $-25\,\mathrm{dBm}$, which is also used for all other measurements involving the SAIMD-U and the E_{rms}-field probe. The E_{rms}-field probe is moved 305 mm in the z-direction with a step size of 2.5 mm and then 20 mm in the x-direction to measure the next line in the z-direction. A total of 13 lines are measured, covering a plane of 305 mm by 240 mm, as schematically displayed in Fig. 6.2. This measurement volume is the same as for the measurement with the TO in place, so that the closest proximity between the TO and the phantom walls is 20 mm. Fig. 6.2 shows the measurement lines measured with the E_{rms}-field probe and the measurement positions where the ΔT is measured, which will be described in detail in section 6.1.2.
This E_{rms}-field mapping procedure is repeated for different polarizations, in particular 0°, 30°, 90°, 180° and 270°, resulting in a total of 7995 values. The correlation of the measured incident E_{rms}-field without the TO in place and the incident E_{rms}-field extracted from the numerical predictions for all five polarizations for each grid position and thus exposure condition is presented in Fig. 6.3. The mean value and the standard deviation of the relative difference of the measured incident E_{rms}-field compared to the numerically predicted incident E_{rms}-field for all five polarizations is $2.54 \pm 9.46\,\%$. The relative deviation is less than $\pm 10\,\%$ of the entire measurement volume, except for the E_{rms}-field values less than $10\,\mathrm{V/m}$ in the center of the phantom for 180° and the lines at close proximity to the phantom wall for all five polarizations, as observed in section 4.3.2.3. At close proximity to the phantom walls, the influence of reflection effects and low SNR is increased. The relative deviation does not increase substantially for the different polarizations. Therefore, it is assumed that the relative deviation for other polarizations is also within $\pm 9.46\,\%$.

6.1.2 E-field and temperature measurements at the hot spot

E-field measurement with the test object

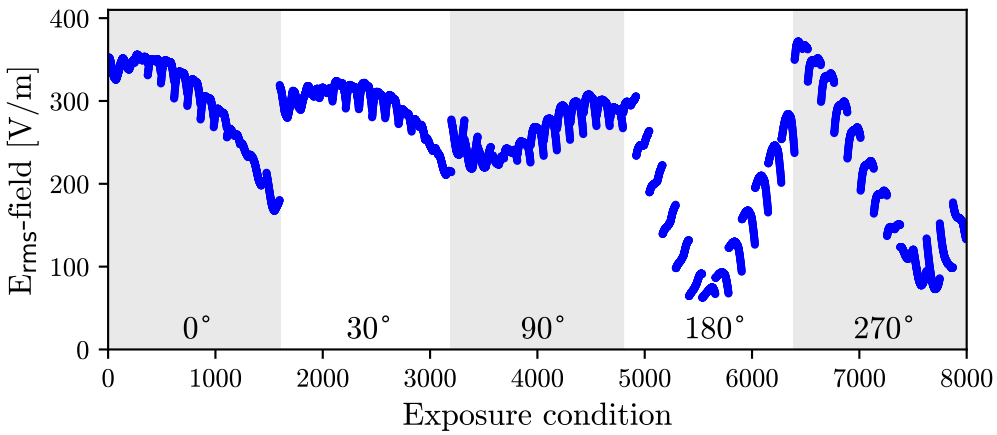

Figure 6.4: The measured E_{rms}-field at the test object tip for every position along the mapping grid for five different polarizations.

For the measurement with the SAIMD-U a holder is printed with a 3D printer. The TO is fixed to the holder in the desired shape and the holder is screwed to the movement system. In addition, the E_{rms}-field probe is attached to the movement system at a defined distance from the object's lead tip, i.e. the electrode. All fixation components are printed with polyactide (PLA) material to reduce the E_{rms}-field disturbances inside the phantom. The starting point of the measurement is the same as for the incident E_{rms}-field measurement. After the waiting time to stabilize the E_{rms}-field value, the same movement pattern is performed as before without the TO. Per polarization 1599 values are measured in approximately 30 minutes. This pattern is used for the same polarizations as in the incident E_{rms}-field measurement in section 6.1.1. The measured E_{rms}-fields at the TO tip are displayed in Fig. 6.4. The measured E_{rms}-field values for the different exposure conditions vary for each position and phase setting, resulting in a dynamic range between 62.6 V/m and 372.0 V/m.

Repeatability of the E-field measurements

To test the robustness and repeatability of the E-field measurement at the TO, the procedure is performed for three polarizations, 0°, 90° and 180°, on four different days and with two different types of TO holders over a period of 3 months, as the setup is assembled and disassembled each time.

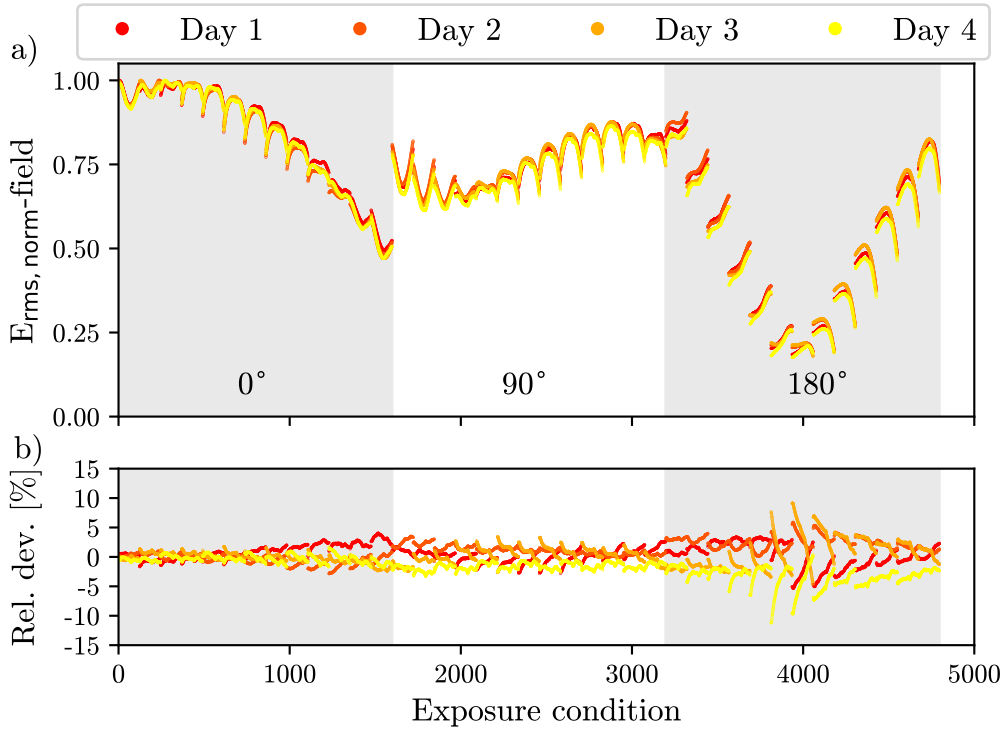

Figure 6.5: The comparison of the normalized E_{rms}-field measurement with the test object for 0°, 90° and 180° polarization at four different days in a), including the relative deviation per exposure condition to the mean E_{rms}-field in b).

The two different holders are used to investigate, whether the amount of material has a significant influence on the E_{rms}-field distribution. The distance between the E_{rms}-field probe and the lead tip is set to a starting E_{rms}-field between 300 V/m and 400 V/m, to achieve a sufficient SNR and to stay within the E_{rms}-field probe measurement interval. The distance is about 2-3 mm.

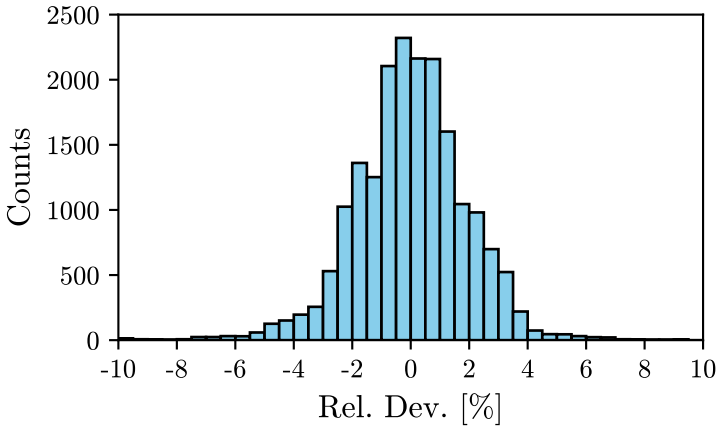

Figure 6.6: The relative deviation of the E_{rms}-field of each single measurement day compared to the mean value of the four days as histogram per exposure condition for three different polarization 0°, 90° and 180°.

Since the starting E_{rms}-field is different for each day, the normalized E_{rms}-fields are compared and presented in Fig. 6.5a). The mean E_{rms}-field of the four measurements per exposure condition is calculated and the relative deviation of the individual E_{rms}-field per day compared to the mean E_{rms}-field is also shown in Fig. 6.5b) and the histogram of the deviation in Fig. 6.6. Although the whole setup is rearranged for each measurement day, the distribution of the E_{rms}-field is repeatable. The mean value and the standard deviation of the E_{rms}-field due to the TO placement, the accuracy of forming the lead into the desired shape, and the amount of holder material is $0.00 \pm 1.92\,\%$. The relative deviation increases for the smaller measurement values due to the small SNR.

Temperature measurements with the test object

To confirm that these E_{rms}-field results are suitable for TF validation, a series of temperature measurements are performed in the gelled TSM. If the temperature rise confirms the E_{rms}-field, the E_{rms}-field probe can be used for further investigation. The holder of the TO is mounted on the movement system as before, and one temperature probe (TS2P) is fixed at the edge of the lead tip. The start position is at [20/45/365] as shown in Fig. 6.2, but due to the time required for a temperature measurement, only 13 measurement positions are selected. The measurement time per position is 30 seconds following a pause of two minutes for cool down, homogenization and movement to the next position. The temperature measurement is performed with different field polarizations of 0°, 90°, 180° and 270° and takes 36 minutes per polarization run with 13 measurement positions each. The input power for these temperature measurements is −15 dBm instead of −25 dBm to increase the SNR. The ΔT are listed in table 6.1. The measured ΔT changes substantially per

position and per polarization between 1.3 °C and 39.0 °C. These ΔT are scaled and compared to the previously measured E-field values measured under the same exposure conditions to validate the E-field probe for the TF validation measurement. Additional measurements are performed to convert these ΔT values to the actual ΔT at the −25 dBm.

Position x [mm]	ΔT_{0° [°C]	ΔT_{90° [°C]	ΔT_{180° [°C]	ΔT_{270° [°C]
20	36.0	23.2	27.3	39.0
40	37.2	21.1	20.7	36.2
60	36.5	18.8	14.2	31.2
80	34.9	17.7	8.7	25.3
100	32.6	17.3	4.4	19.4
120	29.9	17.8	2.1	14.5
140	27.4	18.9	1.3	10.0
160	24.7	20.3	1.6	6.4
180	21.9	22.0	3.2	3.8
200	18.7	23.4	6.0	2.2
220	15.6	24.3	10.0	1.9
240	11.9	24.0	14.7	2.9
260	8.5	21.6	19.2	5.7

Table 6.1: The measurement results of the temperature rise ΔT per position and for four different polarizations for an input power of −15 dBm.

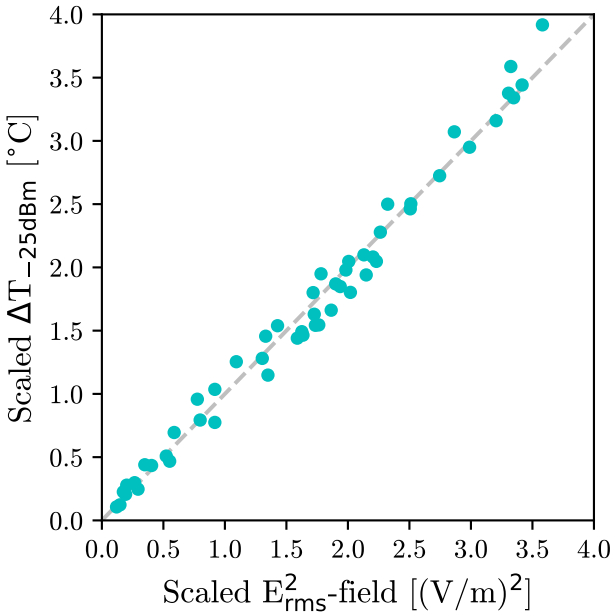

Figure 6.7: The correlation between the scaled temperature rise ΔT and the scaled and squared E_{rms}-field values for four different polarizations for an input power of −25 dBm.

At one position $x = 20$, $z = 365$ the ΔT is measured three times at 0° phase relation and -15 dBm input power. Then the input power is set to -25 dBm and the ΔT is measured three times at the same position for each polarization 0°, 90° and 180°. The mean amplification factor over the three polarizations at this position between the ΔT at -15 dBm and -25 dBm input power is 10.89 ± 0.42. This factor is applied to all ΔT values from table 6.1 and are compared with the E_{rms}-field values at the same positions. The ΔT is proportional to the square of the E_{rms}-field. To compare the results of the temperature measurement with the E_{rms}-field measurement, the E_{rms}-field values are squared and scaled, according to equation 3.2.1. The scaling factor between the ΔT and the recalculated E_{rms}-field values is 3.26 ± 0.18. The scaling is necessary because the distance between the TO and the temperature probe is smaller than to the E_{rms}-field probe. The comparison between ΔT and the recalculated E_{rms}-field at the same position is presented in Fig. 6.7.
The squared E_{rms}-field and the ΔT are linearly correlated with $R^2 = 0.9838$. The mean value and its standard deviation of the relative difference of the squared scaled E_{rms}-field compared with the scaled ΔT is 0.92 ± 11.88 %. The dynamic range of the E_{rms}-field at the lead tip at -25 dBm is between 62.6 V/m and 372.0 V/m and between 1.3 °C and 39 °C for ΔT at -15 dBm. Thus, the resulting mean amplification for the ΔT between the exposure conditions due to changed TO position and polarization is approximately 32.7, calculated from the average of the squared difference between the conditions with the lowest and highest E_{rms}-field conditions and the difference between the lowest and highest ΔT at the hot spot. Also, it should be noted that -25 dBm is a very small input power that results in an incident E_{rms}-field at the measurement positions that varies between 0.9 V/m and 35 V/m.
Due to the linear correlation with $R^2 = 0.9838$ between the measurement modalities, the E_{rms}-field probe is suitable for TF validation measurements for this TO.

6.1.3 Distance between the E-field probe and the test object

To investigate the influence of the E_{rms}-field probe distance to the TO, two measurements are carried out. The first measurement illustrates the difference between the E_{rms}-field measurement when the E_{rms}-field probe distance is fixed and when the E_{rms}-field probe is repositioned for each measurement location. The second case mimics the approach currently recommended by ISO/TS, where different trajectories are used to change the exposure conditions. This will not only show that the deviation increases with repositioning, but also that the measurement time is drastically reduced by fixing the probe.
The second measurement determines the measurement distance between the fixed E_{rms}-field probe and the tip of the lead.

Probe arrangement

To investigate the influence of the E_{rms}-field probe rearranging versus the fixed measurement approach, both approaches are compared. For the polarizations 0° and 180° the measurement positions similar to the temperature measurement (see Fig. 6.2) are measured in two ways. Once the E_{rms}-field probe is fixed in the same way as for the previous measurements, but is dismantled and rearranged as precisely as possible, before it is moved to the next location. Measurement 1 corresponds to the values before rearranging and measurement 2 to the values after rearranging. This procedure took 45 minutes per polarization for the 13 positions. Because the

system must be turned off for rearranging and turned on again, the system is not in a steady state. A 15 minute waiting time per position is not feasible, so a 2 minute measurement time per position to average the E_{rms}-field decrease is set to minimize the deviation.
The other way is to measure the same positions without rearranging the E_{rms}-field probe, used as reference data. With this setup, the measurement time is 1:36 minutes per polarization and 15 additional minutes warming time of the system. In total, measuring the data for the fixed probe took less than 20 minutes. The data from the continuous measurement for the specific locations are taken from the measurement in Fig. 6.5 and used as a reference.
The E_{rms}-field values from the rearranging measurement are plotted against the reference data and and normalized, as displayed in Fig. 6.8.

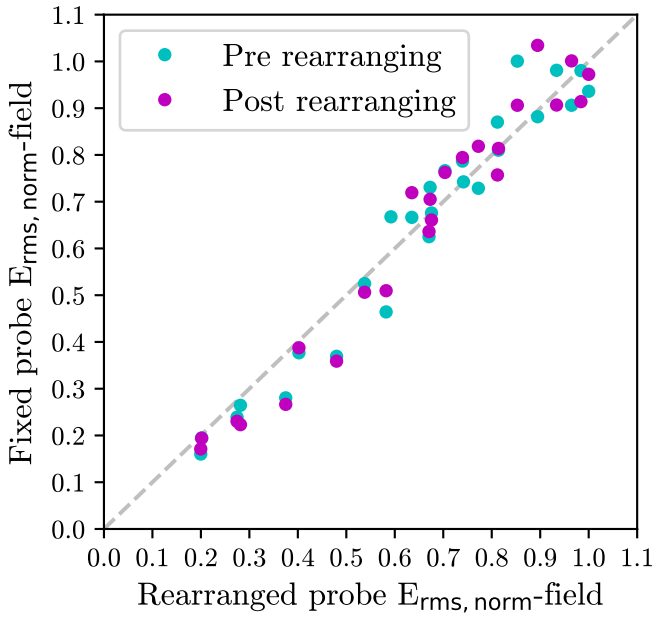

Figure 6.8: The correlation between the measurement of the E_{rms}-field with a fixed distance between measurement probe and test object and a different probe distance for each exposure condition.

The rearranging of the E_{rms}-field probe, and thus the change in distance between the E_{rms}-field probe and the TO, results in maximum relative deviation of up to 28.91 % compared to the same measurement positions with the fixed E_{rms}-field probe and distance. The relative standard deviations are 10.81 % and 11.46 % for measurement 1 and measurement 2, respectively. As expected, the standard deviation due to probe rearrangement is a large factor, since the radial decrease of the E-field is proportional to $1/r^2$ and therefore sensitive to varying distances on a scale of 0.1 mm, as evaluated in section 3.2.

Probe distance

An additional measurement is performed to estimate the distance between the E_{rms}-field probe and the lead tip. Because of the range of the E_{rms}-field probe, it is not possible to measure the field at the closest proximity to the lead tip. Therefore, it

is necessary to determine the actual distance and an amplification factor.
The TO is placed at the location that generates the lowest E_{rms}-field increase at $x = 140$, $z = 365$ with 180° polarization. This position is selected to prevent the E_{rms}-field probe from exceeding its range when the distance between the probe and the TO is reduced. This time the TO holder is not fixed to the movement system, but to the bottom of the phantom to allow the probe to move independently. The E_{rms}-field probe is fixed to the movement system and placed above the lead tip. It is placed as close as possible to the tip and moved in the y-direction with 0.1 mm steps. This is done three times for a total radial distance of 20 mm. The averaged E_{rms}-field in radial direction is presented in Fig. 6.9.

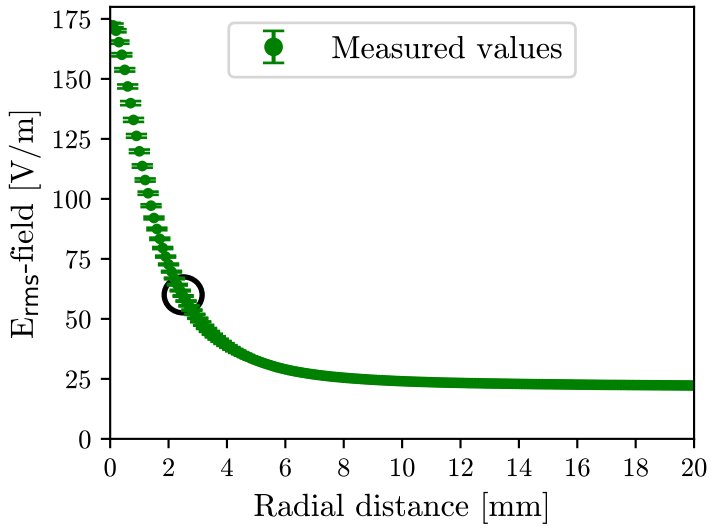

Figure 6.9: The radial E_{rms}-field decrease at the test object's hot spot averaged over three measurements. A distance of 0 mm represents the closest distance between measurement probe and test object tip.

The data show that the radial E_{rms}-field decrease is steep and that the E_{rms}-field reaches the background level after approximately 10 mm, as expected in section 3.2. The E_{rms}-field values of the previous measurements for this position are between 54.5 V/m and 66.2 V/m, as shown in Fig. 6.5, which corresponds to a distance between 2.2 mm and 2.7 mm, as marked with a black circle in Fig. 6.9 and displayed in Fig. 6.1. The distance is within $2-3$ mm, as expected in section 6.1.2. The mean maximum value at the closest position to the tip is 172.5 ± 0.9 V/m, which results in an average amplification factor of approximately 2.84 ± 0.19 between the E_{rms}-field at the probe position and the E_{rms}-field at the closest position to the lead tip.
The ΔT of 1.3 °C at −15 dBm at this position corresponds to a ΔT of 0.1°C at −25 dBm. Using equation 3.2.1 for a measurement period of 30 seconds, the ΔT of 0.1°C results in 188.1 V/m. This is in good agreement with the E_{rms}-field measurement and corresponds to an amplification factor of 3.09, which is within the uncertainty of the previously calculated value of 3.26 ± 0.18 in 6.1.2.
Although the distance between the E_{rms}-field probe and the lead tip is minimized, there is still a distance between the probe tip and the sensitive element and of approximately 1 mm. The measuring crystal of the temperature probe also has a

sensitive volume of approximately 1 mm^3. Therefore, the maximum E_{rms}-field value is less than the ΔT measured when the temperature probe touches the lead tip at an effective distance of 0.5 mm, and thus the amplification factor.
Furthermore, the progression of the E_{rms}-field in the radial direction has a strong field gradient over the first $2-3$ mm. Therefore, the E_{rms}-field probe shouldn't be placed at a greater distance than 3 mm. Since the measurement range of the E_{rms}-field probe is limited to about 400 V/m, the distance and the input power must be adjusted to achieve the highest possible SNR within the limits of the E_{rms}-field probe.

6.2 Transfer function predictions

To compute the TF predictions of the E_{rms}-field at the hot spot, the TF itself and the tangential E_{rms}-fields along the TO per exposure condition $\vec{E}_{\text{tan}}$ is needed according to equation 2.4.1. $\vec{E}_{\text{tan}}$ must be calculated from the numerically predicted E_{rms}-field results from section 4.3.2.2. The numerical predictions of the E_{rms}-field provide the amplitude and phase for each of the three components for each position with a resolution of 1 mm in the x- and the z-directions. Three matrices E_x, E_y, E_z are calculated for each component with a grid of 1x1 mm, including the complex numbers consisting of real and imaginary parts for the isoplane with the size of 651x421. In a second step, the trajectory is organized as a matrix for each component. The trajectory consists of two straight parts with a length of 206 mm each and a semicircle with a diameter of 120 mm, as presented in Fig. 6.1. The trajectory is planar in the xz-plane with no part in the y-direction, so only two matrices are developed, one for the x-component U_x and one for the z-component U_z, as presented in Fig. A.4. The straight parts of the trajectory are aligned with the z-axis. Starting from the lead tip, the first straight part of U_z is filled with $+1$ (parallel to the z-axis) and the straight parts after the semicircle are filled with -1 (antiparallel to the z-axis). For U_x the value 0 is entered for the straight parts (orthogonal orientated to the x-axis), which represent the tangential unit vectors per position and component.
The semicircle requires additional calculations. First, the length is segmented into pieces of equal length of 1 mm to fit the 1x1 mm grid. The circular function and its derivative

$$z = r - \sqrt{r^2 - x^2} \tag{6.2.1}$$

$$z' = \frac{x}{\sqrt{r^2 - x^2}} \tag{6.2.2}$$

are used, where the coordinate system is transferred in the xz-plane. For each position along the semicircle, the derivative and thus the tangential component is calculated and divided into the x- and z-components. The resulting values are normalized and entered on the 1x1 mm grids of U_x and U_z. For example, the result of $z' = 1$ will result in a value of 0.5 for each component in U_x and U_z for that position. Thus, these matrices contain the fraction of the E_{rms}-field per position and component. All remaining entries of the trajectory matrices are filled with 0, representing the empty spaces around the test object. Finally, U_x and U_z are converted to complex numbers with an imaginary part set to zero and a size of 121x266. To calculate the final $\vec{E}_{\text{tan}}$ for each position, a program is scripted that moves the trajectory matrices through the $E_{x,z}$-field matrices, calculating the sum of the piece wise products of $U_x * E_x$ and $U_z * E_z$ for each entry. The resulting matrix per position

contains the $E_{\tan}$ values, otherwise the value 0. The sparse matrix is used to reduce the resulting matrix to the desired $\vec{E}_{\tan}$ vector with 600 entries, corresponding to the lead length of 600 mm by using only the values different from zero to

$$\vec{E}_{\tan}1 = \begin{pmatrix} (U_x E_x + U_z E_z)_1 \\ (U_x E_x + U_z E_z)_2 \\ \cdot \\ \cdot \\ \cdot \\ (U_x E_x + U_z E_z)_{600} \end{pmatrix}. \tag{6.2.3}$$

For each position of the TO within the phantom and for each polarization one $\vec{E}_{\tan}$ is calculated. The requirements for the different $\vec{E}_{\tan}$ representing the exposure conditions are, that they should provide a wide dynamic range in ΔT and that they should vary in amplitude and phase. Some examples of the calculated $\vec{E}_{\tan}$ are shown in Fig. 6.10.

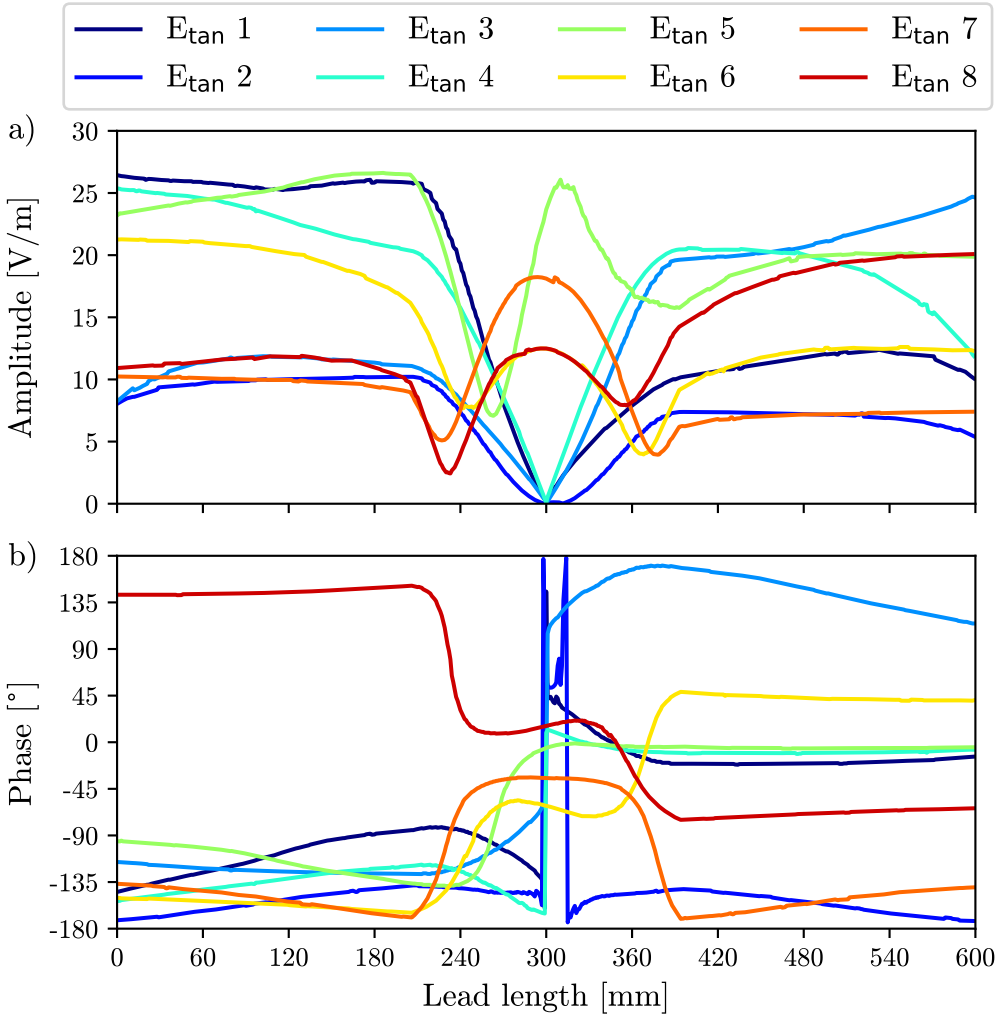

Figure 6.10: Examples of incident $E_{\tan}$-field distributions along the test object trajectory at different positions inside the phantom and different polarizations shown as a) amplitude and b) phase.

The exemplary $\vec{E}_{\tan}$ are selected from the positions and polarizations, where the temperature measurements were performed. There is a huge variety in amplitude and phase, including ramps (e.g. $E_{\tan}5$), linear parts (e.g. $E_{\tan}4$) and phase reversal fields (e.g. $E_{\tan}7$), as described in Ref. [4]. Furthermore, the dynamic range of ΔT, generated by these $\vec{E}_{\tan}$ results in a factor of approximately 32.7, as shown in Fig. 6.4 and table 6.1 in section 6.1.2.
For the validation process, all generated $\vec{E}_{\tan}$ are transposed and listed in a new matrix, to calculate the TF prediction of the E-field value at the tip of the TO.

For the SAIMD-U, the TF is available including a normalized amplitude and phase of the E_{rms}-field along the TO with a resolution of 20 mm in Ref. [62]. To obtain a $\overrightarrow{TF}$ with a 1 mm resolution as the $\vec{E}_{\tan}$, linear interpolation is used and the TFs with both resolutions are presented in Fig. 6.11.

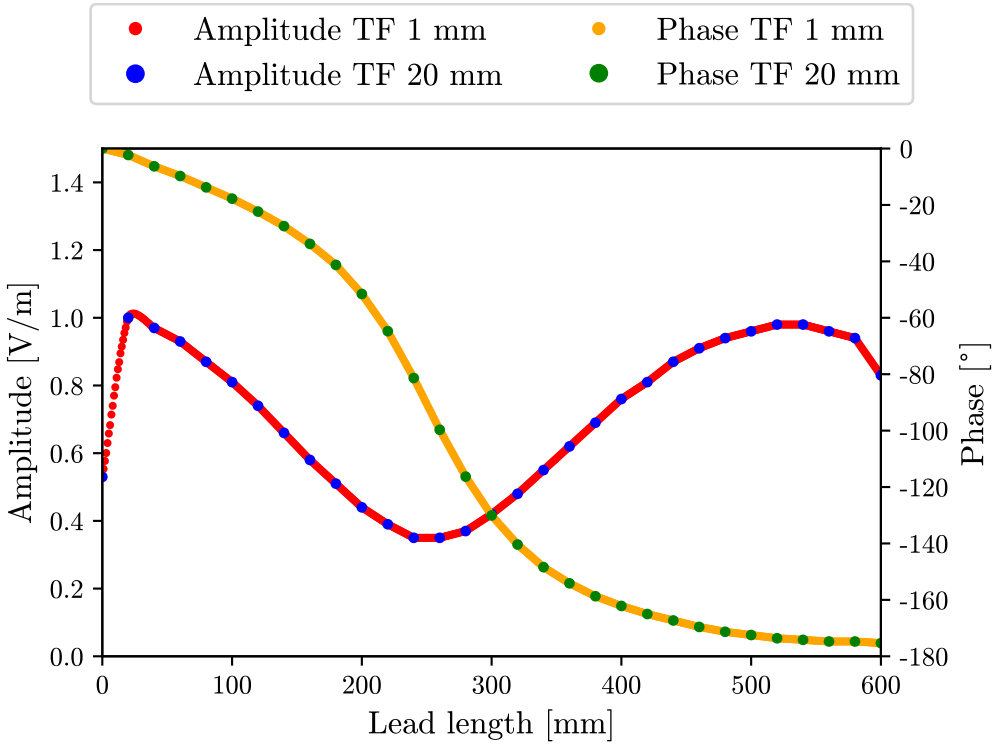

Figure 6.11: The amplitude and phase of the transfer function for 20 mm resolution from Ref. [62] and for the linear interpolated 1 mm resolution.

The interpolated TF with 1 mm resolution and the given TF with 20 mm resolution are further considered.
The $\overrightarrow{TF}$ vector is multiplied by the matrix containing all the $\vec{E}_{\tan}$. The difference of the results of this calculation with the TF of 1 mm interpolated resolution and 20 mm resolution is evaluated. The predicted amplitude and phase values of the two TFs multiplied by $\vec{E}_{\tan}$ for 0°, 90°, 180° and 270° are displayed in Fig. 6.12. The 1 mm resolution TF predictions for the E-field are on average 3.72 % smaller in amplitude than the 20 mm resolution TF results. The results of the predictions of the two TFs with different resolutions are compared to the E_{rms}-field measurements from section 6.1.2 with the TO in the next section.

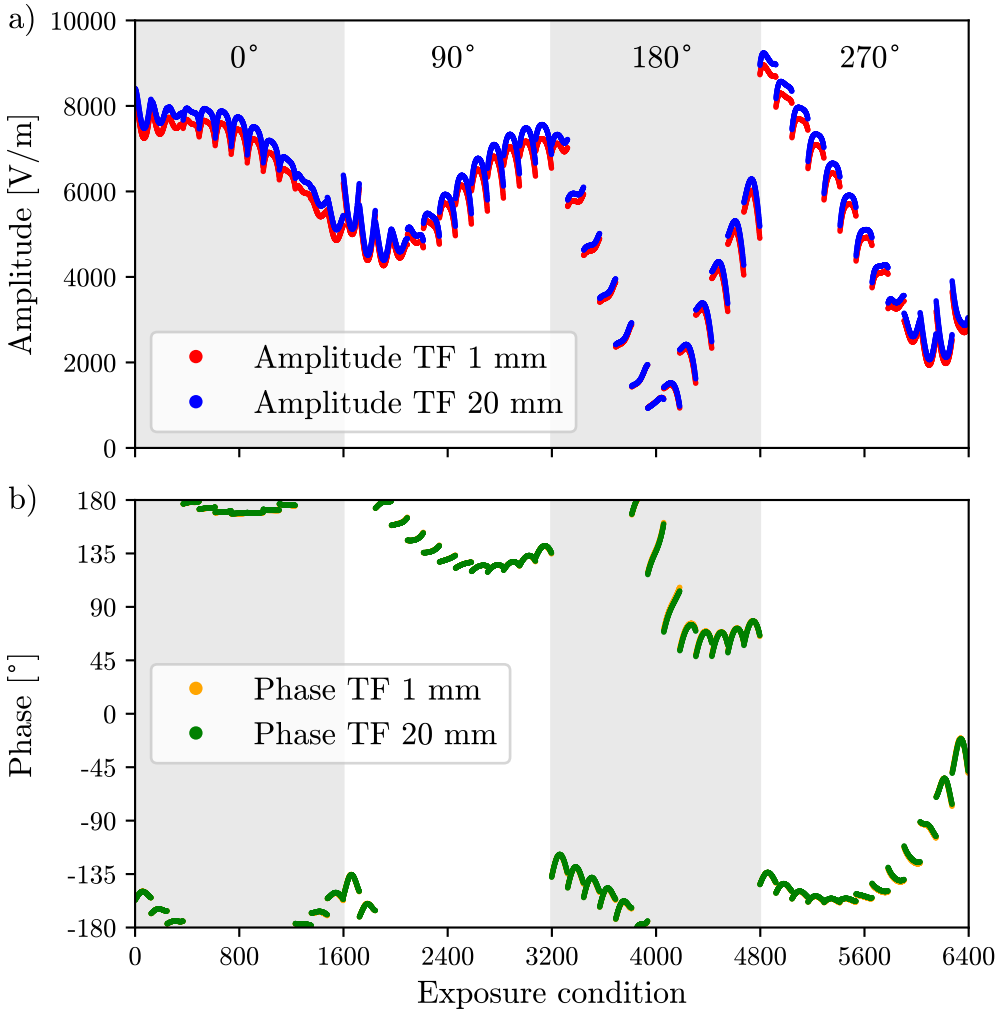

Figure 6.12: The predicted E_{rms}-field from the transfer functions with both resolutions for each exposure condition for the polarizations of 0°, 90°, 180° and 270° in a) amplitude and b) phase.

6.3 Calibration and Validation

To compare the measurement results from the E_{rms}-field measurement in section 6.1.2 with the TF predictions for the same exposure condition, equation 2.4.1 is modified, where z is the product of the tangential field and the TF

$$\Delta T = A\left|\int_l \vec{E}_{\tan}(l)\,\overrightarrow{TF}(l)\,dl\right|^2 = \tag{6.3.1}$$

$$A\left(\sum \vec{E}_{\tan}(l)\,\overrightarrow{TF}(l)\right)\left(\sum \vec{E}_{\tan}(l)\,\overrightarrow{TF}(l)\right)^* = A\mid z\mid^2$$

with 3.2.1 to

$$E \propto \mid z \mid . \tag{6.3.2}$$

For each calculated $\vec{E}_{\tan}(l)$ scalar multiplied by the $\overrightarrow{TF}(l)$, the programmed script returns one complex number z and thus for each exposure condition inside the phantom, as presented in Fig. 6.12. The modulus of this number should be proportional to the measured E_{rms}-field at the corresponding exposure condition. The E_{rms}-field calculated from the different $\overrightarrow{TF}$ and the measured E_{rms}-field are shown in Fig. 6.13 for 0°, 90°, 180° and 270°. A total of 6369 values are measured in about two hours. This set of exposure conditions is used as calibration data to scale the predicted E-field with the TF to the measurement conditions.

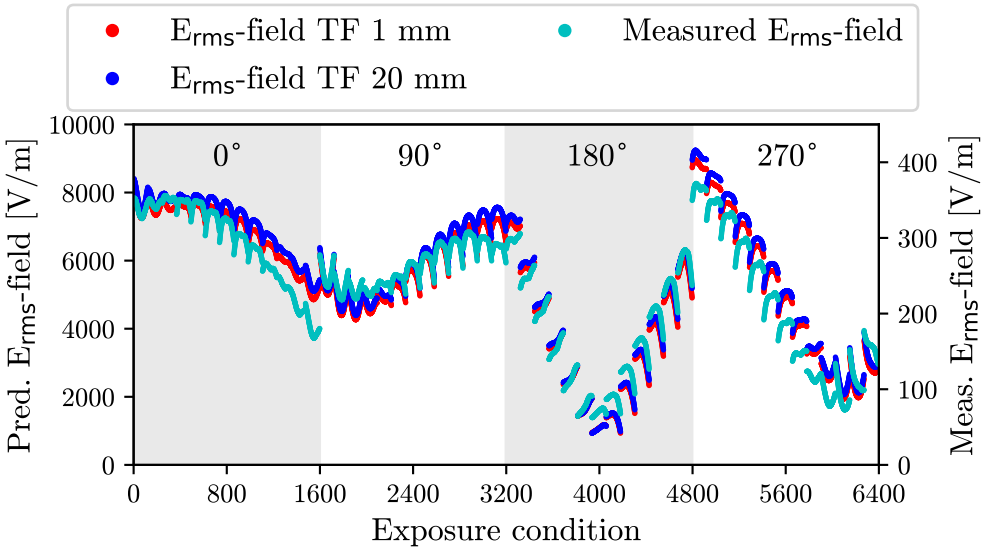

Figure 6.13: The comparison of the measured and transfer function predicted E_{rms}-field at the test object hot spot for each exposure condition of four polarizations for both transfer function resolutions.

The TF predictions and the measured E_{rms}-field are in reasonable agreement at first glance. To assess the accuracy with which the TF predicts the measured E_{rms}-field, they are compared against each other. There should be a linear correlation between the modulus of the TF predictions of the two $\overrightarrow{TF}$ and the measured E_{rms}-field, displayed in Fig. 6.14.
The linear regression is

$$y_i = A_{TF} x_i,$$

where y_i is the measured E_{rms}-field, x_i the predicted E_{rms}-field and A_{TF} the calibration factor. The A_{TF} and R^2, are listed in table 6.2 for both TFs. TF1 corresponds to the 20 mm resolution and TF2 corresponds to the 1 mm resolution, respectively.

Model	A_{TF}	R^2
TF1	0.04211 ± 0.00004	0.9432
TF2	0.04367 ± 0.00004	0.9453

Table 6.2: The calibration factor and R^2 calculated from the linear regression for each transfer function.

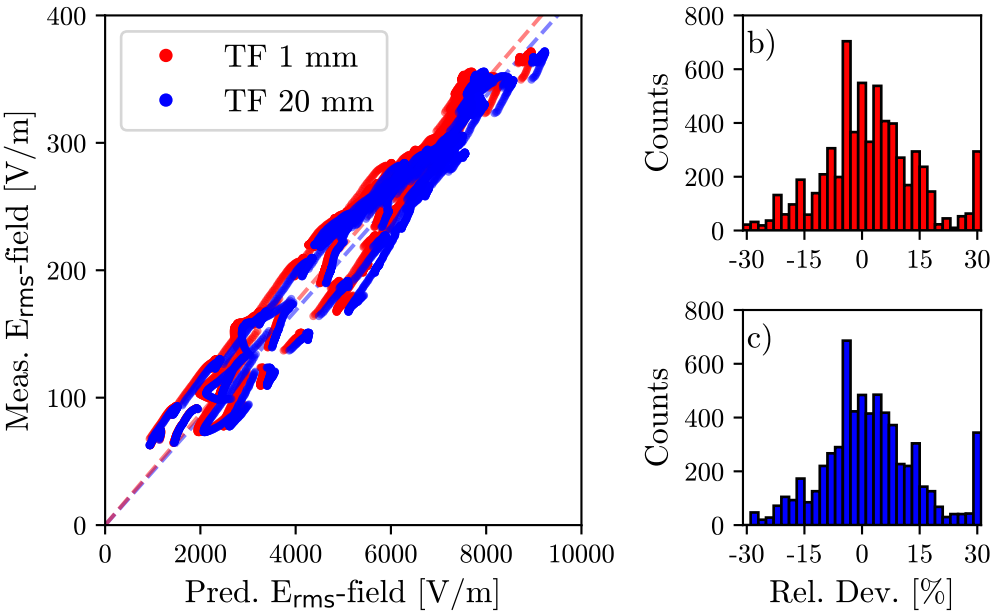

Figure 6.14: The correlation between the measured E_{rms}-field and the transfer function predicted E_{rms}-field at the hot spot for both transfer function resolutions, including the resulting linear regression lines and the relative deviation of the difference for TF2 in a) and TF1 in b).

The specific calibration factor A_{TF} is applied to the different predicted E_{rms}-field values per TF. The difference between the calibration factors is 3.69 %, which is less than the 3.72 % from section 6.2 and thus not significant.
The mean values and standard deviations for the relative difference between the measured E_{rms}-field compared to the calibrated TF predictions are listed in table 6.3.

Model	x[%]	σ[%]
TF1	3.02	14.80
TF2	2.98	14.32

Table 6.3: The mean value and its standard deviation of the relative difference of the measured E_{rms}-field compared to the transfer function predictions.

Table 6.2 and 6.3 show a strong linear correlation between the E_{rms}-field predictions of both TFs and the measured E_{rms}-field, and their standard deviation is in the same order of magnitude. Since TF2 has a slightly lower standard deviation, better correlation, and the same resolution as the numerical predictions, it is the most suitable TF for further investigation.

To validate the calibrated TF2, a second E_{rms}-field measurement is performed with additional exposure conditions $\vec{E}_{\tan}$. The calibration data covers the whole isoplane, measuring values at the closest and farthest proximity from the walls for four phase settings, as presented in Fig. 6.2. For the validation data, the same measurement setup is used, but the movement scheme is reduced and in return additional polarizations are applied to expose the test object to different exposure conditions than

for the calibration data. To investigate the influence of the distance of the TO from the phantom walls, two movement schemes are used, one with 20 mm distance and one with 50 mm from the phantom walls, as shown in Fig. 6.15. As demonstrated in section 4.3.2.1 and section 4.3.2.3, the deviation between different measurement days and between the predicted and measured incident E-field increases for the first and last 30 mm of the lines.

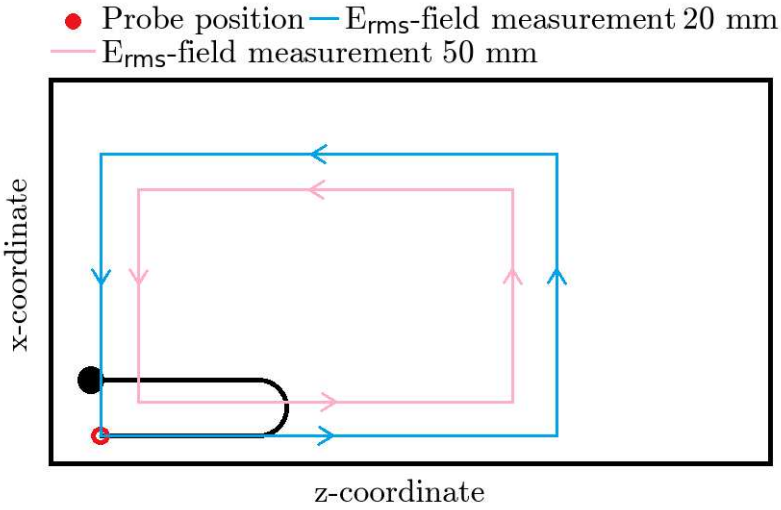

Figure 6.15: The schematic overview of the movement schemes for the validation data sets for 20 mm distance in blue and for 50 mm distance in purple of the test object to the closest phantom wall.

For the E_{rms}-field measurement, where the TO is moved with 20 mm distance from the phantom walls, a total of 8284 exposure conditions are measured in approximately three hours, including 19 polarizations between 0° and 180°. For the E_{rms}-field measurement with 50 mm distance, 8160 exposure conditions are measured in approximately three hours including 24 phase settings between 0° and 330°. In order to measure a similar number of exposure conditions for both validation sets, the number of polarizations is increased to compensate for the reduced number of positions.
The corresponding $\vec{E}_{\tan}$ is calculated accordingly and applied to the calibrated $\overrightarrow{TF2}$ for each exposure condition. The calibrated TF predictions are compared with the measured E_{rms}-field and a linear regression is performed. The slope of the resulting fit function should be $1 \pm a$, where a should be within the ± 0.0372 range. The results are presented in Fig. 6.16.
The scattering of the data points displays that the calibration data and the validation data from the 50 mm distance measurement are in good agreement. The slope for this data is 0.9782, which is within 1 ± 0.0372 and $R^2 = 0.9206$. In addition, the scattering of the data points in the correlation plot is similar to the scattering of the calibration data. The mean value and standard deviation of the relative difference of the measured E_{rms}-field compared to the TF prediction is $0.51 \pm 12.86\,\%$, which is in good agreement with the values in table 6.3.
The slope for the data at 20 mm distance is 0.9882, which is also within the requirement. However, the scattering of the values differs substantially from the calibration data and the R^2 is reduced to 0.8543. The mean value and standard deviation of

the relative difference of the measured E_{rms}-field compared to the TF prediction is $0.77 \pm 10.26\,\%$, which is less than for the calibration data. However, the scattering of the data at 20 mm distance is not symmetric, with less correlation than the calibration data and the data at 50 mm distance. Reflection effects have an influence, and also the fact that the deviation between the numerical predicted and measured incident E_{rms}-field in section 4.3.2.3 increases for the outer 50 mm, adds up to the difference between measured and predicted E_{rms}-field. Therefore, it is recommended to exclude the data at 20 mm distance for TF validation measurements in the LES.

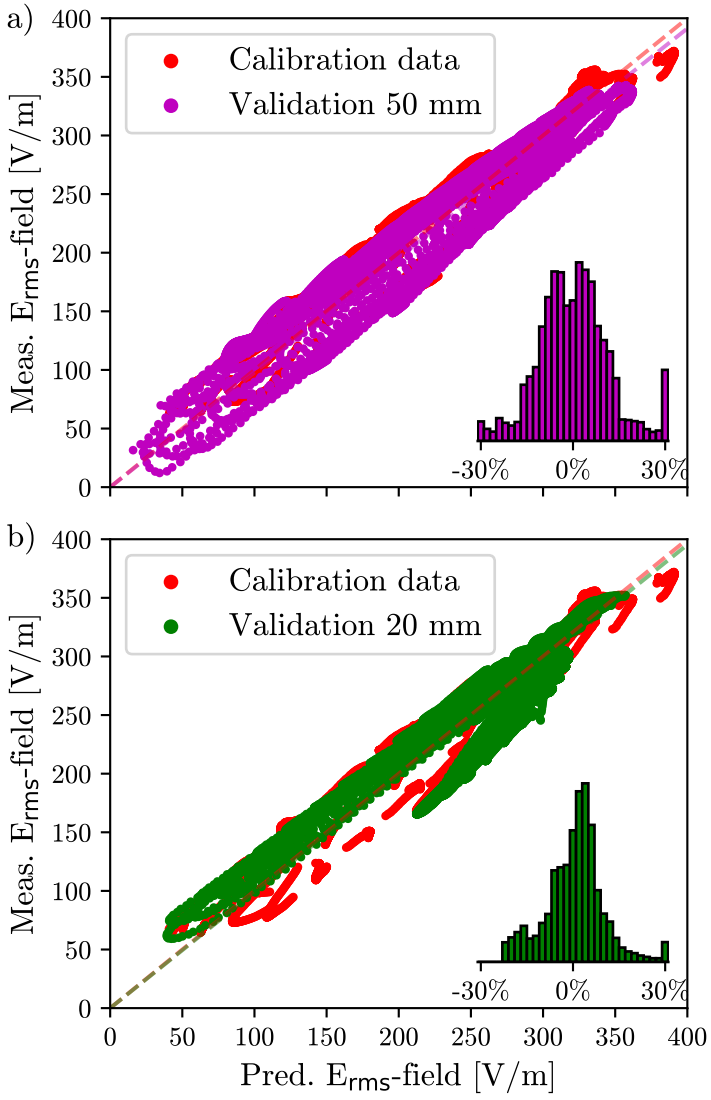

Figure 6.16: The comparison of the measured E_{rms}-field and the TF prediction of the calibration data set and a) the validation data set at 50 mm, including the histogram showing the relative deviation of the measured E_{rms}-field compared to the predicted E_{rms}-field and b) the validation at 20 mm distance to the phantom walls and its relative deviation histogram.

To evaluate the influence of the coupling between the channels on the correlation between the TF predictions and the measured E_{rms}-field, the regression is performed

per polarization for the validation data at 50 mm distance. Ideally, the coupling is negligible for all polarizations, resulting in a constant regression slope, but for this measurement the regression results of the slope differ substantially for each polarization. Thus, the coupling is not negligible and the interference between the signal of the channels is different for each polarization in terms of the transmitted and reflected signal per channel. The transmitted and reflected power are monitored by the oscilloscope, connected to the coupler after the amplifier and the amplifier itself. The transmitted and reflected power also varied during the measurement of the validation data at 50 mm of the four lines in Fig. 6.15 and over all polarizations, as presented in Fig. 6.17. Additionally, the regression slope per polarization is plotted on the second axis in Fig. 6.17. Since the oscilloscope logs the data over the measurement time, the positions of the slopes per polarization are recalculated to the corresponding measurement time.

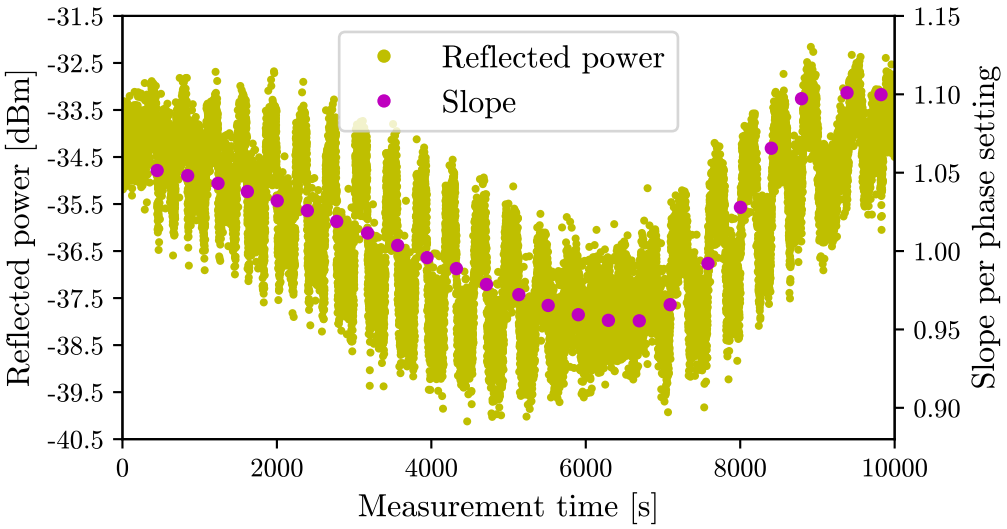

Figure 6.17: The comparison of the reflected power monitored by the oscilloscope and the slope of the linear regression between measured and predicted E_{rms}-field per polarization recalculated to the measurement time of the validation data set at 50 mm.

The slope of the regression between the measured E_{rms}-field and the predicted E_{rms}-field per polarization for the validation data at 50 mm and the reflected power behave similarly. The smaller the mean reflection per polarization, the smaller the slope of the regression between measured and predicted E_{rms}-field for that polarization. Although the reflected power varies by up to 3 dBm per polarization, the general pattern is comparable.
The coupling between the channels and the coupling between the TO and the antennas are responsible for the varying reflected and transmitted power for each polarization and position of the TO inside the phantom. The interference, and thus the change in transmit and reflected power, results in a different E_{rms}-field distribution inside the phantom, compared to the ideal case without coupling. The dependence of the coupling per polarization should also be visible in the oscilloscope data of the incident E_{rms}-field measurement, and the coupling between the TO and the antennas

should be visible between the measurement lines. Both cases are shown in Fig. 6.18. First, the transmitted and reflected power monitored by the oscilloscope during the incident E_{rms}-field measurement for five different polarizations in section 6.1.1 are presented, showing the coupling between the two channels. Second, the transmitted and reflected power monitored during the measurement of the four lines with the TO attached, displaying the coupling of the TO to the antennas, is shown for one exemplary polarization.

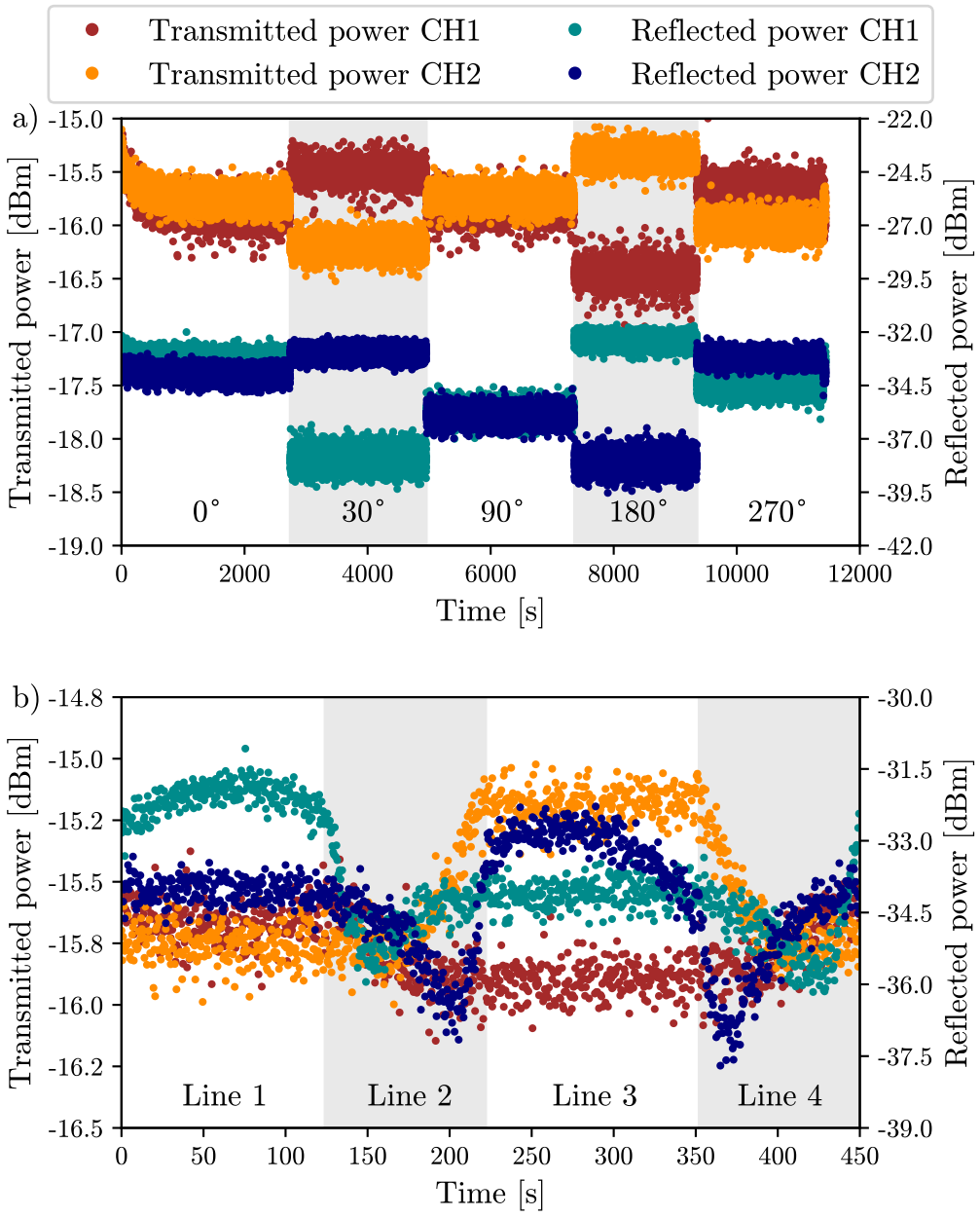

Figure 6.18: The monitored transmitted and reflected data per channel for the incident E_{rms}-field mapping for five polarizations in a) and the transmitted and reflected data for the four lines measured for one exemplary polarization of the validation data in b).

As expected, the transmitted and reflected power change drastically for different polarizations in Fig. 6.18a) and during the four line measurement with the TO in Fig. 6.18b). The coupling between the two channels can be described by the S-parameter S_{12}. The coupling between the channels, and thus the transmitted and reflected signals, changes per polarization. This is a physical effect that can potentially be reduced in two ways.

The first way is to readjust the amplitude at the FG to a fixed value for the transmitted power after changing the polarization. However, this method does not eliminate the variation in reflected power per polarization. The total reflection can be reduced by using an additional element in the signal line in Fig. 3.1. During the time of the measurements presented in this work, a circulator was developed as a bachelor thesis [64]. It is a device that redirects the reflected signal to a dummy load to protect the amplifiers and is specifically designed to stabilize the BC system.
In this case, the circulator is used to investigate whether the deviation of the difference between the measured E_{rms}-field and the predicted E_{rms}-field can be reduced by a modified measurement setup. The TO is fixed and placed for the mapping at 50 mm distance in Fig. 6.15.

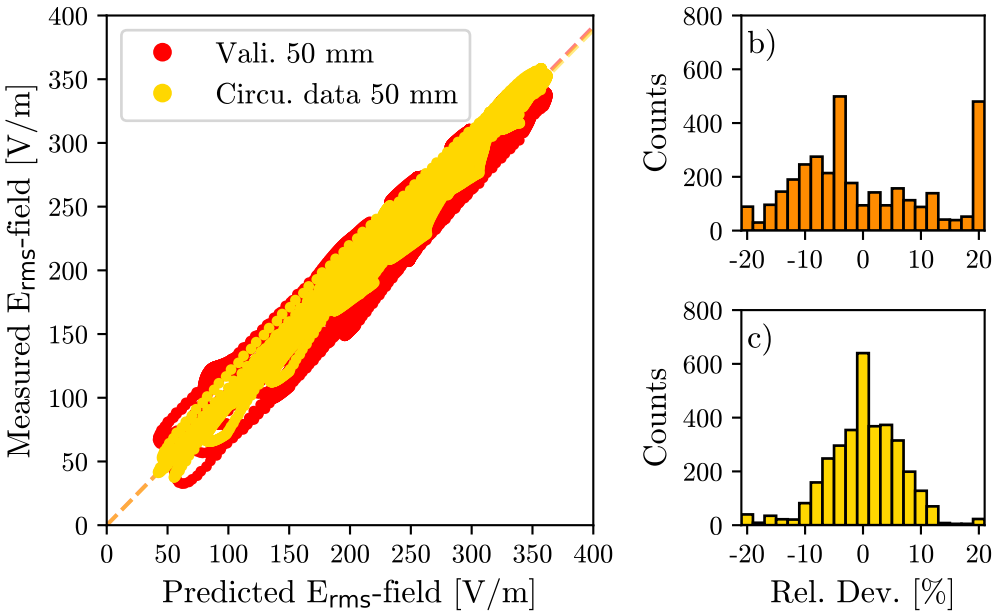

Figure 6.19: The correlation between the transfer function predictions and the measured E_{rms}-field of the validation data at 50 mm measured with and without the circulator connected to the power supply line and adjusting the input power to a stable transmit value in a), the relative deviation between the measured E_{rms}-field with and without circulator in b) and the deviation between the measured E_{rms}-field with the circulator compared to the predicted E_{rms}-field in c).

The number of polarizations is reduced to 10 (0°, 30°, 60°, 90°, 150°, 180°, 240°, 270°, 300°, 330°). The circulator is connected between the couplers and the LES, and the reflected power at the circulator is monitored by the oscilloscope. The am-

plitude at the FG is readjusted individually for each channel to a fixed transmit power. The measured E_{rms}-field at the lead tip at [50/45/90] is scaled to the same starting value as the validation data at 50 mm without the circulator, and thus the same E_{rms}-field probe distance, and compared to the E_{rms}-field measured without the readjustment of the amplitude and circulator, as presented in Fig. 6.16a). The mean value and the relative standard deviation of the measured E_{rms}-field without the circulator compared to the measured E_{rms}-field with the circulator and adjusted amplitude for the same polarizations is $-0.98 \pm 14.35\,\%$, as shown in Fig. 6.19b). The E_{rms}-field for both cases compared to the TF predictions are displayed in Fig. 6.19 for the ten polarizations, and the relative deviation of the measured E_{rms}-field with circulator compared to the predicted E_{rms}-field in Fig. 6.19c). The slope of the regression between the predicted E_{rms}-field and the measured E_{rms}-field with the circulator and amplitude adjustment is 0.9716, which is in agreement with the calibration data and the previous measurement at 50 mm distance. In addition, the scattering of the values around the regression line is reduced, resulting in a higher correlation with $R^2 = 0.9803$. The mean value and its standard deviation of the relative difference of the measured E_{rms}-field compared to the predicted E_{rms}-field is $0.26 \pm 6.59\,\%$. The standard deviation is reduced by half compared to the measurement without the circulator and readjustment. Therefore, the amplitude adjustment with respect to the transmitted power and the circulator reducing the reflected power drastically improve the agreement between the measured E_{rms}-field and the predicted E_{rms}-field.

The second way is to consider the coupling of the channels per polarization in the numerical predictions of the incident E_{rms}-fields. This would increase the agreement of the predicted incident E_{rms}-field with the actual incident E_{rms}-field measured inside the phantom. Due to the complexity of such numerical predictions, the channels are simulated individually and then added in a complex manner, resulting in the coupling being assumed to be negligible and therefore ideal.

The coupling between the TO and the antennas varies with the TO and cannot be avoided during the measurement and must be evaluated individually for each TO in the LES and with this approach. Depending on the strength of the coupling between the TO and the antennas, the minimum distance between them can be increased to reduce the coupling.

The overall uncertainty of the measurement and the individual factors are described and investigated in the next section, including the influence of the amount of data. The final evaluation of the suitability of this measurement approach with only one trajectory and fixed test object and E_{rms}-field probe is also discussed in the next section.

6.4 Uncertainty analysis

The ISO/TS describes possible sources of uncertainty and proposes to use the approach of ISO/TR 21900:2017 [65] to calculate the measurement uncertainties and the uncertainty of the TF. The uncertainty factors relevant for this analysis are listed in table 6.4. The total measurement uncertainty depends on the E_{rms}-field probe, the TSM, the RF exposure system, and the positioning of the TO. Most likely, the

distance between the E_{rms}-field probe and the TO and the agreement between the incident E_{rms}-field from the numerical predictions compared to the measured E_{rms}-field have the strongest influence on the overall measurement uncertainty. Assuming that the TF and the incident E_{rms}-field from the numerical predictions are ideal, all uncertainty factors contribute to the measurement uncertainty. The different sources and their values determined in the previous sections are listed in table 6.4. The combined uncertainty is calculated as the root square sum (rss) of all uncertainty factors.

Source of Uncertainty	Contributing factor	$\pm\sigma$ [%]
E_{rms}-field probe	Calibration	5.67
	Linearity	
	Isotropy	
	Distortion of the E-field	
	Noise level	
TSM	conductivity	5.00
	permittivity	5.00
RF exposure system	Correlation to simulation	9.46
TO positioning	Lead trajectory	1.92
	AIMD mounting fixture	
	Distortion of fixture material	
	Distortion by AIMD	
Combined uncertainty	rss	**13.25**
	Coupling Channels	14.35
Combined uncertainty	rss	**19.53**
	E_{rms}-field probe rearranging	11.14
Combined uncertainty	rss	**22.45**

Table 6.4: The systematic uncertainties of different sources contributing to the total uncertainty and the total uncertainty reduced due to elimination by measurement setup optimization.

The uncertainty of the E_{rms}-field probe itself is taken from the calibration sheet provided by the manufacturer. The values for the TSM conductivity and permittivity are estimated from the measurement at the beginning and the end of each measurement day. The uncertainties of the exposure system, the TO positioning and the coupling of the channels as well as the uncertainty due to rearranging the probe per exposure condition are calculated from the previously described measurements in section 6.1.3 and section 6.3. The influence of the coupling between channels and the rearranging of the probe and thus the distance between the probe and the TO are combined individually in order to emphasize the advantages of the presented measurement approach.
From table 6.4, the combined measurement uncertainty including all factors is 22.45 %. The ISO/TS suggests that the TF is considered validated, if the relative difference between the measured E_{rms}-field and the predicted E_{rms}-field is less than the combined total measurement uncertainty. A fixed distance between the measurement probe and the TO, as possible with the LES, reduces the measurement uncertainty to 19.53 %. In this case, the relative difference between the measured E_{rms}-field and the predicted E_{rms}-field is 14.32 %, which is less than 19.53 %. There-

fore, the validation criterion is fulfilled for this TO and this measurement approach is suitable for the TF validation procedure.

In addition, by including the circulator in the supply line of the LES and readjusting the amplitude to a stable transmit value, the measurement uncertainty is further reduced to 13.25 %. With this optimized measurement approach, the deviation of the relative difference between the measured and the predicted E_{rms}-field can be reduced to 6.59 %, which is also less than the 13.25 %. The uncertainty is reduced in terms of overall systematic measurement uncertainty and predictability of the TF, and in addition the total measurement time is reduced from several days to hours, validating the TF for thousands of exposure conditions instead of approximately 25. Even though only one TO trajectory is used, the amplification due to changing the position and changing the polarization is approximately 32.7. To ensure that this amplification is due to independent exposure conditions rather than similar tangential E-field distributions along the test object with varying amplitude, the correlation between the incident field at the lead tip position for each exposure condition is compared to the E-field measured at the tip with the test object in place, as shown in Fig. 6.20.

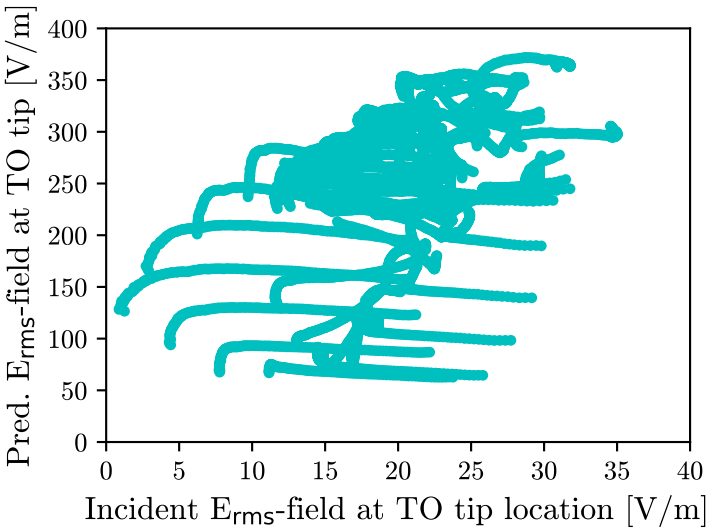

Figure 6.20: The correlation between the incident E_{rms}-field at the hot spot position without the object in place and the measured E_{rms}-field with the object in place at the same position.

The E_{rms}-fields show no correlation, with R^2=0.2178. Thus, the approach is successful in terms of generating a sufficient number of different independent exposure conditions.

To investigate the influence of the number of exposure conditions on the predictability of the TF, the bootstrap method is used. The ISO/TS approach for validating the TF suggests the use of approximately 25 different exposure conditions for the calibration and validation set. In the bootstrap approach, a sample is drawn with replacement from the population of the calibration data. In this case, the sample

size is 25 randomly drawn with replacement, representing any 25 exposure conditions used in the ISO/TS approach. For these 25 conditions, the correlation and regression with the TF predictions are calculated. This is done 20000 times for subsets out of the calibration data. This approach provides the standard error of the calibration factor and the standard deviation of the relative difference between the measured E_{rms}-field and the predicted E_{rms}-field using only 25 exposure conditions compared to thousands.
As listed in table 6.2, the calibration factor for TF2 is 0.04367 ± 0.00004 for the regression using 6396 exposure conditions. Using the bootstrap method, the mean calibration factor over all 20000 subsets of the size of 25 is still 0.04367, as expected. However, the standard error of the calibration factor as a fitting parameter for each subset increases by more than one order of magnitude to a mean value of 0.00071. Fig. 6.21 shows the histogram of the standard error of the calibration factor for all 20000 subsets.

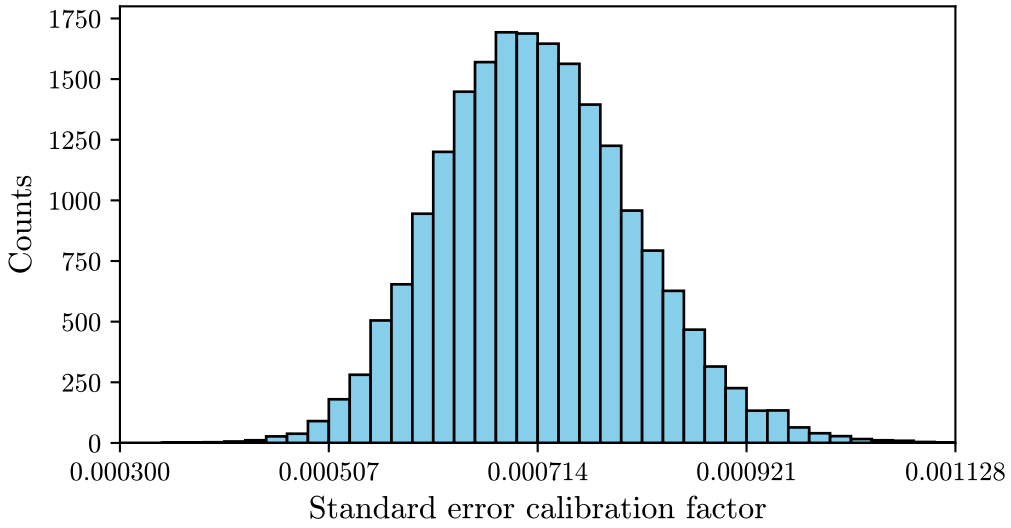

Figure 6.21: The standard error of the calibration factor calculated from the linear regression between the measured and predicted E_{rms}-field for 20000 data sets containing 25 data points.

The histogram demonstrates that the magnitude of the standard error of the calibration factor is at least one order of magnitude higher, due to the smaller sample size of 25 instead of using 6396 exposure conditions.
In addition, the standard deviation of the relative difference of the measured E_{rms}-field compared to the predicted E_{rms}-field is between 4.94 % and 25.08 %, depending on which 25 conditions are randomly chosen. The best and the worst case are displayed in Fig. 6.22. The scattering of the E_{rms}-field between measurement and prediction for the best case subset in green and for the worst case subset in red shows that, depending on the exposure conditions chosen, the predictability of the TF can be drastically over- or underestimated. Therefore, it is desirable to increase the number of exposure conditions to avoid an unreliable statement about the standard deviation and thus the predictability of the TF. In addition, a larger number of exposure conditions reduces the standard error of the calibration factor and thus the statistical uncertainty.

For the measurement part of the validation approach according to the ISO/TS, it is not practical to significantly increase the number of exposure conditions. The setup and accuracy required for each individual exposure condition is too time consuming. Increasing the number of measurable exposure conditions is only possible with the described approach within the LES, with a fixed distance between the E_{rms}-field probe and the TO. In the case, that the coupling between a TO and the antennas increases, a slightly reduced number of exposure conditions may be sufficient for a reliable statement. The distance between the TO and the antennas can be increased by excluding certain phantom areas. However, the measurement time for the calibration data is about two hours and for the validation data about three hours, which means that both measurements can be completed in one working day. Therefore, it may be more practical to measure the maximum number of positions and polarizations in the phantom volume, post-process the results to evaluate the extent of the coupling, and then exclude phantom regions. As demonstrated in section 4.3.2.3 and section 6.3 the minimum distance between any test object and the phantom walls should be increased to 50 mm.

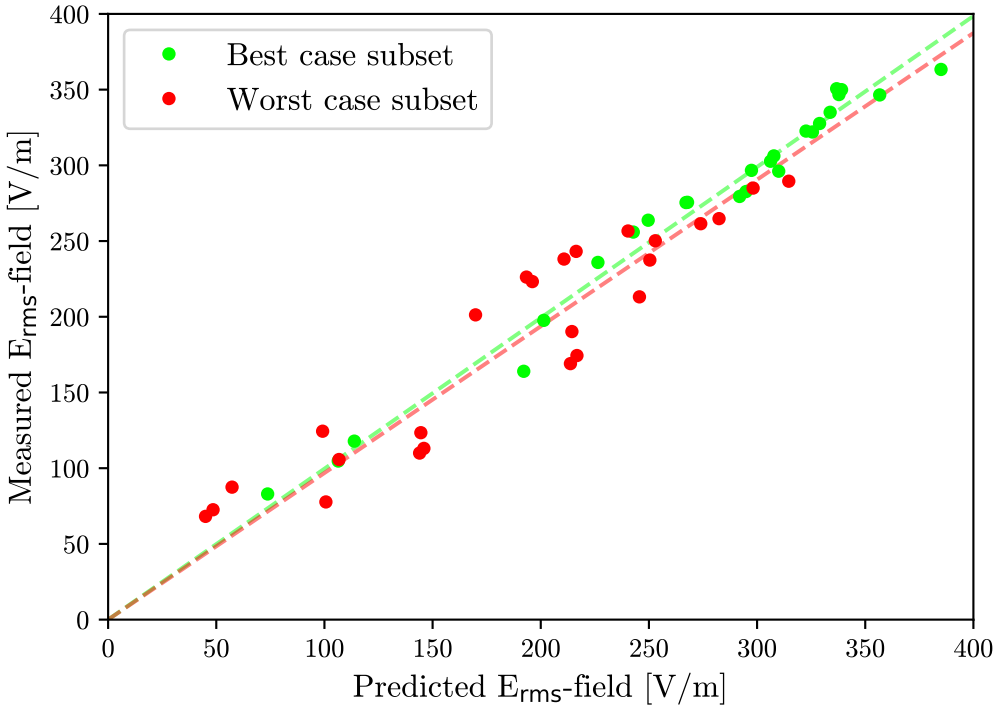

Figure 6.22: The correlation between the measured E_{rms}-field and the transfer function prediction for the data set with the best and worst scattering around the regression line.

Overall, this approach opens the possibility to measure many different exposure conditions in a short period of time, using only one trajectory and a fixed distance between the probe and the hot spot location of the TO. To ensure the best agreement between calibration and validation data, it is recommended to measure both data sets without rearranging the probe. With an optimal measurement setup, including the circulator and the readjustment of the input power per polarization, the total

measurement uncertainty is reduced by almost half, from 22.45 % to 13.25 %.
To fully predict of the power deposition within a hot spot, additional temperature measurements are required to scale the results from the E_{rms}-field probe to the position at closest proximity to the TO. These scaling factors will depend on the TO, but the E_{rms}-field probe should be placed as close to the TO as possible within the measuring range of the probe. The measurement of the calibration and validation data, including the measurement of temperature rise, can be accomplished with one setup and during one day.

6.5 Summary and discussion

This chapter discussed the novel measurement approach for transfer function validation of an active implant that is only possible with the LES. The current approach proposed by the ISO/TS, uses different trajectories and phantoms in the BC for TF validation. Once a TF is determined for a certain test object (active implant), it needs to be validated for a wide range of different tangential E-fields along the TO. To do this, the TO is exposed to a variety of E-field distributions and the temperature rise ΔT is measured. The ΔT is then compared to the results from the TF multiplied by the tangential E-field and integrated. If the measured ΔT and the calculated ΔT are in good agreement, the TF is validated and can be used to calculate the power deposition or temperature rise for any exposure condition occurring in a patient inside the MR scanner.
The validation procedure proposed by ISO/TS has some disadvantages. On the one hand, it is very time-consuming to mount the TO precisely in the desired trajectory. On the other hand, the setup and measurement probes are removed after each exposure condition, resulting in a different distance between the probe and the measurement position. This leads to a feasible number of exposure conditions of approximately 25 and increases the uncertainty of the measurement due to the steep gradient of the typical hot spot distribution.
In the LES, however, it is possible to mount the TO to a holder for one trajectory and fix it together with a measurement probe to a movement system. The whole complex can then be moved through the entire phantom to change the tangential E-field and thus the exposure conditions to which the TO is exposed to. To further modify the exposure conditions, the polarization is varied. This is only possible in the LES due to its accessibility and the channel independence, allowing the system to generate different independent E-field distributions within the phantom.
One of the advantages of this approach is that thousands of measurements with different exposure conditions can be performed in hours instead of days. In addition, the distance between the probe and the measurement location on the TO is fixed, eliminating a dominant uncertainty factor.
To validate this measurement approach, several measurement series were performed. It is shown, that the exposure conditions fulfill the requirements of diversity and the dynamic range. The amplification between the smallest and the largest measured value is approximately 32.7, as demonstrated in section 6.1.2. Additionally, a linear correlation between the squared results of the E_{rms}-field probe and the data from the temperature probe is demonstrated in section 6.1.2, allowing the use of the E_{rms}-field probe for the validation measurements. With the E_{rms}-field probe, the measurement can be further accelerated and saline solution can be used as the TSM, making the

probe and TO visible at all times. Only a few temperature measurements are required, to scale the measured E_{rms}-field value to the maximum temperature rise at closest proximity of the TO.
There is a good agreement between the measured incident E-field and the E-field of the numerical predictions for several polarizations within $\pm 9.46\,\%$ deviation. The agreement between them is directly related to the predictability of the TF. In addition, the measured E_{rms}-field at the TO does not vary substantially for different measurement days and different TO holders, resulting in repeatable measurements within $\pm 1.92\,\%$ deviation in section 6.1.2. The influence of rearranging the probe for each exposure condition compared to a fixed probe is investigated and the rearranging adds an uncertainty factor of $\pm 11.14\,\%$, as presented in section 6.1.3.
A TO with a known TF is used for the validation measurement. One set of 6369 exposure conditions measured in approximately two hours is used as calibration data, and a second set of 8160 exposure conditions measured in approximately three hours is used as validation data. Two different validation data sets were tested, varying in the distance of the TO to the phantom wall. From the corresponding data sets in section 6.3, it can be concluded that a distance of 20 mm to the wall is not suitable for the LES. The agreement between the measured and numerically predicted E-field is worse for these locations and reflection effects and the coupling between the TO and the antennas increases. Therefore, a minimum distance of 50 mm is recommended for the LES.
The agreement between the measured and predicted E_{rms}-field is within $\pm 14.32\,\%$ for the calibration and validation data and the combined measurement uncertainty is $19.53\,\%$, in the case of the fixed measurement probe. Since the deviation of the relative difference between the measured and predicted E_{rms}-field is less than the combined measurement uncertainty, the measurement approach with one trajectory, a fixed distance between the probe and the TO and using the E-field probe is considered as validated.
As a next step, it was investigated whether the uncertainty of the measurement approach can be further reduced by optimizing the measurement setup. Therefore, the TF prediction is compared with the measured E_{rms}-field for each polarization individually. It is observed that the slope per polarization and the reflected signal, monitored by an oscilloscope, show proportional behavior. This is due to the fact that the coupling between the channels causes interference, which changes the reflected signal and thus the E-field distribution inside the phantom. To partially avoid this effect, a circulator is connected to the supply line of the LES, which suppresses the reflected signal to stabilize the measurement. In addition, the input power at the function generator is readjusted to a stable transmit value per polarization.
These measurement optimizations reduce the combined measurement uncertainty to $\pm 13.25\,\%$ and improve the agreement between the measured and predicted E_{rms}-field to $\pm 6.59\,\%$. Overall, the measurement uncertainty is significantly reduced by half.
Finally, the difference between a data set of 25 exposure conditions and the calibration data set of 6369 exposure conditions was investigated. It is shown, that the standard error of the calibration factor increases by more than one order of magnitude for 25 exposure conditions. Depending on the choice of the 25 conditions, the agreement between the measured and predicted E_{rms}-field is between $4.94\,\%$ and $25.08\,\%$. Thus, it is feasible to validate the TF for as many exposure conditions as possible in order to increase the prediction accuracy of the TF.
The novel measurement approach allows a large number of exposure conditions to

be measured in a short period of time with systematic uncertainties reduced by half and statistical uncertainties reduced by one order of magnitude. The flexibility of the LES to generate different E-field distributions allows individual adaptation to any active implant whose TF needs to be validated.

7 Conclusion and Outlook

In this work, the current test procedures to asses the temperature rise ΔT that may occur at an implant due to RF-induced heating during an MR examination are evaluated and optimizations are suggested. The current methods suggested in Ref. [3] for passive implants and in Ref. [4] for active implants were investigated. Up to now, these test procedures are limited to the use of MR scanners or stand-alone BCs as RF exposure systems. Although it seems intuitive to use an MR scanner to test implants for their MR safety, these RF coils are not optimized for this type of testing. Since the goal of the RF coils is to generate a homogeneous magnetic field for a high image quality, and because the RF-induced heating depends on the electric field, generated by the time-varying magnetic RF field, these systems have several disadvantages.

First, the space inside the bore is limited and its accessibility is reduced. Measurement setups consisting of a phantom, a tissue simulating medium, the test object (TO), and measurement probes must be assembled outside the coil and moved to the desired measurement position. In addition, the placement of the components is restricted. But more importantly, the E-field distribution inside the filled phantom is not optimized for the test requirements. For passive implants, a homogeneous tangential incident E-field over the entire implant volume is required. The measured ΔT at the hot spot for a given implant is scaled to the square of the mean incident field and then rescaled to the E-field occurring in a patient at the implantation volume. Therefore, it is essential to measure the highest possible ΔT for a given mean incident field to ensure that the ΔT prediction inside the patient is not underestimated.

Since there is only a small volume where the distribution inside a BC generates a homogeneous tangential incident field, the distribution can vary within $\pm 1\,\mathrm{dB}$, increasing the measurement uncertainty of the measured ΔT.

For active implants, the test procedure is more complicated. A TF must be determined and validated for the TO. The validated TF is then able to transfer any realistic E-field distribution along the TO in the implantation volume into a ΔT at the hot spot. The validation measurement within a BC is very time consuming. A total number of approximately 25 different exposure conditions and thus tangential E-fields along the TO are required. For each exposure condition, the TO must be placed with high accuracy inside the phantom in the desired shape. A temperature probe must be placed at the hot spot, the phantom is filled with gelled medium, and the filled phantom has to be moved inside the coil. After the measurement, everything has to be removed out of the system and the phantom and the setup for the next exposure condition is assembled. Each exposure condition takes about one hour, so the validation measurement is spread over several days. There are a lot of measurement uncertainty factors, that need to be considered for this measurement procedure. One of the main factors is the distance between the probe and the hot spot, which is slightly different for each exposure condition. In addition, the TO must be placed exactly in the desired shape. Once all components are as-

sembled, the whole setup has to be moved, making the setup susceptible to small movements. It is not feasible to measure one exposure condition more than once due to the long measurement time, so there are no statistics for the individual exposure conditions.

Due to all these disadvantages, the need for a different exposure system that focuses on the requirements of both test procedures is high. In this work, an alternative two-channel linear dipole-based open RF exposure system has been comprehensively validated and its potential for both test procedures has been investigated. The goal of this system is to generate a uniform E-field over a large volume inside the medium filled phantom. During the validation, it was tested for stability, linearity, repeatability, and its E-field distribution in amplitude and phase of the main component and the combined fields for different polarizations. The measured E-field was compared with the numerically predicted E-field from the manufacturer for each individual channel and for different combined polarizations. The results of the stability and linearity measurements led to general recommendations of a warm-up time of approximately 15 minutes prior to measurements and an input power of less than $-7\,\mathrm{dBm}$. The day to day repeatability of the E-field distribution is validated and both channels operate symmetrically. The agreement between the measured and the numerically predicted incident E-field distribution for the polarizations of 0° and 180° is sufficient and the z-component is confirmed as the main component contributing to the total E-field. Finally, the LES was validated using the recommended approach of Ref. [4], using a standard TO to measure the ΔT per incident field.

It was shown, that the LES generates polarization dependent E-field distributions with large variety. Sufficiently large volumes of homogeneous E-fields can be generated for elongated and 3D extended test objects using different polarization settings. The influence of the incident E-field homogeneity and direction on the resulting ΔT at the hot spot of a TO was investigated for elongated objects and 3D extended objects. Both object groups were placed inside the BC and inside the LES and the ΔT was measured according to Ref. [3]. It was discovered that the measured ΔT for all tested TOs was significantly higher inside the LES compared to the BC, even in cases where the homogeneity requirement of $\pm 1\,\mathrm{dB}$ was fulfilled. Therefore, it is not possible to adequately estimate the patient risk with the BC. The difference in ΔT scaled to the square of the mean incident E-field over the TO volume between the systems was approximately $4-12\,\%$ for the elongated objects and $14-24\,\%$ for the 3D extended objects. In addition, a misplacement of the TO in both x-directions results in a ΔT difference of approximately $5\,\%$ for the BC, while there was no significant difference in ΔT for the LES. The general underestimation of the ΔT per incident field of the BC may lead to a patient risk that should be avoided in any case. With the LES E-field distribution, which represents a possible worst-case ΔT, this risk can be drastically reduced.
For both systems, an amplitude readjustment to a stable E-field value during the measurement time at a reference position is recommended and was included in all temperature measurements. The current standard approach does not include this readjustment, which increases the measurement uncertainties.

Furthermore, the accessibility of the LES and its independent channels, offer the possibility to use a simplified and faster approach for the validation measurements of the TF of an active implant. It is possible to fix the TO and the measurement probe simultaneously to a movement system. This whole complex can be moved

through the entire phantom and additionally the polarization can be changed to generate a large number of different exposure conditions.
This measurement approach was validated on a standard TO with a known TF. It was shown that the LES generates a sufficient variety of tangential E-fields along the TO and that the validation measurement could be performed with an E-field probe instead of a temperature probe. With a fixed distance between the measurement probe and the TO for all exposure conditions, one of the dominant measurement uncertainty factors of approximately $\pm 11\,\%$ was eliminated. By adding a circulator in the supply line and readjusting the amplitude, the coupling between the channels was reduced. This not only improves the overall measurement uncertainty, but also the agreement between the generated and numerically predicted incident E-field per polarization.
The measurement uncertainty without any optimization and without a fixed distance between the measurement probe and the TO was about $\pm 22\,\%$. The mentioned optimizations reduce this measurement uncertainty by half to about $\pm 12\,\%$.
To accept a TF as validated, the standard deviation of the relative difference between the measured E-field and the E-field calculated from the TF, should be less than the measurement uncertainty, which is achieved by the optimized case.
This novel measurement approach not only reduces the measurement uncertainty and the uncertainty of the predictability of the TF by half, but also drastically reduces the measurement time. With the novel approach, 6000 to 8000 exposure conditions can be measured in approximately three hours instead of measuring 25 exposure conditions over several days, reducing not only the time, but also the necessary resources and costs.

In general, the LES offers various possibilities to optimize both measurement procedures for passive and active implants and to reduce the uncertainties of the estimated temperature rise ΔT inside a patient. In the future, the LES could be used to generate an individual tangential field along a passive implant to ensure worst-case conditions.
In addition, an automation could be implanted for TF validation to provide the most appropriate TO trajectory, including its positions within the phantom and the polarizations, resulting in the greatest variety of tangential E-fields along the TO and thus exposure conditions.
To complete the general measurement capabilities, other similar LES are under development for other frequencies, e.g. 128 MHz and 299 MHz, corresponding to a magnetic field strengths of 3 T and 7 T. With a set of different LES, the BCs for the different frequencies could be completely replaced and one TO could be tested faster and with less uncertainty for the common frequencies of the available MR scanners in daily clinical practice.

A Appendix

A.1 Numerical predicted incident E-field

The E-field distributions in amplitude and phase for the x-, y- and z-components and the combined E-field are calculated from the numerical predictions provided by ING Gao for channel 1 (CH1), Fig. A.1, channel 2 (CH2), Fig. A.2 and the channel combination of 0° phase difference, Fig. A.3.

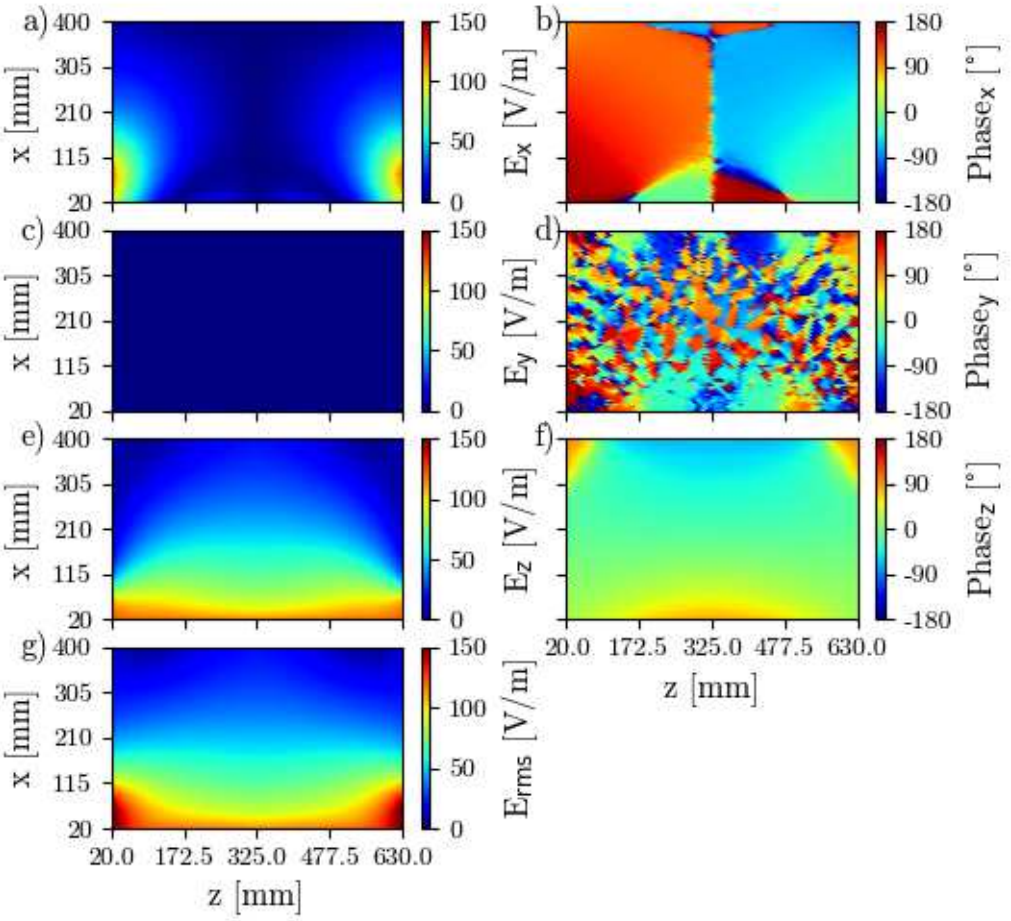

Figure A.1: The numerical predicted total E_{rms}-field distribution and the tangential E_{rms}-field distribution for all three components in amplitude in a) E_x, b) E_y, c) E_z and phase in b) Phase$_x$, d) Phase$_y$, f) Phase$_z$ and in g) the total E-field for channel 1.

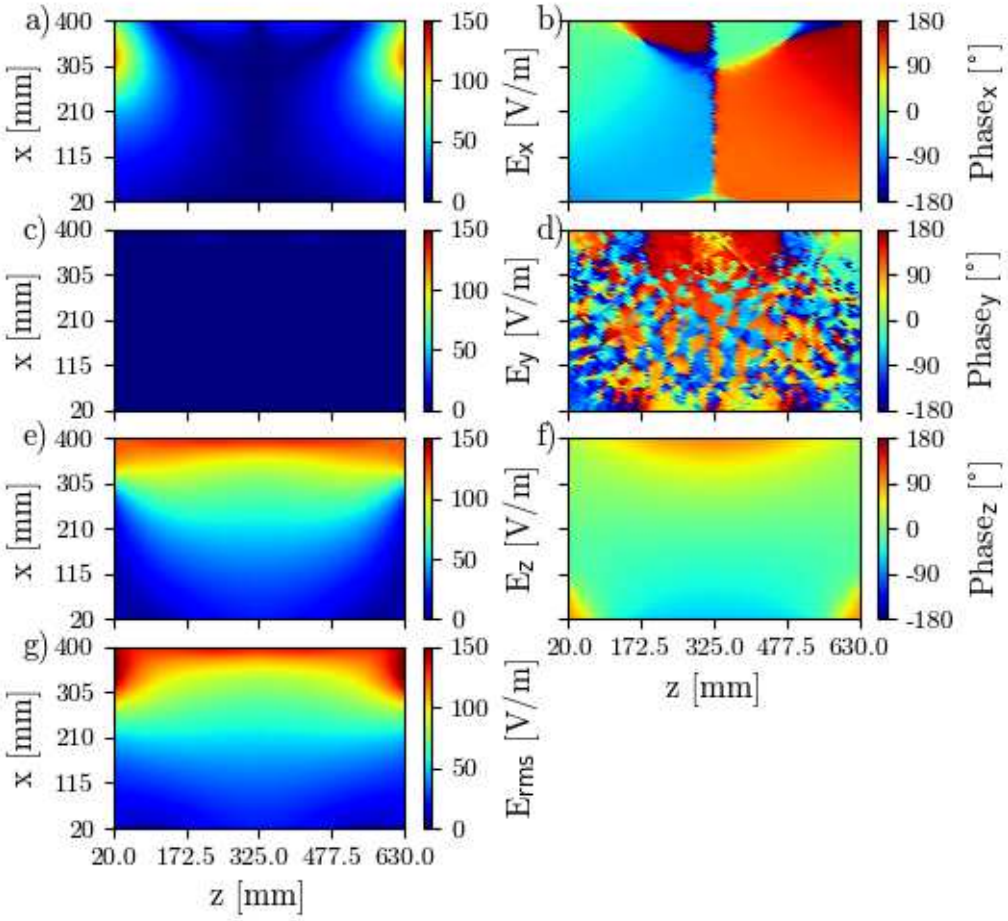

Figure A.2: The numerical predicted total E_{rms}-field distribution and the tangential E_{rms}-field distribution for all three components in amplitude in a) E_x, b) E_y, c) E_z and phase in b) Phase$_x$, d) Phase$_y$, f) Phase$_z$ and in g) the total E-field for channel 2.

The E-field distributions show a symmetric behavior and the y-component for both channels and the combination at 0° is negligible. The z-component is the dominant component in all cases. The amplitude increases near the end plates of the antennas and decreases towards the phantom center.
The phase distribution is smooth for the z-component, negligible for the y-component and smooth with a few phase jumps for the x-component.

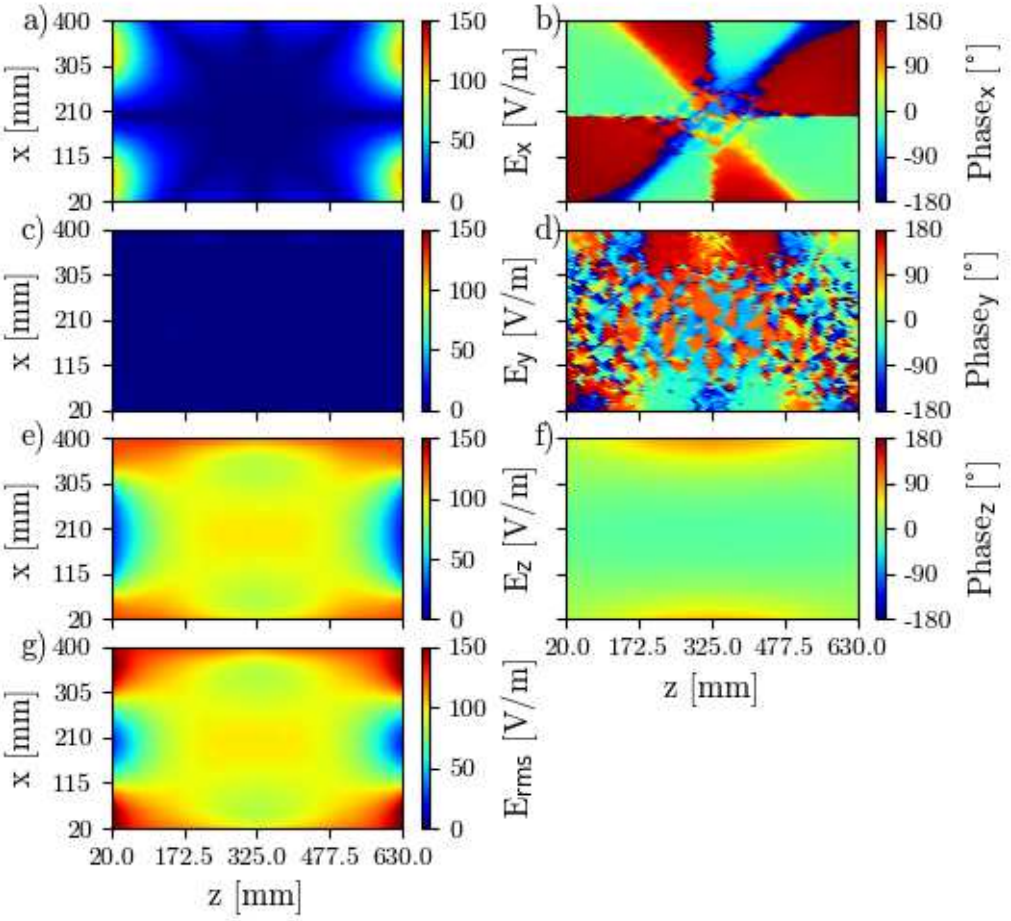

Figure A.3: The numerical predicted total E_{rms}-field distribution and the tangential E_{rms}-field distribution for all three components in amplitude in a) E_x, b) E_y, c) E_z and phase in b) Phase$_x$, d) Phase$_y$, f) Phase$_z$ and in g) the total E-field for 0° phase difference between the channels.

A.2 Transfer function predictions

To calculate the tangential E-field along the U-shaped trajectory of the test object, SAIMD-U, the trajectory is transformed into one matrix for the x-component and one for the z-component containing the normalized tangential component of the E-field. The matrices U_x and U_z are displayed in Fig. A.4. The hot spot is located at [0/0] of the matrix and the first straight part is aligned with the z-component, resulting in +1 entries in the matrix U_z and 0 entries in U_x. At the turning point $U_z = 0$ and $U_x = 1$ represents the case where the the trajectory is aligned with the x-component of the E-field.

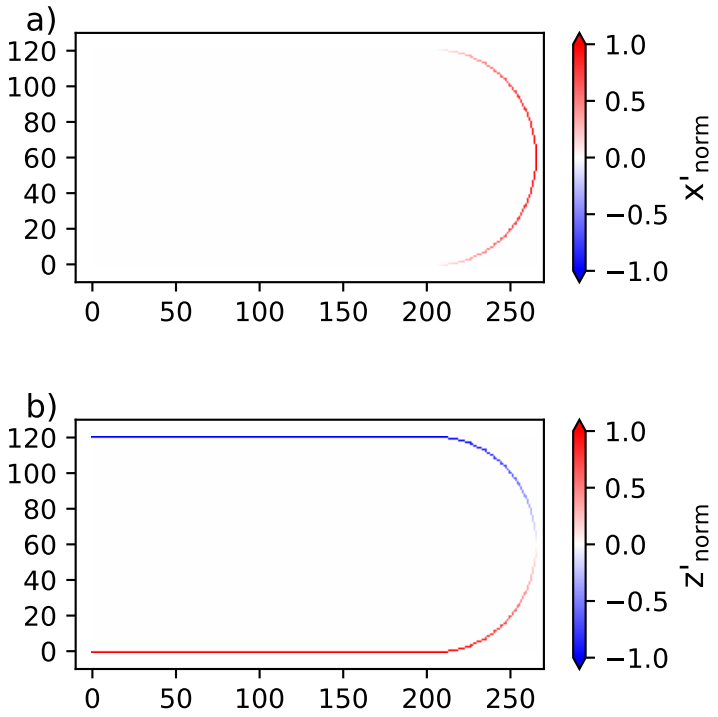

Figure A.4: U-shaped trajectory transferred into 121x266 matrices for the normalized first derivation of the x-component in a) and the z-component in b), where [0/0] is the lead tip and therefore the hot spot position.

Bibliography

[1] A. Wengler, U. Nimptsch, and T. Mansky, "Hip and knee replacement in Germany and the USA analysis of individual inpatient data from german and US hospitals for the years 2005 to 2011," *Dtsch Arztebl Int.*, Jun. 2014, 111(23-24):407-16.

[2] Statista. Orthopedic Devices - Germany, accessed on 18-03-2025. [Online]. Available: https://www.statista.com/outlook/hmo/medical-technology/medical-devices/orthopedic-devices/germany

[3] *ASTM F2182-19e2 - Standard Test Method for Measurement of Radio Frequency Induced Heating On or Near Passive Implants During Magnetic Resonance Imaging*, American Society for Testing and Materials Std., 2019.

[4] *ISO/TS 10974:2018 - Assessment of the safety of magnetic resonance imaging for patients with an active implantable device*, International Organization for Standardization Std., 2018.

[5] *Testing and Labeling Medical Devices for Safety in the Magnetic Resonance (MR) Environment*, U.S. Department of Health and Human Services Food and Drug Administration Std., 2023.

[6] F. Ketelsen, J. Kreutner, and G. Schaefers, "Validity of radial symmetric hotspot distribution around a lead for comparison of differentprobe types at various orientations to a lead," *ISMRM Workshop on MR Safety 2019*, 2019.

[7] "ESMRMB 2019 36th Annual Scientific Meeting, Rotterdam, NL, October 3-October 5: Abstracts, Friday," *Magnetic Resonance Materials in Physics, Biology and Medicine*, vol. 32, no. 1, pp. 107–233, 2019. [Online]. Available: https://doi.org/10.1007/s10334-019-00754-2

[8] F. Ketelsen, J. Kreutner, G. Schaefers *et al.*, "Approach to reduce the measurement volume to determine spatial distribution of power deposition around a straight lead according to ISO/TS 10974," *ISMRM and SMRT Virtual Conference and Exhibition, Proc. Intl. Soc. Mag. Reson. Med. 28 (2020)*, 2020.

[9] F. Ketelsen, K. Kröninger, and G. Schaefers, "Validation of a new 64MHz RF exposure system for testing medical implants for RF-induced heating according to ASTM-F2182 and ISO/TS 10974," *ISMRM and SMRT Annual Meeting and Exhibition, Proc. Intl. Soc. Mag. Reson. Med. 29 (2021)*, 2021.

[10] F. Ketelsen, V. Hammersen, G. Schaefers *et al.*, "Influence of E-field homogeneity and drift for testing medical implants for RF-induced heating at 64MHz according to ASTM-F2182 and ISO/TS 10974," *ISMRM and SMRT Annual Meeting and Exhibition, Proc. Intl. Soc. Mag. Reson. Med. 29 (2021)*, 2021.

[11] V. Hammersen, F. Ketelsen, A. Rennings *et al.*, "Numerical simulation study on the effects of intentionally inhomogeneous E-field distributions on RF-induced heating of implants," *ISMRM and SMRT Annual Meeting and Exhibition, Proc. Intl. Soc. Mag. Reson. Med. 29 (2021)*, 2021.

[12] F. Ketelsen, H. Gao, and G. Schaefers, "Validation of a novel 128MHz dual channel dipole-based RF exposure system to test medical implants for RF-induced heating according to ASTM-F2182 and ISO/TS 10974," *ISMRM Workshop on MR Safety, 2022*, 2022.

[13] F. Ketelsen and G. Schaefers, "New system, new approach: Fasten up transfer function validation measurements, prove of concept," *ISMRM and ISMRT Annual Meeting and Exhibition, Proc. Intl. Soc. Mag. Reson. Med. 31 (2023)*, 2023.

[14] F. Ketelsen, Y. Zhang, and G. Schaefers, "Evaluation of a dipole-based RF exposure system for testing RF-induced heating of passive implants at 64 MHz," *will be submitted*.

[15] R. E. Watson and L. Yu, "Safety considerations in MRI and CT," *Neuroimaging*, vol. 29, no. 1, pp. 27–53, Feb. 2023.

[16] O. Dössel, *Bildgebende Verfahren in der Medizin*, 2nd ed. Springer Vieweg Berlin, Heidelberg, 2016.

[17] D. Weishaupt, V. D. Köchli, and B. Marincek, *Wie funktioniert MRI?*, 7th ed. Springer Berlin, Heidelberg, 2013.

[18] R. B. Buxton, "The physics of functional magnetic resonance imaging (fMRI)," *Reports on Progress in Physics*, vol. 76, no. 9, p. 096601, sep 2013. [Online]. Available: https://dx.doi.org/10.1088/0034-4885/76/9/096601

[19] J. C. Gore, "Principles and practice of functional MRI of the human brain," *The Journal of Clinical Investigation*, vol. 112, no. 1, pp. 4–9, 7 2003. [Online]. Available: https://www.jci.org/articles/view/19010

[20] D. Hao, T. Ai, F. Goerner *et al.*, "MRI contrast agents: Basic chemistry and safety," *Journal of Magnetic Resonance Imaging*, vol. 36, no. 5, pp. 1060–1071, 2012. [Online]. Available: https://onlinelibrary.wiley.com/doi/abs/10.1002/jmri.23725

[21] F. Iacobellis, M. Di Serafino, C. Russo *et al.*, "Safe and informed use of gadolinium-based contrast agent in body magnetic resonance imaging: Where we were and where we are," *Journal of Clinical Medicine*, vol. 13, no. 8, 2024. [Online]. Available: https://www.mdpi.com/2077-0383/13/8/2193

[22] M. M. Chaumeil, J. A. Bankson, K. M. Brindle *et al.*, "New horizons in hyperpolarized 13C MRI," *Molecular Imaging and Biology*, vol. 26, no. 2, pp. 222–232, 2024. [Online]. Available: https://doi.org/10.1007/s11307-023-01888-5

[23] S. Jørgensen, N. Bøgh, E. Hansen *et al.*, "Hyperpolarized MRI – an update and future perspectives," *Seminars in Nuclear Medicine*, vol. 52, no. 3, pp. 374–381, 2022, advancement in Instrumentation for Molecular

Imaging. [Online]. Available: https://www.sciencedirect.com/science/article/pii/S0001299821000787

[24] J. M. Henderson, J. Tkach, M. Phillips *et al.*, "Permanent neurological deficit related to magnetic resonance imaging in a patient with implanted deep brain stimulation electrodes for parkinson's disease: Case report," *Neurosurgery*, vol. 57, Nov. 2005.

[25] *Safety Guidelines for Magnetic Resonance Imaging Equipment in Clinical Use 2022*, MHRA Medicines and Healthcare products Regulatory Agency Std., 2022.

[26] P. Davis, L. Crooks, M. Arakawa *et al.*, "Potential hazards in NMR imaging: heating effects of changing magnetic fields and RF fields on small metallic implants," *American Journal of Roentgenology*, vol. 137, no. 4, pp. 857–860, 1981, pMID: 6974985. [Online]. Available: https://doi.org/10.2214/ajr.137.4.857

[27] L. Winter, F. Seifert, L. Zilberti *et al.*, "MRI-related heating of implants and devices: A review," *Journal of Magnetic Resonance Imaging*, vol. 53, no. 6, pp. 1646–1665, 2021. [Online]. Available: https://onlinelibrary.wiley.com/doi/abs/10.1002/jmri.27194

[28] H. S. Ho, "Safety of metallic implants in magnetic resonance imaging," *Journal of Magnetic Resonance Imaging*, vol. 14, no. 4, pp. 472–477, 2001. [Online]. Available: https://onlinelibrary.wiley.com/doi/abs/10.1002/jmri.1209

[29] F. G. Shellock, "Radiofrequency energy-induced heating during MR procedures: A review," *Journal of Magnetic Resonance Imaging*, vol. 12, no. 1, pp. 30–36, 2000. [Online]. Available: https://onlinelibrary.wiley.com/doi/abs/10.1002/1522-2586%28200007%2912%3A1%3C30%3A%3AAID-JMRI4%3E3.0.CO%3B2-S

[30] T. Sommer, C. Vahlhaus, G. Lauck *et al.*, "MR imaging and cardiac pacemakers: In vitro evaluation and in vivo studies in 51 patients at 0.5 T," *Radiology*, vol. 215, no. 3, pp. 869–879, 2000, pMID: 10831713. [Online]. Available: https://doi.org/10.1148/radiology.215.3.r00jn08869

[31] J. Nyenhuis, S.-M. Park, R. Kamondetdacha *et al.*, "MRI and implanted medical devices: basic interactions with an emphasis on heating," *IEEE Transactions on Device and Materials Reliability*, vol. 5, no. 3, pp. 467–480, 2005.

[32] S.-M. Park, R. Kamondetdacha, A. Amjad *et al.*, "MRI safety: RF-induced heating near straight wires," *IEEE Transactions on Magnetics*, vol. 41, no. 10, pp. 4197–4199, 2005.

[33] P. Nordbeck, F. Fidler, I. Weiss *et al.*, "Spatial distribution of RF-induced E-fields and implant heating in MRI," *Magnetic Resonance in Medicine*, vol. 60, no. 2, pp. 312–319, 2008. [Online]. Available: https://onlinelibrary.wiley.com/doi/abs/10.1002/mrm.21475

[34] E. Mattei, M. Triventi, G. Calcagnini *et al.*, "Complexity of MRI induced heating on metallic leads: experimental measurements of 374 configurations," *Biomedical engineering online*, vol. 7, Mar. 2008.

[35] E. Neufeld, S. Kühn, G. Szekely *et al.*, "Measurement, simulation and uncertainty assessment of implant heating during MRI," *Physics in Medicine and Biology*, vol. 54, no. 13, pp. 4151–4169, jun 2009. [Online]. Available: https://doi.org/10.1088/0031-9155/54/13/012

[36] T. Song, Z. Xu, M. I. Iacono *et al.*, "Retrospective analysis of RF heating measurements of passive medical implants," *Magnetic Resonance in Medicine*, vol. 80, no. 6, pp. 2726–2730, 2018. [Online]. Available: https://onlinelibrary.wiley.com/doi/abs/10.1002/mrm.27346

[37] A. Yao, M. Murbach, T. Goren *et al.*, "Induced radiofrequency fields in patients undergoing MR examinations: insights for risk assessment," *Physics in Medicine & Biology*, vol. 66, no. 18, p. 185014, sep 2021. [Online]. Available: https://doi.org/10.1088/1361-6560/ac212d

[38] A. Yao, T. Goren, T. Samaras *et al.*, "Radiofrequency-induced heating of broken and abandoned implant leads during magnetic resonance examinations," *Magnetic Resonance in Medicine*, vol. 86, no. 4, pp. 2156–2164, 2021. [Online]. Available: https://onlinelibrary.wiley.com/doi/abs/10.1002/mrm.28836

[39] P. Sanpitak, B. Bhusal, B. T. Nguyen *et al.*, "On the accuracy of Tier 4 simulations to predict RF heating of wire implants during magnetic resonance imaging at 1.5 T," in *2021 43rd Annual International Conference of the IEEE Engineering in Medicine Biology Society (EMBC)*, 2021, pp. 4982–4985.

[40] B. T. Nguyen, B. Bhusal, A. A. Rahsepar *et al.*, "Safety of MRI in patients with retained cardiac leads," *Magnetic Resonance in Medicine*, vol. 87, no. 5, pp. 2464–2480, 2022. [Online]. Available: https://onlinelibrary.wiley.com/doi/abs/10.1002/mrm.29116

[41] X. Yang, R. Guo, J. Zheng *et al.*, "Impact of patient postures on the RF-induced heating for the active implantable medical device (AIMD) at 1.5T MRI," *IEEE Transactions on Electromagnetic Compatibility*, vol. 66, no. 4, pp. 1029–1040, 2024.

[42] *ASTM F2182-11a - Standard Test Method forMeasurement of Radio Frequency Induced Heating On orNear Passive Implants During Magnetic Resonance Imaging*, American Society for Testing and Materials Std., 2011.

[43] Medical Device Marketing Agency - Active Medical Devices Vs. Passive Medical Devices 2024, accessed on 18-03-2025. [Online]. Available: https://www.medicaldevicemarketingagency.com/articles/active-medical-devices-vs-passive-medical-devices

[44] S.-M. Park, R. Kamondetdacha, and J. A. Nyenhuis, "Calculation of MRI-induced heating of an implanted medical lead wire with an electric field transfer function," *Journal of Magnetic Resonance Imaging*, vol. 26, no. 5, pp. 1278–1285, 2007. [Online]. Available: https://onlinelibrary.wiley.com/doi/abs/10.1002/jmri.21159

[45] A. Missoffe and S. Aissani, "Experimental setup for transfer function measurement to assess RF heating of medical leads in MRI: Validation in the case of a single wire," *Magnetic Resonance in Medicine*, vol. 79, no. 3, pp.

1766–1772, 2018. [Online]. Available: https://onlinelibrary.wiley.com/doi/abs/10.1002/mrm.26773

[46] P. R. S. Stijnman, M. A. Erturk, C. A. T. van den Berg *et al.*, "A single setup approach for the MRI-based measurement and validation of the transfer function of elongated medical implants," *Magnetic Resonance in Medicine*, vol. 86, no. 5, pp. 2751–2765, 2021. [Online]. Available: https://onlinelibrary.wiley.com/doi/abs/10.1002/mrm.28840

[47] ZMT Zurich MedTech AG - Medical Implant Test System (MITS), accessed on 18-02-2025. [Online]. Available: https://zmt.swiss/validation-hw/mits-systems/mits1-5/?pdf=view

[48] A. G. Webb, Ed., *Magnetic Resonance Technology: Hardware and System Component Design*. The Royal Society of Chemistry, May 2016. [Online]. Available: https://doi.org/10.1039/9781782623878

[49] Schmid und Partner Engineering AG, TDS measurement probe, accessed on 04-03-2025. [Online]. Available: https://speag.swiss/components/probes-2/e-field/e1tds-tds-e-probes/?pdf=view

[50] Schmid und Partner Engineering AG - Easy6 measurement probe, accessed on 04-03-2025. [Online]. Available: https://speag.swiss/components/probes-2/dosimetric/ex3dv4-isotropic-dos-probe-3/?pdf=view

[51] WEIDMANN Technologies Deutschland GmbH - TS2P, accessed on 04-03-2025. [Online]. Available: https://www.micronor.com/products/files/TS2P/MICRONOR_DS_TS2P.pdf

[52] WEIDMANN Technologies Deutschland GmbH - TS5, accessed on 04-03-2025. [Online]. Available: https://www.micronor.com/products/files/TS5/MICRONOR_DS_TS5.pdf

[53] S. Kuschkowitz, "Entwicklung und Umsetzung eines dreidimensionalen, computergesteuerten Sondenpositionierungssystems für den Einsatz in Hochfrequenztestumgebungen," Bachelorarbeit 2018.

[54] W. Kainz, "MR heating tests of MR critical implants," *Journal of Magnetic Resonance Imaging*, vol. 26, no. 3, pp. 450–451, 2007. [Online]. Available: https://onlinelibrary.wiley.com/doi/abs/10.1002/jmri.21020

[55] K. B. Baker, J. A. Tkach, J. A. Nyenhuis *et al.*, "Evaluation of specific absorption rate as a dosimeter of MRI-related implant heating," *Journal of Magnetic Resonance Imaging*, vol. 20, no. 2, pp. 315–320, 2004. [Online]. Available: https://onlinelibrary.wiley.com/doi/abs/10.1002/jmri.20103

[56] ZMT Zurich MedTech AG - Medical Implant Test System - TableTop (MITS-TT), accessed on 18-03-2025. [Online]. Available: https://zmt.swiss/validation-hw/mits-systems/mits-tt/?pdf=view

[57] S. Song, J. Zheng, Y. Wang *et al.*, "Dual-frequency high-electric-field generator for MRI safety testing of passive implantable medical devices," *IEEE Transactions on Microwave Theory and Techniques*, vol. 68, no. 12, pp. 5423–5431, 2020.

[58] Y. Wang, S. Song, J. Zheng *et al.*, "A novel device model validation strategy for 1.5- and 3-T MRI heating safety assessment," *IEEE Transactions on Instrumentation and Measurement*, vol. 69, no. 9, pp. 6381–6389, 2020.

[59] M. Kozlov, L. M. Angelone, and S. Rajan, "Effect of multiple scattering on heating induced by radio frequency energy," *IEEE Transactions on Electromagnetic Compatibility*, vol. 62, no. 5, pp. 2311–2316, 2020.

[60] A. Yao, E. Zastrow, E. Neufeld *et al.*, "Novel test field diversity method for demonstrating magnetic resonance imaging safety of active implantable medical devices," *Physics in Medicine and Biology*, vol. 65, no. 7, p. 075004, apr 2020. [Online]. Available: https://dx.doi.org/10.1088/1361-6560/ab7507

[61] Z. Wang, J. Zheng, Y. Wang *et al.*, "On the model validation of active implantable medical device for MRI safety assessment," *IEEE Transactions on Microwave Theory and Techniques*, vol. 68, no. 6, pp. 2234–2242, 2020.

[62] *ISO 10974:xxxx - Assessment of the safety of magnetic resonance imaging for patients with an active implantable device*, International Organization for Standardization Std., will be released in 2026.

[63] E. Zastrow, A. Yao, and N. Kuster, "Practical considerations in experimental evaluations of RF-induced heating of leaded implants," in *2017 XXXIInd General Assembly and Scientific Symposium of the International Union of Radio Science (URSI GASS)*, 2017, pp. 1–4.

[64] R. M. Laser, "Aufbau und Integration eines Stabilisationssystem in einem MR äquivalentem Expositionssystem, sowie die Programmierung einer Steueroberfläche," Bachelorarbeit 2022.

[65] *ISO/TR 21900:2017 - Guidance for uncertainty analysis regarding the application of ISO/TS 10974*, International Organization for Standardization Std., 2017.

Danksagung

An dieser Stelle möchte ich mich bei allen bedanken, die mich in den letzten Jahren begleitet und die Erstellung dieser Arbeit ermöglicht haben!

An erster Stelle möchte ich mich bei Herrn Prof. Dr. Kevin Kröninger dafür bedanken, dass er sich bereit erklärt hat, diese Arbeit in dieser ungewöhnlichen Konstellation zu betreuen, wie auch schon die vorangegangenen Abschlussarbeiten. Ich danke Ihnen für Ihre positive, optimistische, verständnisvolle und humorvolle Art. Weiterhin möchte ich mich bei Herrn PD Dr. Armin Lühr für die Übernahme der Rolle des Zweitgutachters dieser Arbeit bedanken. Vielen Dank für Ihre Spontanität und Flexibilität.

Vielen Dank an die gesamte Gruppe E4, die über die Jahre wichtige Fragen und Anmerkungen zu meinem Thema hatte und mich wöchentlich an physikalischen Themen und Diskussionen teilhaben ließ. Ich habe viele spannende Einblicke in verschiedene Bereiche erhalten. Ein besonderer Dank geht an dieser Stelle an Jens für seine Verfügbarkeit bei Fragen, seine Kommentare zu meiner Arbeit und seine generelle Bereitschaft, sich mit meinem externen Thema zu beschäftigen.

Ein weiterer wichtiger Dank geht an die MR:comp GmbH, ohne die diese Arbeit nicht möglich gewesen wäre. Vielen Dank an Herrn Gregor Schaefers für die Bereitstellung aller Messgeräte und die allgemeine Unterstützung über die Jahre. Ein weiterer Dank geht an das gesamte Team der MR:comp, das mir den Arbeitsalltag verschönert hat! Ob beim gemeinsamen Mittagessen, bei Feierabendaktivitäten oder bei Gruppendiskussionen zu allen Themen, die die Welt bewegen, es hat immer Spaß gemacht! Ein besonderer Dank geht an Vincent, Micha und Mikhail, einer von euch hatte immer eine Lösung oder Antwort auf jede Frage oder wusste die richtigen Knöpfe an den Geräten zu drücken. Danke an Sebastian für die Umsetzung aller 3D-Druck-Anfragen (auch von meiner Tochter) und an Jens für alle Korrekturen.

Ali und Henning! Danke, dass ihr meine Freunde seid. Danke für alles, was wir in den letzten Jahren zusammen erlebt haben! Danke, dass ihr vorgelegt habt! Danke, dass ihr mir geholfen habt und für Fragen und Diskussionen zur Verfügung standet und steht! Danke für Spiegelei Speck! Auf alles was kommt :)
Danke Godje! Fürs Boot teilen, fürs Verständnis und das Empowerment!

Zu guter Letzt möchte ich mich bei meiner Familie bedanken! Bei meinen Eltern für die Unterstützung und das Verständnis und bei meinem Mann und meiner Tochter für die bedingungslose Liebe! Ohne euch beide wäre das alles nicht möglich gewesen. Ein kleines Dankeschön für den Zeitdruck und die damit verbundene Extraportion Motivation geht an das strampelnde Baby in meinem Bauch, bis bald! ♡